Tunable quantum interfaces between superconducting qubits and microwave photons induced by extreme driving

Ann, B.

DOI
10.4233/uuid:477df1e7-29fc-494b-af92-f5d63af87366

Publication date
2021

Document Version
Final published version

Citation (APA)
Ann, B. (2021). *Tunable quantum interfaces between superconducting qubits and microwave photons induced by extreme driving*. [Dissertation (TU Delft), Delft University of Technology]. https://doi.org/10.4233/uuid:477df1e7-29fc-494b-af92-f5d63af87366

TUNABLE QUANTUM INTERFACES BETWEEN SUPERCONDUCTING QUBITS AND MICROWAVE PHOTONS INDUCED BY EXTREME DRIVING

TUNABLE QUANTUM INTERFACES BETWEEN SUPERCONDUCTING QUBITS AND MICROWAVE PHOTONS INDUCED BY EXTREME DRIVING

Dissertation

for the purpose of obtaining the degree of doctor
at Delft University of Technology
by the authority of the Rector Magnificus, Prof. dr ir. T.H.J.J. van der Hagen,
chair of the Board for Doctorates
to be defended publicly on
7th July 2021 at 12:00 o'clock.

by

Byoung-moo ANN

Master of Science in Physics,
Ludwig Maximilians Universität München, Germany,
born in Seoul, Republic of Korea (South Korea).

This dissertation has been approved by the promoters

Composition of the doctoral committee:

Rector Magnificus,	chairperson
Prof. dr. G. A. Steele,	Delft University of Technology, promotor
Dr. T. van der Sar,	Delft University of Technology, copromotor

Independent members:

Prof. dr. D. Vitally,	University of Camerino
Prof. G. S. Paraoanu,	Aalto University
Prof. dr. B. Terhal,	Delft University of Technolog
Prof. dr. Y. M. Blanter,	Delft University of Technology
Prof. dr. A. F. Otte,	Delft University of Technology, reserve member

Keywords: Circuit quantum electrodynamics, Quantum engineering.

Printed by: Gildeprint, Enschede

ISBN 978-90-5934-481-3

Casimir PhD Series, Delft-Leiden 2021-15

An electronic version of this dissertation is available at
http://repository.tudelft.nl/.

Thoroughly conscious ignorance is the prelude to every real advance in science.

James Clerk Maxwell

CONTENTS

PREFACE

I hope this thesis will contribute to the effort of making world better to live.

Byoung-moo Ann
Delft, June 2021

1

INTRODUCTION

1

This thesis deals with the theoretical and experimental studies about implementing a tunable quantum interface between superconducting qubits and microwave photons. The purpose of this chapter is to provide readers with overall backgrounds on how quantum science and technology have developed so that they grasp the motivations and importance of the studies provided in this thesis. The following is a brief summary of this chapter.

Section 1.1 focuses on the development of quantum mechanics in the experimentalist's perspective. I will explain how the technological developments contributed to the advances in the quantum revolution that began in the early twentieth century. The point I emphasize in this section is that quantum mechanics has evolved with much effort from experimentalists as well as theorists. **Section 1.2** introduces the rise of quantum technology. As many mysteries in quantum mechanics have been unveiled, physicists and engineers' attention moved to how to make use of it, and these desires triggered the advent of quantum technology. **Section 1.3** introduces to the many types of quantum systems considered promising platforms for applications. This section provides understanding their working principles and discusses the pros and cons as candidates for quantum technology. **Section 1.4** focuses on the case of state engineering harmonic oscillators. One especially important mission in quantum technology is to engineer the quantum states of harmonic oscillators, one of the most essential forms that frequently appear in many disciplines of physics. However, manipulating Harmonic oscillator's quantum states is a challenging task compared with other strongly nonlinear systems due to its harmonicity. A couple of strategies on how to synthesize the Harmonic oscillator's quantum states are introduced. **Section 1.5** concludes this chapter. Currently, superconducting quantum circuit is the best platform in terms of quantum state engineering with harmonic oscillators. A variety of exotic quantum states have been experimentally demonstrated with microwave resonators assisted by the superconducting qubits. Here, tunable quantum interface between them is a key for the successful manipulation. The rest of this thesis is closely related with the unexplored topics (mainly quantitative) in the superconducting qubit research regarding this tuneable interface.

1.1. ADVANCES IN QUANTUM MECHANICS FROM AN EXPERIMENTALIST'S POINT OF VIEW.

The beginning of this chapter might be different from other literature that conventionally concentrates on the theoretical perspectives. In the early 20th century, physicists found clear evidence of classical physics' failure in explaining the experiments such as black body radiation, photoelectric current, and electron scattering (Davisson-Germer), electron-atom collision (Frank-Hertz), and many more. Through contributions from many brilliant minds, a new framework that describes the microscopic world had appeared, which we call quantum physics. It goes without saying that the advent of quantum mechanics is one of the biggest events in science history.

However, the technical limitations significantly impeded the deeper studies on the quantum foundation and more rigorous tests of quantum mechanics. For example, the photoelectric effect that led to the discovery of light quanta can also be explained by an alternative semi-classical theory without quantizing the electromagnetic fields. Strictly

speaking, the photoelectric effect cannot be considered a sufficient condition of light's quantum nature. Unfortunately, at the beginning of quantum mechanics' history, technical limitations hindered the rigorous test of the light quanta's existence.

Another example is the test of Bell-inequality. There were a number of debates over how to interpret the wavefunction in quantum mechanics. Two major interpretations, among many others, are local realism and Copenhagen interpretation. These two differently state how the measurement in quantum physics works. The question of which interpretation properly explains the nature can be answered through experimentally testing Bell-inequality. If Bell-inequality violates, then local realism should fail. This means that the locality and reality of the universe cannot exist at the same time. However, when Bell-inequality was proposed, it could not be tested in the real world since there was no proper experimental test-bed. Despite its importance, the experimental test of Bell-inequality fell out of the attention of the physicist for many years.

It took a long time until both cases were experimentally confirmed. The first rigorous experimental evidence of the photon was found in a photon correlation measurement [1]. In the experiments given in [1], a couple of advanced techniques were employed. First, they used an atomic cascade decay as a single-photon source. When one photon is detected, then it heralds the other photon at another detector. By doing so, they were able to expect the arrival times of a single photon and identify the photon cannot be divided further. Second, the other core of the experiment is the Hanbury-Brown Twiss (HBT) interferometer. It was originally devised for astronomical study. In this work, however, it was used to identify an anti-correlation of the photo-detection, which demonstrates the single photon's existence. Here, we can conclude the advances in the experimental techniques such as heralding single-photon detection, or HBT type interferometry had significant roles in revealing the fundamentals of quantum mechanics.

Such a conclusion can be equivalently applicable to the case of Bell-inequality. The first experiment that demonstrated the violation of Bell-inequality was reported in [2], a long time after Bell proposed the theory. The experiment used the fact that the momentum entanglement of the emitted photon pairs from the atomic cascade decay. Later, more and more experiments were performed to test the Bell-inequality with different approaches. As the technology developed, various quantum systems have become testbeds for Bell experiments such as optomechanics [3], Nitrogen vacancy centers [4], superconducting qubit [5]. All the results from these experiments are interpreted in the context of the Copenhagen interpretation.

The lesson we should take from the above stories is that the progress in the experimental techniques accompanied the progress in quantum mechanics. That is to say, quantum mechanics is not all about the theoreticians' masterpiece. We should also acknowledge the many efforts made by a number of experimentalists and technicians (whose names are indeed less familiar to the public) engaged in the development of quantum mechanics. Taking such a technical point of view is largely recommended to have a comprehensive view of how quantum physics studies have evolved and how it will be like in the future.

1

1.2. QUANTUM TECHOLOGY

One of the biggest motivations to study quantum mechanics is to use the quantum properties of the microscopic objects for our daily life. Nowadays, there are many research areas where people are working toward the application of quantum mechanics. Such a trend led to the birth of new terminology, 'quantum technology.' Literally, it refers to the technologies that benefit from the laws of quantum mechanics. Many scientists expect that quantum technology will be a disruptive technology in the future. On the other hand, many scientists expect that quantum technology will assist the existing technology and not replace it. In any case, it is definitely clear that quantum technology will push the limits of current technology to some extent.

The largest sector of quantum technology is undoubtedly quantum computing [6]. It uses superposition and entanglement to store information and perform computation. Recently, quantum artificial intelligence has emerged as a potential area where we can benefit from quantum computing. In communication and cryptography, it has been proposed and demonstrated that using entangled photon pairs provides great advantages [7]. Quantum simulation [8] is one of the big sectors of quantum technology. The computational complexity of solving quantum systems exponentially scales with the size of the systems. Using analogies with another simpler quantum system, we can indirectly investigate the target system, beyond the efficiency limits of classical computers. Quantum sensing, employing quantum technologies to overcome the limits of classical sensors, is another rapidly growing area.

1.3. VARIOUS QUANTUM SYSTEMS AND THEIR CONTROLS

Faithful control of the quantum systems is a core technique for quantum technologies. Unfortunately, controlling individual quantum systems is technically even more challenging than conventional classical systems. This is because the quantum states are extremely fragile under the interactions with the environments surrounding the quantum systems. To conserve the quantum properties for a long time, we should isolate them from the environment, and the demanded extent of the isolation is far beyond the requirements for any classical technologies. Depending on the types of quantum systems, different conditions are required. With advances in many engineering disciplines, manipulating the quantum states became more and more feasible, and the experimental demonstrations have been reported with various quantum systems.

The atomic metastable states or hyperfine states have very long lifetimes, and hence these were considered attractive places to store quantum information since many decades. In an ultracold atomic gas in a quantum regime, millions of atoms behave as if they are one particle. We can observe quantum mechanical phenomena more easily since the light absorption or emissions by atomic clusters are even stronger than those from a single atom. By manipulating the trapping potential, we can also investigate the dynamics of the electrons in solid-state lattices (quantum simulation with optical lattices) [9]. Thanks to the advances in laser cooling/trapping techniques and vacuum technology, atomic physics rose as a leading platforms for quantum information processing and quantum simulation. Revolutionary developments in laser and vacuum technologies made it possible to realize many marvelous experiments such as single atom trapping

[10], Bose-Einstein condensation [11], and simulating quantum phase transition [12]. We cannot miss the invention of the ion trap as one of the milestones in the history of modern atomic physics. Trapping neutral atoms should rely on laser trapping and the laser power largely limits the depth of the trapping potential, which results in the limitation in the trapping times. In the meantime, an ion trap normally yields more than 1 keV trapping energy. Nowadays, ions even can be trapped for more than a day. Moreover, the collective mechanical modes formed by Coulomb interactions between ions makes it easy to transfer the quantum states among the ions. This makes the ion traps strong candidate for realizing quantum computing. Remarkably high fidelities in quantum gate operations are reported with ion trap architecture nowadays [13].

With optical photons, the polarization degree of freedoms as carriers of quantum information is often used. The excellent property of the photonic qubits is that polarizations are hardly affected by surrounding environments. Also, photons naturally propagate through space, and therefore they are suitable to deliver quantum information from one place to another. These advantages accounted for the fact that the photonic qubits have been strong candidates for quantum information processing since the early phase. One milestone event is entangled photon pair generation from the spontaneous parametrical down-conversion (SPDC) process [14]. It formed a basis in many applications like quantum teleportation [15] and cryptography [16]. I should point out that the progress in the photonic qubits goes along with the progress in nonlinear optics, as we can see in SPDC.

So far, we have discussed quantum technologies using atoms and optical photons (B.1)[1]. I would have to call these 'traditional' forms since they are relatively older than other approaches, which I will introduce now. Advances in nano-fabrication and cryogenic technology enable that solid state-based qubits have merged as strong competitors. This involves semiconductor quantum dots [17], superconducting qubits [18], and many others (B.2). They have a shorter history but have grown rapidly, threatening the status of the 'traditional' approaches.

In the following part of this section, I will briefly introduce qubits based on semiconductor quantum dots and superconducting circuits, and omit the explanations of other types of solid-state qubits. Trapped electrons in the quantum dots defined in the two-dimensional electron gas (2DEG) at heterostructures paved another way toward quantum technology. The electric potential can be synthesized by manipulating the voltages of the electrodes. Typically, the double-well potential configuration (double quantum dot) is preferred. Electrons trapped in the quantum dots are analogous with the trapped atomic ions, but the working principles are quite different. We can use the charge or spin states of electrons as qubits. Qubits based on charge states have very short coherence times (a few nanosecond scales) due to the charge noise. Meanwhile, qubits based on spin states have much longer coherence times, but we need to apply strong magnetic fields to split the energy levels of each spin state. The strong magnetic fields can break superconductivity, and therefore spin-based quantum dot qubits have a limitation when we want to them interfaced with superconducting resonators or superconducting qubits.

[1] Figures are taken from the following websites. https://physics.illinois.edu/people/directory/profile/kwiat (a),https://quantumoptics.at/en/research/quantum-information.html (b), and https://www.nist.gov/ (c).

1

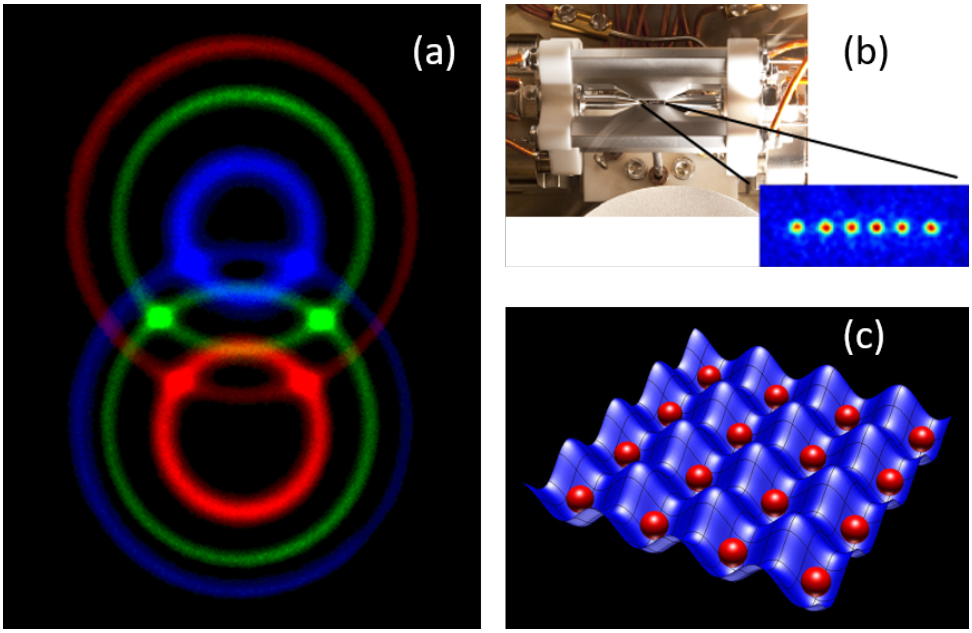

Figure 1.1: Atomic and optical quantum systems. (a) An image of type-2 spontanous parameteric down conversion (SPDC). Where two green rings intersect, the polarizations of the photon pairs at each intersections are entangled. (b) An image of a blade type ratio-frequency ion trap. An image of a CCD camera that shows a string of trapped 5 ions is also given at the lower part. (c) A schematic image of atoms trapped on an optical lattice.

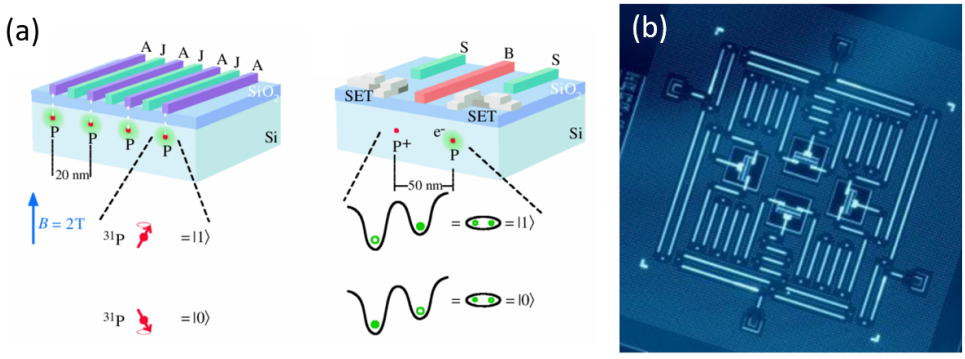

Figure 1.2: Solid-state based quantum systems. (a) Illustrations on how the spin (left) and charge qubit (right) can be defined with semiconductor quantum dots. (b) An optical microscopy image of a superconducting device that contains multiple transmon qubits and co-planer waveguide resonators.

A superconducting qubit is comprised of Josephson junctions and other linear circuit elements. Without Josephson junctions, we can always decompose the circuits into a series of harmonic oscillators, and therefore all the energy levels of modes are equally spaced. In this case, we cannot define qubit states. We can use Josephson junctions that act as nonlinear inductors to make the energy levels non-equally spaced. Superconducting qubits refer to qubits based on the superconducting circuits involving such nonlinear elements. Depending on the circuit designs, the superconducting qubits are classified by several types. The most representative ones are the charge qubits, the flux qubits, and the phase qubits. In addition to this, there are many hybridizations. Depending on the parameters, the charge qubits are divided into the Cooper-pair boxes [19] and the transmons [20]. The former has strong nonlinearity but extremely sensitive to the charge noise. The latter is widely preferred due to the insensitiveness to the charge noise. The weak nonlinearity of transmons causes some problems, but at the same time, many technical approaches to overcome them are devised and demonstrated [21]. The study of the interactions between superconducting qubits and microwave photons is called circuit quantum electrodynamics (QED) [19], taking analogies of cavity-QED that studies the interactions between atoms and single-mode light.

We can roughly classify the quantum systems we have discussed so far into two classes: One is atomic/optical systems, and the other is solid-state systems. The pros of the atomic and photonic systems are long coherence time and the fact that we do not need the clean room process. The finite trapping time of atoms or decay time of photons is one of the cons. We can also point out that the system parameters of the atomic system cannot be engineered since they are already fixed by nature. The solid-state systems also have pros and cons. One of the pros is their compatibilities to Silicon and CMOS technologies. Also, unlike atomic systems, we can engineer the system parameters as targeted. The cons are requirement of cryogenic systems, clean room tasks, and relatively short coherence times.

Nowadays, a number of academic and industrial research groups are competing for developing quantum technology toward realization in real-life applications. It is currently debatable which one is the most superior and the most advantageous to the ultimate goals. The one important thing is that all the candidates are yet nascent. It is an interesting It is interesting to see which system will be the final winner in this race. At the same time, we should not forget that we might not see the end of this race while we live.

1.4. QUANTUM STATE ENGINEERING OF HARMONIC OSCILLATORS.

As I remark in the previous section, manipulating arbitrary quantum states is the heart of quantum technology. For strongly nonlinear systems like two-level qubits, we can individually address the transitions between arbitrary two quantum states of the systems. By consecutively inducing the transitions, we can synthesize arbitrary quantum states as long as the process is done within the lifetimes of each quantum state. Unfortunately, this simple picture is not available for the opposite case, where the nonlinearity is not sufficient. In that sense, the difficulty is the highest for the harmonic oscillators, where

all the energy levels are equally spaced. It sounds quite paradoxical that the quantum state control of the simplest system is more difficult than any other system.

The harmonic oscillator ubiquitously appears in all the areas of science and engineering. Basically, any potential function near the stable points can be approximated as harmonic potentials. Many systems have an analogy with the harmonic oscillator. It also comprises one of the archetypes in quantum technology. The typical types of harmonic oscillators that we frequently meet in the study of quantum technology are photons in optical and microwave resonators, mechanical modes of trapped ions, acoustic resonators, and cavity optomechanics. Recently, the idea to store quantum information on the harmonic oscillators, called the bosonic quantum information process, has emerged [22–24] due to the convenience for quantum error corrections. Such a trend demands further studies on the faithful quantum state generation in the harmonic oscillators.

Many schemes have been proposed and demonstrated in various systems. A common key strategy is to introduce other nonlinear systems (mostly two-level qubits) coupled to the resonators in a tunable manner. In the case of trapped ions, the sideband transitions are employed between the mechanical mode and two-level electric states. In the case of superconducting qubits and resonators, the fundamentals of the methods are the same. For example, a superconducting flux qubit is used to create multi-photon Fock states in a superconducting resonator [25]. In the study, the qubit is initially far detuned and effectively decoupled to the resonator. They turn on the interaction by rapidly switching the qubit frequency to the same frequency of the resonator. Repeating turning on and off the interaction, they create the Fock states up to six photons. In more recent studies [26], a configuration with two superconducting resonators (one is for storage and the other is for engineering) mediated by a transmon qubit is employed. Applying external driving fields with proper matching frequencies, the state of the storage resonator is stabilized to target states.

1.5. THESIS OUTLINE

From the above discussion, one can readily notice that the tunable interface between nonlinear systems and harmonic oscillator is a key to engineer the harmonic oscillator's quantum states. In this thesis, I will narrow the scope to superconducting qubit cases. Despite several disadvantages, the superconducting qubit architecture is undoubtedly the leading platform at present. This thesis investigates a couple of unexplored topics in superconducting qubit studies. I specifically focused on how to implement *in-situ* tunable quantum interface to superconducting resonators by driving the qubits. In circuit QED, it is often required to use *extreme* drive fields. The previous studies largely depend on the rotating wave approximation (RWA), a useful technique when dealing with the time-periodically driven Hamiltonian, but it does not correctly describe the systems' dynamics when the drive fields are excessively strong and far off-resonant. Breakdowns in the RWA often happen in circuit QED experiments but are not intensively studied. Specifically, how the breakdown of the RWA affects the interaction rates between two systems has been mostly unexplored. The main topic throughout this thesis is a quantitative study on the sideband interaction rates in a dispersively coupled qubit and resonator configuration. We also explore a possible application of the sideband transitions

in the precise resonator spectroscopy.

This thesis is organized as follows. **Chapter 2** provides theoretical background required to understand the main ideas of the thesis. It involves elementary quantum theory and an introduction to circuit quantum electrodynamics (QED). In addition, I will discuss about several methodologies to implement tuneable quantum interfaces in circuit QED. I will argue that the method using external transverse driving fields is the most advantageous one in some specific perspectives. This approach is the central topic in the remaining part of the thesis.

Chapter 3 gives description on the fabrication steps for superconducting circuits. It also provides description on the cryogenic measurement system used for the experiments in this thesis.

In **Chapter 4**, covers analytical and numerical studies on two-photon sideband transition in the quantum Rabi model (QRM). Many circuit QED systems can be described by the QRM. Therefore, it is of pivotal importance to understand how to implement the tunable quantum interface between the qubits and microwave photons in the QRM.

In **Chapter 5**, I present a study on two-photon sideband transition between a transmon and a reasonator. In the study, all the theoretical, numerical, and experimental studies are consistent with one another. Since a transmon cannot be approximated by a two-level system, a different approach is required to understand it quantitatively.

In **Chapter 6**, I propose and demonstrate a new approach for spectroscopy of superconducting resonators. Based on the electromagnetically induced transparency (EIT). This new approach is especially useful when one do not want the probe to affect the quality factors of the target resonators.

Chapter 7 concludes the thesis.

2

THEORETICAL BACKGROUND

This chapter provides the theoretical background necessary to comprehend the remaining parts of this thesis. I start with introducing the elementary concept of quantum theory and then discuss how to apply quantum theory to linear circuit systems. Next, the discussion is extended to the nonlinear circuit systems. Josephson junction is the indispensable element for the superconducting qubits, which is kind of artificial atoms made on the chips. Together with microwave photons in superconducting resonators, the superconducting qubits form the circuit electrodynamics (QED) systems. After a brief introduction to the circuit QED, several methods for in-situ control of the interactions between superconducting qubits and microwave resonators are addressed. Of all the methods, this thesis covers the one employing external transverse driving fields. I explain under which perspectives this approach especially makes a difference compared with other approaches.

2.1. QUANTUM THEORY IN A NUTSHELL

In quantum mechanics, the quantum state of a system is represented by a vector $|\psi\rangle$ in a Hilbert space. This is called a state vector (or state ket). For a system having multiple degrees of freedom, (DOF) direct product of multiple state kets represents the system's total quantum state, and each ket represents the state of each DOF. Meanwhile, a hermitian operator acting on the state kets represents a corresponding physical observable. The eigenvalues of the operator represent the possible values to measure. In the case of some quantum operator such as position or momentum operator ($\hat{x}$ and $\hat{p}$ respectively), the eigenvalues are continuous, and these are called continuous variables. The dimension of the Hilbert space is determined by the system's physical properties. For a spin 1/2 system, the spin DOF can be represented by a two-dimensional Hilbert space. For a system whose Hamiltonian is comprised of continuous variables, we need an infinite-dimensional Hilbert space.

Unlike classical physics, quantum mechanics allows the systems to exist in two or more different states at the same time. This is called quantum superposition. The mathematical expression of the quantum superposition among state $|\psi_n\rangle$ is given by,

$$|\psi\rangle = \Sigma_n c_n |\psi_n\rangle . \tag{2.1}$$

Here, c_n are complex numbers whose magnitudes are lower than unity. A probability to find the system in the state $|\psi_n\rangle$ is given by $|c_n|^2$. We should distinguish this from the statistical mixture of each state. The former shows quantum interference effects but the latter does not. In order to distinguish them mathematically we should introduce the concept of the density matrix. If the state is defined by only a single ket $|\psi\rangle$ (pure state), the density matrix is given by $\hat{\rho} = |\psi\rangle\langle\psi|$. On the other hand, if the state is defined as a statistical mixture of multiple kets $|\psi_n\rangle$ (mixed state), the density matrix is given by $\hat{\rho} = \Sigma \rho_n |\psi_n\rangle\langle\psi_n|$. Here, ρ_n is real positive numbers less than unity and interpreted as a probability to find the system in the state ψ_n. Now, we can readily see the difference between the quantum superposition and the statistical mixture in the density matrix representations. We can define the purity γ of a quantum state $\hat{\rho}$ like below,

$$\gamma = \mathrm{tr}(\hat{\rho}^2). \tag{2.2}$$

γ satisfies the condition $1/d \leq \gamma \leq 1$, and d is the dimension of the Hilbert space. If γ is unity, then $\hat{\rho}$ is a pure state. Even the state that was initially pure state can lose its purity. One possible scenario is the interaction with the environment. More detail discussion on this is given in section 2.1.4. Density matrices do not need to be diagonal in the matrix representations. The diagonal components are called population and the off-diagonal components are called coherence respectively.

In general, the time evolution of a ket state $|\psi\rangle$ or a density matrix $\hat{\rho}$ is governed by Schrödinger equation,

$$\begin{aligned} \hat{H}|\psi\rangle &= i\hbar \frac{\partial |\psi\rangle}{\partial t}, \\ \frac{d\hat{\rho}}{dt} &= -i\hbar[\hat{H}, \hat{\rho}]. \end{aligned} \tag{2.3}$$

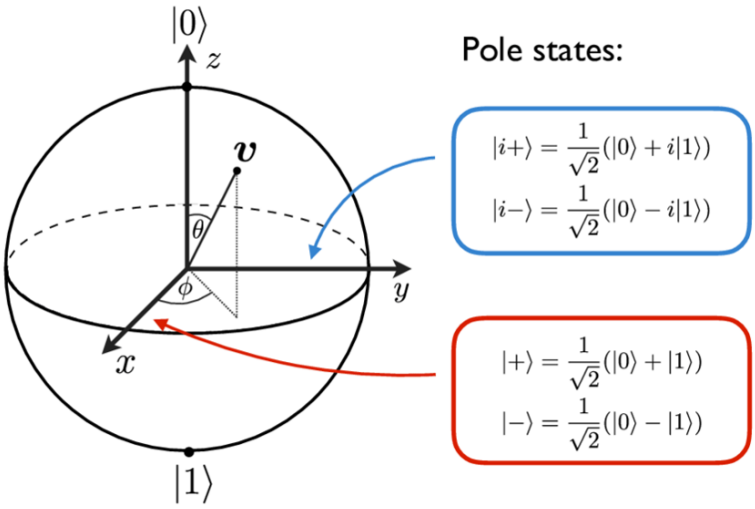

Figure 2.1: Retrieved from [27]. Illustration of Bloch sphere representation of the arbitrary quantum state of a two-level system.

Here, $\hat{H}$ is the Hamiltonian operator of the system. If the state is the eigenstate of $\hat{H}$ and there is not explicit time-dependence in $\hat{H}$, only the phase of the state vector is evolving not changing its direction. Therefore, the eigenstate of the Hamiltonian is a stationary state. Describing the system on the eigenbasis of the Hamitonian operator is the simplest way to do it and that is why we always try to find the energy levels of the systems first in quantum mechanics. Things become more complex with the time-dependent Hamiltonian. We will meet this case in section 2.1.3.

2.1.1. TWO-LEVEL SYSTEM

A two-level system (TLS) can be described by a two dimensional Hilbert space. The spin DOF of spin 1/2 particles or the polarization DOF of the photons are examples. The TLS is the simplest form of systems in quantum mechanics. Understanding the dynamics of TLS is important not just for the systems like the spin 1/2 or polarization but also for the multi-level systems such as atomic systems or other ones that have complicated energy level structures. In describing the dynamics between two specific quantum states of an arbitrary system, everything follows the rule of the TLS as long as the state leaking to the other states is negligible. The quantum systems where we define qubit states are not the TLS in many cases. If one cares all the energy levels of the systems, it results in huge overhead in the calculations. It should be a wise decision to approximate the systems to the TLS, when the contributions from the other states are negligible in the dynamics. In this thesis, I use $|0\rangle$ and $|1\rangle$ for each energy eigenstates ($|0\rangle$ has a smaller energy) of the TLS[1]. If the transition frequency is ω_0, then the Hamiltonian can be represented in a 2 by

[1] I stick to this convention throughout this thesis. That is, $|n\rangle$ refers to the n-th energy eigenstate of any arbitrary systems. Otherwise, there will be a remark.

2 matrix,

$$\hat{H}_{\mathrm{TLS}} = \frac{\hbar}{2}\begin{pmatrix}\omega_0 & 0\\ 0 & -\omega_0\end{pmatrix}. \tag{2.4}$$

Figure 2.1 describes how the state of a TLS can be represented with a Bloch sphere. $|0\rangle$ and $|1\rangle$ are orthonormal basis states. For a Bloch vector $\vec{v} = (v_x, v_y, v_z)$, the corresponding density matrix is given by,

$$\hat{\rho} = \frac{1}{2}\begin{pmatrix}1+v_z & v_x - i\,v_y\\ v_x + i\,v_y & 1-v_z\end{pmatrix}. \tag{2.5}$$

In above matrix representation, the first row and column correspond to $|1\rangle$ in Figure 2.1. For a pure state, the states are sitting on the surface of the sphere. For fully mixed state, the states are within the Bloch sphere. The Bloch sphere representation provides us with graphical descriptions of the quantum states. It is useful to visualize the the dynamics of state kets.

2.1.2. SYSTEM WITH CONTINUOUS VARIABLES

The physical observables with a continuous eigenvalue spectrum are called continuous variables. In fact, the most important physical quantities, the position, and momentum are some examples of continuous variables. In addition to these, the electric and magnetic fields are also continuous variables. In contrast to the TLS, the systems defined with continuous variables cannot be described with finite-dimensional Hilbert spaces. Therefore, we need a different formalism than the TLS case. Using continuous-variable (CV) quantum systems can be an alternative approach to realize quantum communication [7] and quantum information processing [16]. Especially for quantum computing, the CV systems have the advantage of implementing quantum error correction codes [22–24]. In this section, we deal with the harmonic and weakly anharmonic oscillator. The importance of the former one is already discussed in chapter 1. The latter one is the model for transmons qubits used in the experimental studies of this thesis.

HARMONIC OSCILLATOR

The Hamiltonian of a mechanical harmonic oscillator $\hat{H}_{\mathrm{HO}}$ is given by,

$$\hat{H}_{\mathrm{HO}} = \frac{1}{2}m\omega^2\hat{x}^2 + \frac{1}{2m}\hat{p}^2. \tag{2.6}$$

Here, m and ω are the mass and the angular resonance frequency of the oscillator respectively. We can rewrite the Hamiltonian with creation and destruction operators $\hat{a}^\dagger$ and $\hat{a}$,

$$\hat{H}_{\mathrm{HO}} = \hbar\omega(\hat{a}^\dagger\hat{a} + \frac{1}{2}). \tag{2.7}$$

The definition of $\hat{a}$ is given by,

$$\hat{a} = \frac{1}{\sqrt{2\hbar m\omega}}(\hat{p} - i\,m\omega\hat{x}). \tag{2.8}$$

The constant one-half in Eq. 2.7 is omitted in many cases. The n-th energy eigenstates $|n\rangle$ ($n = 0, 1, 2...$) are related with one another by the following equations,

$$\begin{aligned} \hat{a}^\dagger |n\rangle &= \sqrt{n+1}\,|n+1\rangle\,. \\ \hat{a}\,|n\rangle &= \sqrt{n}\,|n-1\rangle\,, \end{aligned} \tag{2.9}$$

and the eigenenergies E_n are

$$E_n = \hbar\omega(n + \frac{1}{2}). \tag{2.10}$$

It is useful to define the number operator $\hat{n} = \hat{a}^\dagger \hat{a}$. This counts the number of the excitation of the harmonic oscillators.

Although the derivation so far is based on the mechanical oscillator cases, many other non-mechanical systems take the same form with this Hamiltonian. In this thesis, all of them are called the harmonic oscillators. A single-mode electromagnetic field is one example. In this case, the photons are defined as the eigenstates of the harmonic oscillator that describes the mode's Hamiltonian. The n-th excited state of the harmonic oscillator is equal to n photons stored in the mode.

WEAKLY ANHARMONIC OSCILLATOR

The harmonic oscillator has equally spaced energy levels as seen in Eq. 2.10. This property creates significant difficulties in controlling the quantum states. Therefore, introducing nonlinearities should be necessary for the applications. In this section, I only consider the case of weakly anharmonic oscillators, where the nonlinearities are perturbative. It means that the systems still have properties as the harmonic oscillator but not the same due to the nonlinearities. Two examples we deal with are Duffing and Kerr oscillators. The Hamiltonian of a Duffing oscillator is expressed like below,

$$\hat{H}_{\text{Duff}} = \frac{1}{2}m\omega^2\hat{x}^2 + \beta\frac{\hat{x}^4}{4} + \frac{1}{2m}\hat{p}^2, \tag{2.11}$$

and β is a Duffing coefficient. As we did with the harmonic oscillator, we can also rewrite this Hamiltonian with $\hat{a}^\dagger$ and $\hat{a}$. Then it takes the form given below,

$$\hat{H}_{\text{Duff}} = \hbar\omega\hat{a}^\dagger\hat{a} + \frac{\gamma}{12}(\hat{a}^\dagger + \hat{a})^4. \tag{2.12}$$

When $\omega \gg \gamma$, we can approximate $|n\rangle$ as an eigenstate of $\hat{H}_{\text{Duff}}$. It is the model of transmon qubits, which I will discuss in the section 2.3. If we neglect the off-diagonal terms in Eq. 2.12, then the system described by the reduced Hamiltonian amounts to a Kerr oscillator in the energy eigenbasis,

$$\hat{H}_{\text{Kerr}} = (\hbar\omega + \gamma)\hat{a}^\dagger\hat{a} + \frac{\gamma}{2}\hat{a}^\dagger\hat{a}^\dagger\hat{a}\hat{a}. \tag{2.13}$$

In the Kerr oscillator case, $|n\rangle$ are the exact eigenstates to $\hat{H}_{\text{Kerr}}$, and this statement holds without any approximation.

2.1.3. TIME-PERIODICALLY DRIVEN SYSTEM

Time dependence in a Hamiltonian always causes additional difficulties in analytically solving the system's quantum dynamics. However, time dependence in the Hamiltonian is indispensable if one wants to have a coherent transition from one state to another. Driving the system periodically in time is technically the easiest way to induce the transitions. Thus, it is the most common type of time dependent systems one encounters while investigating coherent quantum control.

There are two types of driving—longitudinal and transverse. In this thesis, when I mention a term 'driving' then it should indicate a transverse driving. In a TLS case, a driving Hamiltonian $\hat{H}_{\mathrm{d}}$ can be expressed by,

$$\hat{H}_d(t)/\hbar = \begin{pmatrix} 0 & \Omega_d \cos\omega_d t \\ \Omega_d \cos\omega_d t & 0 \end{pmatrix}, \tag{2.14}$$

here ω, ω_d, and Ω_d are the transition frequency of the TLS, the driving frequency, and the driving amplitude respectively. The oscillatory terms only exist in the off-diagonal components. In the case of a longitudinal driving, the oscillatory terms must be placed at the diagonal components. The total Hamiltonian $\hat{H}(t)$ of the driven TLS is,

$$\hat{H}(t)/\hbar = \begin{pmatrix} \omega_0/2 & \Omega_d \cos\omega_d t \\ \Omega_d \cos\omega_d t & -\omega_0/2 \end{pmatrix}. \tag{2.15}$$

Obtaining the equation of motion from this Hamiltonian seems an easy task. However, the exact solution of the Schrödinger equation with the above Hamiltonian has not been found until 2020 [28]. Considering the almost 100 year history of quantum mechanics, this manifestly shows how much the 'pain' comes when we struggle with the time-dependent Hamiltonian. Fortunately, if we take proper approximations, these difficulties can be significantly alleviated. One widely used approximation technique when we deal with the oscillatory time dependence is the rotating wave approximation.

ROTATING WAVE APPROXIMATION

The best way to comprehend the rotating wave approximation (RWA) is to look at the Hamiltonian sitting on the rotating frame at a speed ω_d. The transformation from the lab to the rotating frame is given by $\hat{U} = \exp(i\hat{\sigma}_z\omega_0 t/2))$. Under this transformation, we obtain $\hat{H}_{rot}$, which refers to the Hamiltonian seen from the rotating frame.

$$\hat{H}_{rot}/\hbar = \begin{pmatrix} 0 & \Omega_d e^{i(\omega_0-\omega_d)t} + \Omega_d e^{i(\omega_d+\omega_0)t} \\ \Omega_d e^{-i(\omega_0-\omega_d)t} + \Omega_d e^{-i(\omega_d+\omega_0)t} & 0 \end{pmatrix}. \tag{2.16}$$

From the result, we can see the Hamiltonian is divided into two parts: One rotating at $|\omega_0 - \omega_d|$ (slow rotating terms) and the other rotating at $\omega_0 + \omega_d$ (fast rotating terms). When $\omega_d \approx \omega_a \gg \Omega_d$ satisfies, the dynamics is clearly decomposed into a slow (with a large amplitude) evolution and a fast (with a small amplitude) evolution. Typically, only the dynamics with the large amplitude concerns us. By averaging out the fast evolution, we can simplify the dynamics without losing relevant information and this is what amounts to the RWA. The fast evolution is induced by the fast rotating terms, and hence the RWA can be applied just by neglecting that terms in the Hamiltonian from the beginning. The validity of RWA is significantly harmed as the drive amplitude or the detuning

from the resonance ($|\omega_0 - \omega_d|$) are compatible to drive frequency. In the rest of this section, we will explore the consequences when the RWA does not hold.

BREAKDOWN OF THE RWA - RESONANT DRIVING

We first deal with the case when the driving frequency is on resonant with the TLS. Figures. 2.2 lists the dynamics of a driven TLS numerically solved using QuTip [29, 30]. In (a) and (b), where the driving amplitudes are moderate, the dynamics obtained using the RWA (blue curves) are almost equal with the dynamics without the approximation (yellow curves). In (c), we can see small wiggles in the yellow curve with a larger Ω_d. The wiggles get more several in (d) as increasing Ω_d. Until (d), we can somehow decompose the fast and slow dynamics, and the RWA is still beneficial. In (e), with $\Omega_d/2\pi$ =10 GHz, we cannot distinguish the slow and fast dynamics anymore. In (f), with $\Omega_d/2\pi$ =50 GHz, the RWA entirely distorts the dynamics. Over the range $0 < t < 2$, both blue and yellow curves seem sinusoidal, but their periods differ by almost double. More graphical description using Bloch spheres is provided in figure 2.3 .

BREAKDOWN OF THE RWA - FAR DETUNED DRIVING

We now turn to the case when the driving frequency is far detuned from the resonance frequency of the TLS. In this regime, the driving field cannot induce any transition, but lead to a shift in the transition frequency. As long as $\omega_{0,d} \gg \Omega_d$ holds, this shift can be calculated perturbatively and the result is [31],

$$\delta\omega_0 \approx \underbrace{\frac{\Omega_d^2}{2(\omega_0 - \omega_d)}}_{\text{AC-Stark shift}} + \underbrace{\frac{\Omega_d^2}{2(\omega_0 + \omega_d)}}_{\text{Bloch-Siegert shift}} . \tag{2.17}$$

The first term is called AC-Stark shift, and the second term is called Bloch-Siegert shift. Mathematically, both shifts are caused by the slow and fast rotating terms in Eq. 2.16 respectively. In this case, the RWA amounts to neglecting the Bloch-Siegert shift component. It holds when ω_d is near ω_0, but the detuning is still far above than Ω_d. Out of this regime, taking only Ac-stark shift into account cannot be justified. To conclude, Bloch-Siegert shift is the consequence of the breakdown of the RWA for the far-detuned driving case.

2.1.4. OPEN QUANTUM SYSTEM

INTERACTION WITH THE ENVIRONMENT AND MASTER EQUATION

A quantum systems interacting with the surrounding environment is called an open quantum system. Here, the environment normally refers to the thermal reservoir which the systems are thermalized to. In this section, I define $\hat{\rho}_{s,r}$ and $\hat{H}_{s,r}$ as the density matrices and Hamiltonians of the system and the reservoir. I also define the interaction Hamiltonian between the system and the reservoir as $\hat{H}_{sr}$. The thermal reservoir has a huge number of DOF, and therefore completely solving the total system's equation of motion is unfeasible in general. However, the difficulty is largely alleviated if several approximations are valid. One is Born approximation, which assumes that the total system's[2]

[2]The total system here is often called 'world' and its Hamiltonian is called 'world Hamiltonian'.

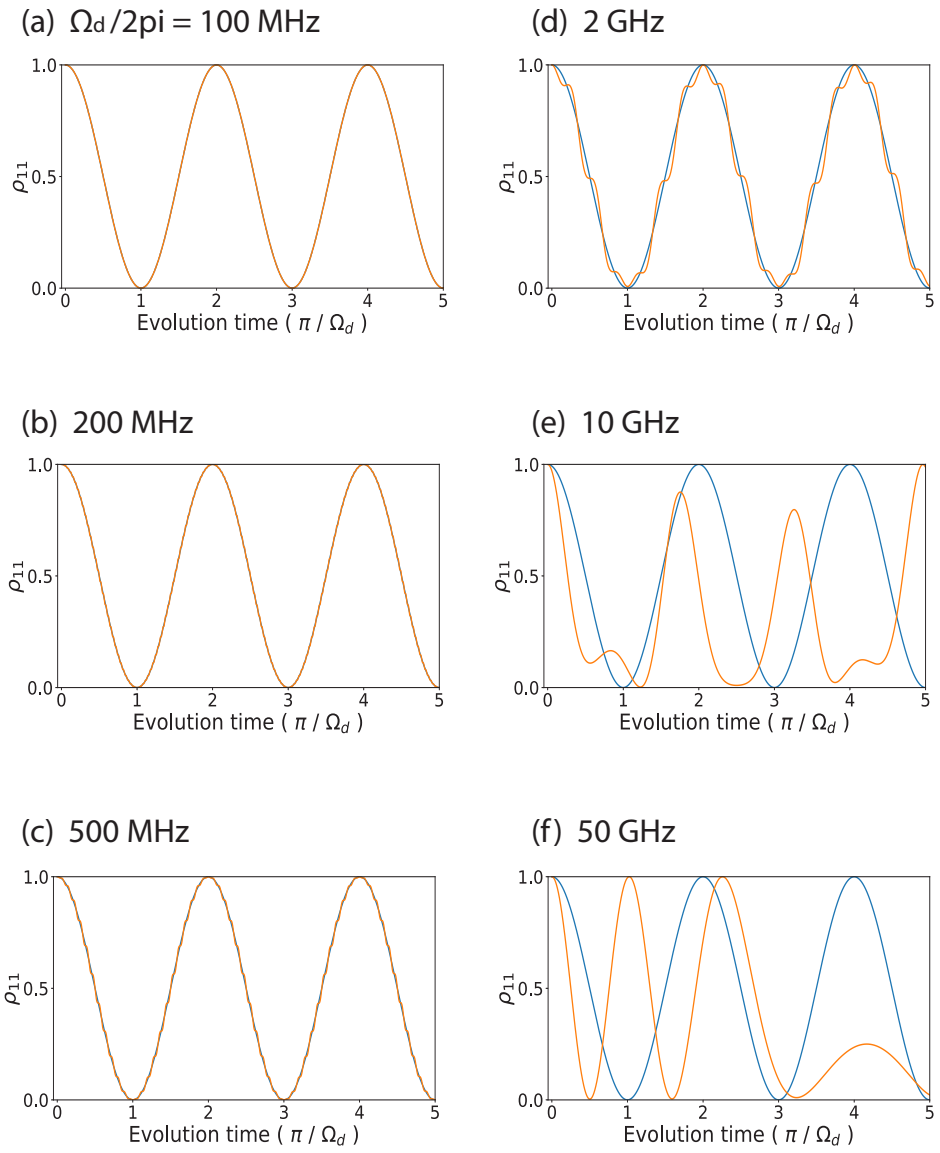

Figure 2.2: Dynamics of a resonantly driven TLS with sweeping the driving amplitudes.Yellow lines indicate the numerically calculated dynamics with the full Hamiltonian and blue lines indicate that with the RWA Hamiltonian.

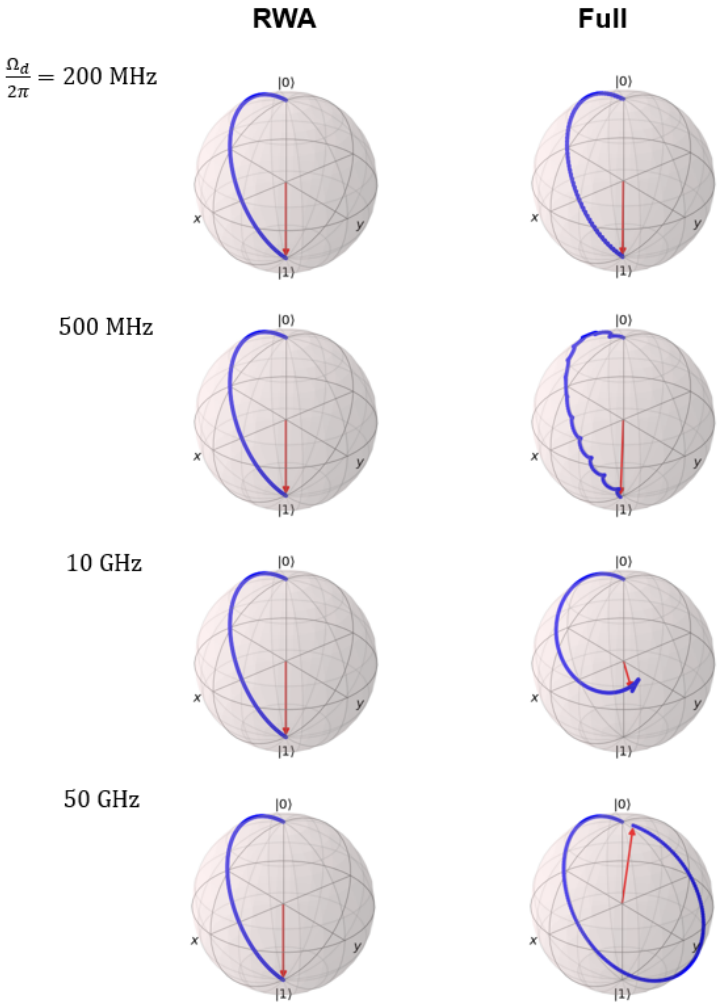

Figure 2.3: Traces of the quantum states represented on a Bloch spheres. The traces describe the dynamics of a driven TLS with several driving amplitudes. Time duration is $0 < t < \pi/\Omega_d$

.

density matrix $\hat{\rho}_{tot}$ is a direct product of $\hat{\rho}_s$ and $\hat{\rho}_r$ for all time, that is $\hat{\rho}_{tot}(t) = \hat{\rho}_s(t) \otimes \hat{\rho}_r$. Here, $\hat{\rho}_r$ does not have the time-dependence since it is assumed to be stationary. The second one is Markov approximation which amounts to assuming that the reservoir has a very short memory compared with the time scale of the system's dynamics. From this, the system's dynamics only depends on the current state and we can neglect the effects of its history (non-Markovian effects). These two assumptions are called Born-Markov approximation together.

Assisted by the Born-Markov approximation, analytically solving the equation of motion of the total system becomes tractable. After tracing out the reservoir state, we finally come to Lindblad master equation (LME), a kind of extension of Schrödinger equation. The LME reads,

$$\begin{aligned}\frac{d\hat{\rho}_s}{dt} = & \underbrace{-i\left[\hat{H}_s(t), \hat{\rho}_s(t)\right]}_{\text{Liouvillian, unitary evolution}} \\ & \underbrace{+\sum_n \frac{1}{2}\left(2\hat{C}_n\hat{\rho}(t)\hat{C}_n^\dagger - \hat{\rho}(t)\hat{C}_n^\dagger\hat{C}_n - \hat{C}_n^\dagger\hat{C}_n\hat{\rho}(t)\right)}_{\text{Lindbladian, non-unitary evolution}}.\end{aligned} \tag{2.18}$$

In the above equation, I omit the generalized Lamb shift term. The collapse operators $\hat{C}_n$ are determined by the types and strength of the interaction between the system and reservoir.

The interaction with the reservoir causes the non-unitary part of the equation (Lindbladian). I also want to remark that the time evolution of the open quantum systems cannot be captured by Eq. 2.3 which only works for the closed quantum systems and pure quantum states. The non-unitary dynamics is unfortunately irreversible. Accordingly, we cannot retrieve the system's quantum states once it undergoes the interactions with its environment. That is why isolating the system from the external environment is of great importance in most quantum experiments. Nonetheless, there are a few cases where we benefit from the interactions with reservoir.

CONSEQUENCES IN TWO-LEVEL SYSTEM

Let us define a two-level system of a Hamiltonian, $\hat{H}_{\text{TLS}} = -\frac{\omega_0}{2}|0\rangle\langle 0| + \frac{\omega_0}{2}|1\rangle\langle 1|$ with collapse operators $\hat{C}_1 = \frac{1}{\sqrt{T_1}}|0\rangle\langle 1|$ and $\hat{C}_2 = \frac{1}{\sqrt{T_2^*}}(|0\rangle\langle 0| - |1\rangle\langle 1|)$. The first collapse operator $\hat{C}_1$ leads to a decay process from $|1\rangle$ to $|0\rangle$ and T_1^{-1} is a decay rate. The time evolution of ρ_{11},

$$\dot{\rho}_{11} = -\frac{1}{T_1}\rho_{11}, \tag{2.19}$$

,and ρ_{11} indicates the population of the state $|1\rangle$. $\hat{C}_1$ induces not only the decay in the population ρ_{11}, but also the decay in the coherence $\rho_{12} = \rho_{21}^*$, called decoherence or dephasing. The decay rate of ρ_{12} (i.e. dephasing rate) by $\hat{C}_1$ is a half of $\frac{1}{T_1}$, that is,

$$\dot{\rho}_{12} = -\frac{1}{2T_1}\rho_{12}, \tag{2.20}$$

without $\hat{C}_2$. The collapse operator $\hat{C}_2$ accounts for an additional dephasing not relavant with $\hat{C}_1$ and does not affect the population decay. To distinguish them, we call this additional one as pure dephasing. Consequently, the total dephasing rate is given by $\frac{1}{T_2} = \frac{1}{T_2^*} + \frac{1}{2T_1}$, and the time evolution of the coherence is governed by,

$$\dot{\rho}_{12} = -\frac{1}{T_2}\rho_{12}. \tag{2.21}$$

The collapse operator $\hat{C}_1$ is originated by the energy exchange between the system and reservoir. In the above case, $\hat{C}_1$ only induces the decay from excited to ground state, meaning that the system always loses it energy to the reservoir. This implies that the temperature of the reservoir is absolute zero, and therefore the system cannot get any energy from the reservoir. In order to describe the TLS submerged in the reservoir with non-zero temperature T, then $\hat{C}_1$ must be replaced with two collapse operators, $\hat{C}_{10} = \frac{1}{\sqrt{T_1^{10}}}|0\rangle\langle 1|$ and $\hat{C}_{01} = \frac{1}{\sqrt{T_1^{01}}}|1\rangle\langle 0|$. Here, $1/T_1^{nm}$ is the decay rate from n to m states. Then the rate equation for the population of the TLS is given by,

$$\dot{\rho}_{11} = -\frac{1}{T_1^{10}}\rho_{11} + \frac{1}{T_1^{01}}\rho_{00}. \tag{2.22}$$

Both T_1^{01} and T_1^{10} should be determined such that the relation $\rho_{00}(t\to\infty)/\rho_{11}(t\to\infty) = e^{\hbar\omega_0/k_BT}$ satisfies. Here, k_B refers to Boltzmann constant. Under ideal situation, when the system is completely isolated from any other physical objects except the thermal bath at the temperature T, we can more quantitatively describe the Eq. 2.22 by using Einstein's A and B coefficients like below,

$$\dot{\rho}_{11} = -A\rho_{11} - B\xi(\omega_0)\rho_{11} + B\xi(\omega_0)\rho_{00}, \tag{2.23}$$

where $\xi(\omega)$ indicates the energy density of thermal radiation at the angular frequency ω.

$$\xi(\omega) = \frac{\hbar}{c^2\pi^2}\frac{\omega^3}{e^{\hbar\omega/k_BT}-1}. \tag{2.24}$$

2.2. LINEAR CIRCUITS AND QUANTIZATION

This section provides the explanation on how the quantum theories are applied to microwave electrical circuit systems. Using the mechanical analogy of the circuit, its quantization is quite straightforward. I deal with only the linear circuit elements here. The nonlinear element, which counts for realization of qubits, will be introduced in section 2.3.

2.2.1. LUMPED ELEMENT

When the size of the circuit element is much smaller than the circuit's operating wavelength, we can use the lumped element model to describe it. Two examples are introduced in figure. 2.4, one is a lumped-capacitor model and the other is a lumped-inductor model. As particle's position and momentum form a canonical pair and represent the

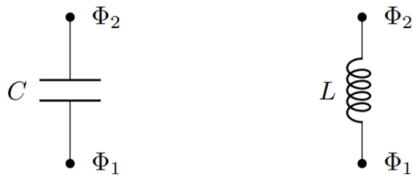

Figure 2.4: Lumped models of linear circuit elements. (Left) A lumped-capacitor model. (Right) A lumped-inductor model. $\Phi_{1,2}$ indicate the superconducting phases at each ends of both elements.

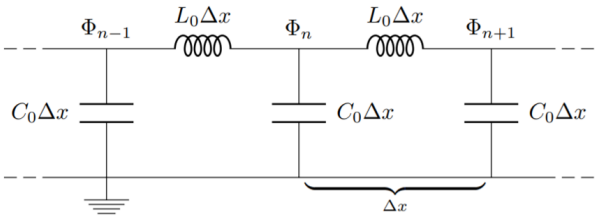

Figure 2.5: Transmission line depicted by the array of lumped-capacitors and inductors.

physical state of its motion, we can use the voltage (V) and current (I) across the circuit elements to do the same thing. Instead of V and I, we can also use the charge ($Q = Q_1 - Q_2$) and flux ($\Phi = \Phi_1 - \Phi_2$) alternatively[3]. In quantizing the superconducting circuits, the latter pair is more preferred. Both Q and Φ are related with V and I by the below equations,

$$\begin{aligned} \frac{dV}{dt} &= \Phi, \\ \frac{dQ}{dt} &= I. \end{aligned} \tag{2.25}$$

The charging and inductive energies stored in the capacitor and inductor (H_C and H_L respectively) are then given by $H_C = \frac{Q^2}{2C}$ and $H_L = \frac{\Phi^2}{2L}$. When the capacitor and inductor are connected in parallel (parallel LC resonator), the total Hamiltonian becomes $H_{LC} = H_L + H_C$. Circuit quantization is simply made by promoting Q and Φ to quantum operators $\hat{Q}$ and $\hat{\Phi}$ respectively. For $\hat{H}_{LC}$, the Hamiltonian takes the same form of a Harmonic oscillator. Therefore we can just follow the same approaches used for the Harmonic oscillator. We can interpret the n-th energy eigenstates of the LC resonator as n photons stored there. A single photon's energy in this case is given by $\hbar\omega_r$, where $\omega_r = 1/\sqrt{LC}$ is the resonant frequency of LC resonator.

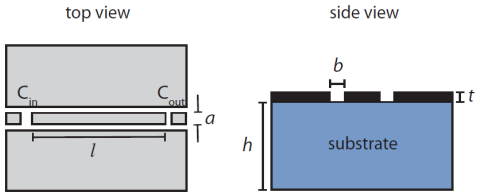

Figure 2.6: Schematics of a gap coupled co-planar waveguide resonator. (a) Top view. (b) Side view.

2.2.2. DISTRIBUTED ELEMENT

The circuit elements that cannot be described by the lumped element model are called distributed elements. One example is transmission line, necessary to feed the microwave power on the targets. It can be described by the array of lumped-capacitors and inductors as shown in figure 2.5. When proper boundary conditions are set at two specific points on the transmission lines, we can define resonator modes between the points. Co-planar waveguide resonator is an example of this transmission line based resonator, we deal with here.

CO-PLANAR WAVEGUIDE RESONATOR

Co-planner waveguide (CPW) is a type of the transmission line made out of 2-dimensional metal sheets. It consists of a center pin, ground plates, and substrate layers. The impedance of CPW is determined by the geometry, dielectric constant of the substrate, and kinetic inductance of the metal (if the metal is superconducting). It also provide a convenient way to construct a resonator (CPW resonator). One approach is given in figure 2.6(a). The gaps at each end of a CPW resonator set boundary conditions, and only the electromagnetic wave at certain frequencies can exist there. These form the modes of the CPW resonator, and each of them can be considered as LC resonators.

The design given in figure 2.6(b) is called gap-coupled $\lambda/2$ CPW resonator. There are other approaches to define resonators, and these are nicely illustrated in [32]. The advantage of the gap-coupled design is that one can easily calculate its coupling rates to the external transmission lines. Only the capacitance between them is needed, and this can be done with the static electromagnetic simulations, without any RF domain simulations.

2.3. ARTIFICIAL ATOMS WITH SUPERCONDUCTING CIRCUITS.

The term “Artificial atom" normally refers to a system where we can define a two-state subsystem, in other word, a qubit. The qubit defined in superconducting circuits is called superconducting qubit. For this, we need a nonlinear circuit element, and Josephson junction has a role as such. Of many superconducting qubit designs, we explore the one based on Cooper pair box (CPB) here. Transmon qubit is one specific case of CPB based superconducting qubit, which we especially focus on in this thesis. The circuits mimic cavity quantum electrodynamics (QED) systems when combining superconduct-

[3] Q_n and ϕ_n mean the charge and flux at the node n of the circuit.

ing qubits and resonators. Naming after cavity QED, the study on such a circuit configuration is called circuit QED.

2.3.1. JOSEPHSON JUNCTION

To realize artificial atoms out of the circuits, we cannot exclude Josephson junction (JJ). A JJ is comprised of two superconducting metal parts, which are disconnected from each other by an insulator layer. If the layer is thin enough, then the wavefunction of the cooper pairs can stretch over both parts as depicted in figure 2.7. As a result, the wavefunction's phase on both superconductor (call $\phi_{\text{left,right}}$ respectively) is correlated. We can define the Josephson phase $\phi = \phi_{\text{left}} - \phi_{\text{right}}$, and it relates the voltage and current over the insulator as described in the below equations,

$$\begin{aligned} V &= \frac{\Phi}{2\pi}\frac{d\phi}{dt}. \\ I &= I_0 \sin\phi. \end{aligned} \tag{2.26}$$

Here, I_0 is the maximum current through the JJ determined by the JJ's geometry. $\Phi_0 = \pi\hbar/e$ is called flux quanta. Above this value, all the relations in Eq. 2.26 breakdowns. The Josephson phase ϕ is directly proportional to the flux Φ, $\phi = \frac{2e}{\hbar}\Phi$. The total energy stored in the JJ (therefore Hamiltonian H_J) is given by,

$$H_J = \int V I dt = -E_J \cos(2\pi\frac{\Phi}{\Phi_0}) = -E_J\cos\phi, \tag{2.27}$$

where $E_J = I_0\Phi_0/2\pi$, called Josephson energy. Capturing the lowest order term (excluding the constant term), H_J can be approximated by,

$$H_J \approx \frac{E_J}{2}\phi^2 = (\frac{2\pi}{\Phi_0})^2\frac{E_J}{2}\Phi^2. \tag{2.28}$$

This form looks after H_L, and thus we can invoke to define Josephson inductance $L_J = (\Phi_0/2\pi)^2 E_J^{-1}$. The nonlinear part in Eq. 2.28 [4] is the heart to realize qubits. Meanwhile, for ideal superconductor, all the electrons are paired up into Cooper pairs, and therefore it is useful to define $n = -Q/2e$ as the number of Cooper pairs.

As we did with linear circuit elements, quantization of JJ can be done just by promoting the canonical variables to quantum operators. It is conventionally preferred to use n, ϕ instead of Q, Φ for simplicity when JJs are involved in the circuit. In an operator form, the Hamiltonian of the JJ can be expressed by, $\hat{H}_J = -E_J\cos\hat{\phi}$. In the meantime, based on the canonical relation $[\hat{n}, \hat{\phi}] = i$, we can express $\cos\hat{\phi}$ with $|n\rangle$, the eigenstates of $\hat{n}$. Then, $\hat{H}_J$ can be given by,

$$\hat{H}_J = -\frac{E_J}{2}(|n+1\rangle\langle n| + |n\rangle\langle n+1|). \tag{2.29}$$

This expression is much convenient for computing the eigenenergies when the JJ is combined with other shunt capacitors.

[4] The 4th and higher order terms of Φ.

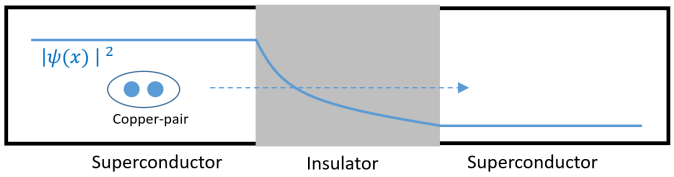

Figure 2.7: A schematic description of a Josephson junction. The blue curve depicts the probability density of the Cooper pair.

2.3.2. FROM COOPER PAIR BOX TO TRANSMON

A circuit diagram of the Copper pair box (the simplest charge qubit configuration) is given in figure 2.8(a). The Hamiltonian of the circuit is given by,

$$\hat{H}_{\mathrm{CPB}} = 4E_C(\hat{n} - n_g)^2 - \frac{E_J}{2}(|n+1\rangle\langle n| + |n\rangle\langle n+1|). \tag{2.30}$$

Here, $E_C = e^2/2C$ is defined as a counterpart of E_J, called the charging energy. $2e \times n_g$ is the offset charge existing at the capacitor. It is important to introduce n_g here since the offset charge is always fluctuating due to the external electrical noise in real situations. Figure 2.8(b) gives the eigenenergies of $\hat{H}_{\mathrm{CPB}}$ as a function of n_g. It is interesting to see how the energy level structures change with respect to the dimensionless system parameter E_J/E_C.

When E_J and E_C are comparable to each other, we say the system is in the 'charge' limit. We can see the significant non-equality in the energy level spacing, which is a good property to define qubit states. The downside of working in the CPB regime is that the transition energies are too sensitive to n_g. Therefore, the qubit's dephasing rate largely depends on n_g dispersion[5]. We can loosen the problem using an additional gate electrode and biasing the n_g to half integers. These bias points are called charge sweet spots. However, even at the sweet spots, the predicted coherence time is only 1 μs [20] in the charge qubit regime ($E_J = E_C$) with the typical n_g dispersion [20], and usual circuit parameters. When $E_J \gg E_C$ satisfies, the system is in the transmon limit. In this regime, the transition energies become insensitive with respect to n_g, and consequently the qubit states become more robust against n_g dispersion. For example, the theoretical prediction of the coherence time limited by the n_g dispersion is 40 μs when $E_J/E_C = 85$, even larger than that of charge qubits. The downside of the transmon is weak nonlinearity in the energy levels.

In the transmon regime, we can approximate the CPB Hamiltonian to $\hat{H}_{\mathrm{t}}$ by truncating the higher order ϕ terms larger than 4-th order in the $\cos\phi$,

$$\hat{H}_{\mathrm{CPB}} \longrightarrow \hat{H}_{\mathrm{t}} = 4E_C(\hat{n} - n_g)^2 + \frac{E_J}{2}\hat{\phi}^2 - \frac{E_J}{24}\hat{\phi}^4. \tag{2.31}$$

We can set n_g to be zero in the tramsmon regime since we already know its effect on the energy levels is negligible. If matching $\hat{n}$ and $\hat{\phi}$ to $\hat{p}$ and $\hat{x}$ respectively, the approximated Hamiltonian resembles the $\hat{H}_{\mathrm{Duff}}$. As we did in section 2.1.2, we can express transmon's

[5]The origin of this n_g dispersion is mainly the unknown 1/f electrical noise at the device.

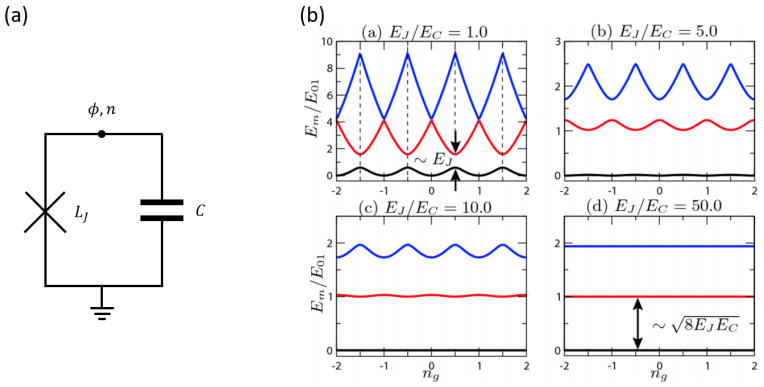

Figure 2.8: Charge qubit configuration based on a Josephson junction and the energy diagrams. (a) Simplified design of a charge qubit. The cross mark symbolizes a Josephson junction. (b) Retrieved from [20]. The energy levels as a function of offset charge n_g for different values of E_J/E_c.

Hamiltonian using creation and destruction operators. In the transmon case, those operators are defined by,

$$\begin{aligned} \hat{n} &= -\frac{i}{2}\left(\frac{E_J}{2E_C}\right)^{\frac{1}{4}}(\hat{a}-\hat{a}^\dagger) \\ \hat{\phi} &= \left(\frac{2E_C}{E_J}\right)^{\frac{1}{4}}(\hat{a}+\hat{a}^\dagger). \end{aligned} \tag{2.32}$$

Then the transmon Hamiltonian is represented by,

$$\hat{H}_\mathrm{t} = \hbar\omega_\mathrm{t}\hat{a}^\dagger\hat{a} - \frac{E_C}{12}(\hat{a}+\hat{a}^\dagger)^4. \tag{2.33}$$

Here, $\hbar\omega_\mathrm{t} = \sqrt{8E_JE_C}$. In the low excitation limit (up-to 3rd energy level), $\hat{H}_\mathrm{t}$ is reduced to,

$$\hat{H}_\mathrm{t}^\mathrm{low} \approx \hbar\omega_\mathrm{t}\hat{a}^\dagger\hat{a} - \frac{A_\mathrm{t}}{2}\hat{a}^\dagger\hat{a}^\dagger\hat{a}\hat{a}. \tag{2.34}$$

We call A_t anharmonicity of the tramsmon. Please note that A_t and E_C are generally different. They become identical only in the limit of $12\hbar\omega_\mathrm{t} \gg E_C$.

Figure 2.9 graphically depicts the difference between the LC resonator and transmon qubit in their energy levels. The transmon's potential deviates from parabola due to the 4-th order nonlinear term, resulting the anharmonicity in the energy levels. The two lowest energy states constitute qubit states. Nonetheless, the higher energy levels of the transmon affect the qubit's properties and dynamics significantly. Therefore, one must not indiscriminately apply the consequences from two-level systems to the transmon qubit case.

2.3.3. CIRCUIT QUANTUM ELECTRODYNAMICS

Circuit quantum electrodynamics (QED) is the study of the interaction between superconducting qubits and quantized resonator modes. In this section, we only consider the

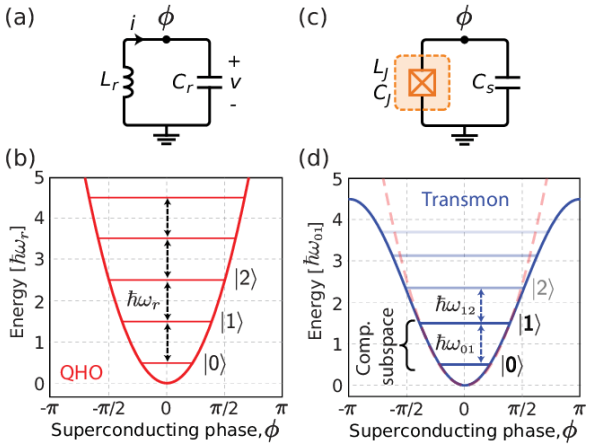

Figure 2.9: Retrieved from [33]. Difference in the energy levels between the LC resonator (a) and transmon qubit (b).

capacitive coupling case. In quantum mechanical view, the coupling mechanism between them can be understood that the resonator's field affects the offset charge n_g of the CPB. We can capture the interaction by changing n_g to $n_g + n_r(\hat{b}+\hat{b}^\dagger)$ in the CPB Hamiltonian $\hat{H}_{\mathrm{CPB}}$. We define $n_r = \frac{C_g V_0}{2e}$ to simplify the equations. Here, C_g is the capacitance between the CPB and resonator and V_0 is zero-point voltage fluctuation of the resonator. $\hat{b}$ is the destruction operator of the resonator mode. Then we obtain below expression to describe the CPB coupled to the resonator mode of an angular frequency ω_r.

$$\hat{H}_{\mathrm{cQED}} = \underbrace{4E_C(\hat{n}-n_g)^2 + E_J\cos\hat{\phi}}_{\text{CPB}} \underbrace{- g_0\hat{n}(\hat{b}+\hat{b}^\dagger)}_{\text{Interaction}} + 4E_C(n_g + n_r(\hat{b}+\hat{b}^\dagger))^2 + \underbrace{\hbar\omega_r\hat{b}^\dagger\hat{b}}_{\text{Resonator}}. \tag{2.35}$$

Here, g_0 is given by $8E_C n_r$. The fourth term in Eq. 2.35 is on the order of n^2, and hence results in only a tiny influence on the Hamiltonian.

Depending on the system parameters E_J,E_C, and n_g Eq. 2.35 is reduced to different forms. In the charge qubit limit when n_g is half-integers, $\hat{H}_{\mathrm{cQED}}$ can be reduced to the quantum Rabi model (QRM) like below,

$$\hat{H}_{\mathrm{cQED}}/\hbar \longrightarrow \hat{H}_{\mathrm{QRM}}/\hbar = \frac{\omega_0}{2}\hat{\sigma}_z - g(\hat{b}+\hat{b}^\dagger)\hat{\sigma}_x + \omega_r\hat{b}^\dagger\hat{b}. \tag{2.36}$$

Here, $\omega_0 = \sqrt{E_J^2 + [4E_C(1-2n_g)]^2}$ and $g/\hbar = eV_0C_g/(C_g+C)$. $\hat{\sigma}_x$ and $\hat{\sigma}_z$ are x and z components of Pauli operators. We approximate the CPB as a two-state systems with a transition frequency ω_0 in the above expression. The two-state approximation works well in the charge qubit limit thanks to the large nonlinearity. In the transmon limit, the system can be modeled by coupled Duffing and harmonic oscillators as given below,

$$\hat{H}_{\mathrm{cQED}}/\hbar \longrightarrow \hat{H}_{\mathrm{D-H}}/\hbar = \omega_t\hat{a}^\dagger\hat{a} + \omega_r\hat{b}^\dagger\hat{b} - g(\hat{a}+\hat{a}^\dagger)(\hat{b}+\hat{b}^\dagger) - \frac{E_C}{12}(\hat{a}+\hat{a}^\dagger)^4. \tag{2.37}$$

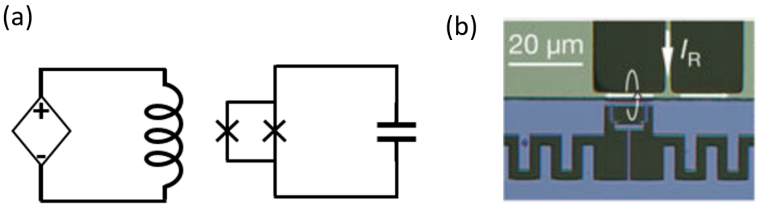

Figure 2.10: The frequency control of a qubit. (a) A schematic. A squid loop and a coil are inductively coupled. By adjusting the bias current applied to the coil, one can control the magnetic flux through the squid loop, leading to the change in the qubit frequency. For the fast control of the frequency, it is desired to use the on-chip flux line. (b) An optical microscopy image of the flux line realized in the device used in [35]

The definitions of $\hat{a}^\dagger$, $\hat{a}$, and ω_t are the same in 2.32 and 2.33. We set $n_g = 0$ as the offset charge hardly contributes the transmon's energy levels.

The system is in the dispersive coupling regime when the difference between the qubit's transition frequency (ω_0 or ω_t) and resonator frequency (ω_r) is much larger than g. In this regime, $\hat{H}_{\mathrm{QRM}}$ can be perturbatively diagonalized to[6],

$$\hat{H}_{\mathrm{QRM}}/\hbar \longrightarrow \frac{\omega_0}{2}\hat{\sigma}_z + 2\chi\hat{\sigma}_z(\hat{b}^\dagger\hat{b} + \frac{1}{2}) + \omega_r\hat{b}^\dagger\hat{b}. \tag{2.38}$$

Eq. 2.38 represents that the resonant frequency of the resonator depends on the qubit states. This property is extremely useful to detect the qubit's quantum states. Here, χ is called a dispersive coupling strength. When χ^{-1} is smaller than the decay time of the qubit and resonator, then we can say that the system is in a strong dispersive coupling regime.

The dispersive coupling regime is very important in circuit QED. It provide us with a way for non-demolition measurement. Depending on the qubit states, the resonance frequencies of the resonator are different, and therefore we can distinguish the states by probing the resonator. The advantage is that probing the resonator does not lead to any change in the qubit states. When the measurement outcomes tell the qubit is in the excited state, then it still remains in the excited state, not collapsing to the ground state. This allow the feedback control of the qubit states [34].

2.4. TUNEABLE LIGHT-MATTER INTERACTION WITH SUPERCONDUCTING CIRCUITS.

There are several avenues to achieve tunable interaction in a dispersively coupled qubit and resonator system. They are described in figure 2.11 one by one. One approach is to suddenly switch the qubit's transition frequency (ω_q, black curve) as depicted in figure 2.11(a). If the qubit is initially far-off resonant from the resonator transition frequency ω_r, then we consider qubit and resonator are effectively uncoupled. If the qubit's transition frequency jumps to ω_r, then the qubit and resonator become on-resonant and

[6] We can also perturbatively diagonalize $\hat{H}_{\mathrm{D-H}}$. This case will be more discussed in chapter 5.

the coherent state transfer begins. In this way, we can turn on and off the interaction between the qubit and the resonator. The other approach is to modulate the qubit's transition frequency as depicted in figure 2.11(b-c). When the modulation frequency ω_m satisfies the matching conditions, the sideband transitions between the qubit and resonator take place. These approaches require that the frequency of the qubit should be tunable within a short time scale. It is technically feasible if one employs superconducting qubits with SQUID loops and on-chip magnetic flux lines [35] as shown in figure 2.10. The sudden frequency switch was realized in [25] where the authors create Fock states in a superconducting resonator. Inducing the first order sideband transitions by flux modulation was proposed in [36] and experimentally implemented in [37]. Although above cases successfully demonstrate the state transfer from the qubit to the resonator, introducing the tunability in the transition frequency of qubit leads to the dephasing induced by the external noise.

On the other hand, we can also implement the tuneable qubit-resonator interface with a fixed frequency qubit using the external transverse driving fields. One specific case is desired in figure 2.11(d), where a red sideband transition is induced by two driving fields. When we have a matching condition $f_1 + f_2 = f_q - f_r$, where $f_{1,2}$ are the driving frequencies, the resonant transition between the qubit and resonator is on. In this thesis, I will intensively discussed on this scheme. Despite of its considerable advantage compared to the other approaches, the quantitative studies has still remained undone. Specifically, two systems will be considered, one is the dispersive quantum Rabi model and the other is dispersively coupled a transmon and resonator.

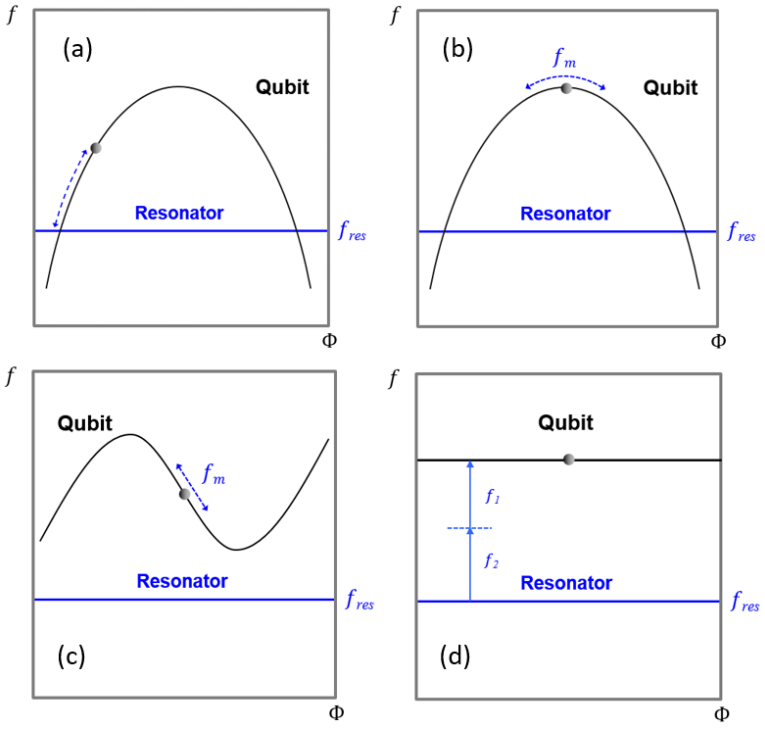

Figure 2.11: Possible schemes to implement tunable interactions between the qubit and resonator in a dispersively coupled qubit-resonator system. The black lines indicate the transition frequency of the qubit with respect to flux into the squid loop (Φ). We call this flux arc. The blue lines indicate the resonator's frequency. The gray circles mean the qubit's initial frequency. In all cases, qubit is initially sufficiently detuned from the resonator, and therefore we can consider the interaction is effectively truned off at the beginning. (a) A sudden shift of Φ turns on the interaction between the qubit and resonator. The interfaction is turned off when we bring the qubit is back. (b) The qubit is initially at the top of the flux arc. Modulating the qubit's frequency with f_m that satisfies the matching conditions can induce the coupling between the qubit and resonator. (c) The qubit is initially at the slope of the flux arc. Such a flux arc is given by an asymmetric squid. (d) This scheme does not need flux dependence. The arrows refer to external transverse driving fields. We can have transitions between the qubit and resonator when f_1 and f_2 satisfy the matching conditions.

3

DEVICE FABRICATION AND MEASUREMENT SYSTEM

This chapter provides the overall description of the experimental studies in this thesis. Illustrations of the device fabrication and the measurement system are present. The main components are transmon qubits and superconducting co-planar waveguide (CPW) resonators. The fabrication process for both is widely known and standardized. However, meticulous care is required during the fabrication process to have the great performance of the devices. In this chapter, I address not merely the fabrication procedures, but also the miscellaneous tips for the successful results. The measurement system part focuses on the technical apparatus including magnetic/radiation shields, dilution fridge, and microwave cable configurations.

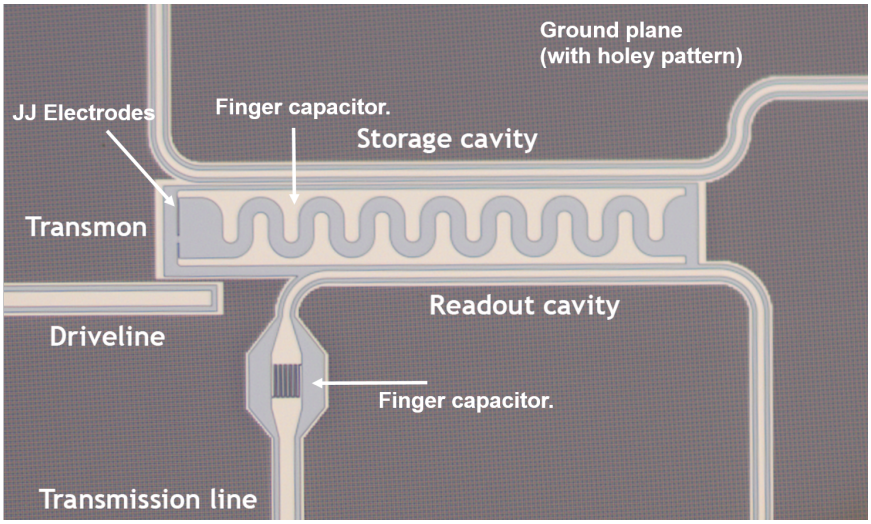

Figure 3.1: Optical microscopy image of the main part of a complete chip.

3.1. DEVICE FABRICATION

The essential circuit components on the chip are shown in figure 3.1. The transmon qubit consists of the finger capacitor and Josephon junction. It is coupled to two coplanar $\lambda/4$ waveguide resonators. Furthermore, there is a drive line directly coupled to the transmon. The resonators are coupled to transmission lines (only one of them is shown). The device is fabricated of 525 μm thickness Silicon substrate with 100 nm Niobium titanium nitride (NbTiN) film on the top of it. The Josephson junction is located between two electrodes, and comprised of Aluminium and Aluminium oxide. The holey pattern on the ground plane is intended to suppress and trap vortices that could appear by stray magnetic field.

The chip fabrication procedure can be divided into two parts. One is NbTiN base layer fabrication, and the other is evaporating Josephson junction. I shall separately illustrate them in the following sections. These are followed by a brief explanation on the chip packaging to interface the chip to commercial microwave electronics.

3.1.1. BASE LAYER

Figure 3.2 describes the fabrication steps for NbTiN base layer. The process begins with pure Silicon substrate[1]. NbTiN film is grown on the top of Silicon wafers in Evatec LLS800 Static evaporation machine[2]. NbTiN is a favorite material for high-quality factor planar waveguide resonators [39]. NbTiN-air interface is known to be very stable over time. Moreover, quasiparticle loss by infrared radiation is also relatively small due to its large superconducting gap frequency (1100 GHz) [39]. The next step is spin-coating an elec-

[1] We can also use Sapphire substrate. The pros and cons of both materials are discussed in the main text.
[2] For the NbTiN films used for devices in this thesis, the deposition step was done by Netherlands Institute for Space Research (SRON).

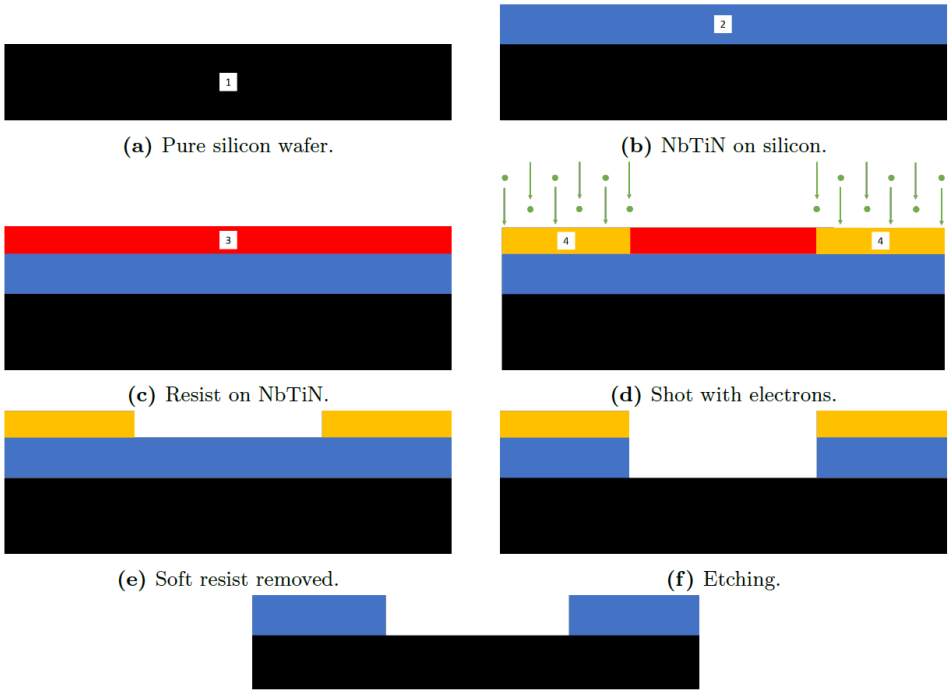

(a) Pure silicon wafer.

(b) NbTiN on silicon.

(c) Resist on NbTiN.

(d) Shot with electrons.

(e) Soft resist removed.

(f) Etching.

(g) Hard resist removed.

Figure 3.2: Retrieved from [38]. Fabrication steps for NbTiN base layer. 1 : Silicon, 2 : NbTiN, 3: E-beam resist, 4 : Resist exposed to E-beam.

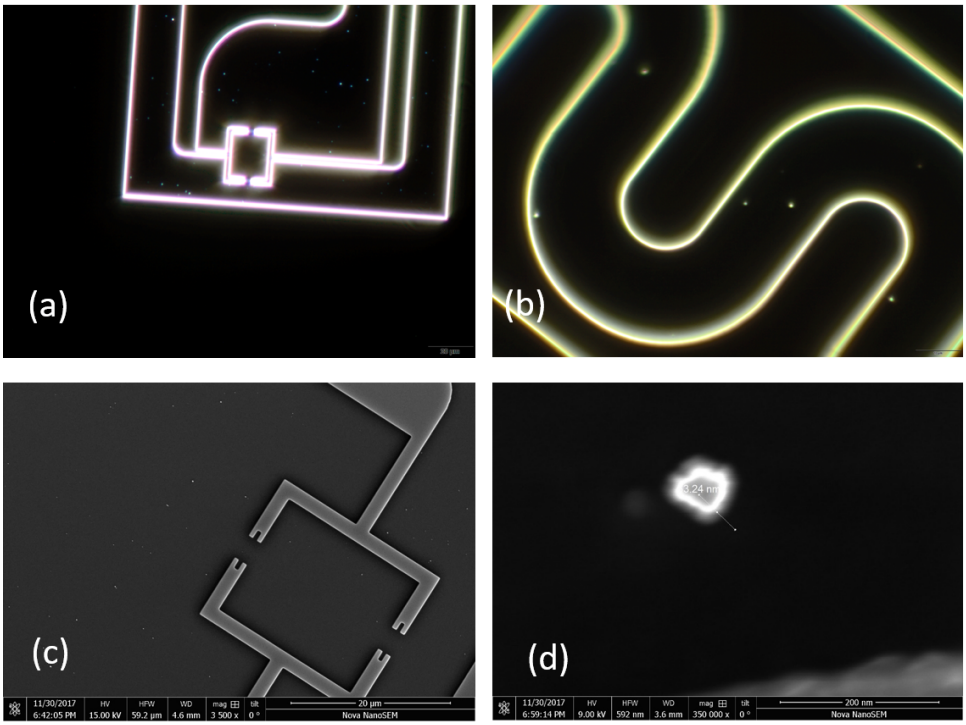

Figure 3.3: Optical microscopy (a-b) and SEM images (c-d) after reactive-ion etching when using PMMA as an E-beam resist.

tron beam lithography (EBL) resist on the NbTiN film. In the EBL process, focused electron beam (E-beam) forms patterns by modifying the resist's inter-molecular bonding structures. The resist on the area not exposed to the electrons is removed by developing solution.[3] Afterward, a reactive ion etching with SF_6 gas is used to completely remove the NbTiN. The base layer fabrication is completed as removing all the residual resist on the NbTiN and Silicon. The detail fabrication procedure and relevant information used for the devices in this thesis is given in Appendix A. Practical advice and tips for successful outcomes are given in the following subsections.

CHOOSING THE SUBSTRATE

The metal-substrate interface is known as the largest surface loss channel in planer resonator designs using NbTiN. Suppressing this loss channel is essential to realize microwave resonators with high-quality factors of more than 100k. Therefore, the surface of the substrates must be intensively cleaned before depositing the superconductors. For a Silicon wafer, the cleaning steps involve several acid cleaning. Hydrogen fluoride (HF) cleaning must be included as the last step before loading into the evaporation chamber. Once HF cleaning is done, we should load the cleaned wafer in the chamber right away

[3] Only true when using negative resist. For positive resist, the exposed area to the electrons is removed by developing solution.

since Silicon oxide is grown on the wafer otherwise. How quickly we load the wafer into the chamber affects the quality of the resulting resonators, as proven in [40]. Sapphire is more stable when exposed to air. Most importantly, Sapphire does not interact with oxygen, and consequently, no surface oxidation takes place. The typical cleaning procedure for Sapphire wafers is simpler than that of Silicon wafers. Even without HF cleaning step, the obtained quality factors of the resonators are comparable to that made on the Silicon wafers.

Although it seems that Silicon is a worse option as a substrate when considering only the preparation process, there are several advantages in using Silicon over Sapphire. For example, Silicon is a CMOS (Complementary metal–oxide–semiconductor)-compatible material, whereas Sapphire is not. Therefore, Silicon can be a better choice than Sapphire if we consider collaborative applications with CMOS technologies [41, 42]. Furthermore, since Silicon is conductive at room temperature, we do not suffer from side-effects that could happen by undesired electrostatic charges. For example, during EBL process, the electrostatic charges formed at the metal by the electron beam can distort the patterns. The distortion can be suppressed by using Silicon substrate since the electrostatic charges can escape through the Silicon substrates. For the same reason, SEM inspections with Silicon substrates are much less proven to damage the chips. The convenience in dicing is also one of the upsides when using Silicon. In the case of Sapphire substrates, we need to use diamond cutters, which is more expensive in general. However, this less-fragility of Sapphire can be an advantage in other perspectives.

FAILURE CASE STUDY

Although the optimized recipe I found during my PhD is provided in Appendix A, I will discuss some failure cases while optimizing the recipe and the issues that account for the failures. In choosing the EBL resist, I tried several types, such as AR-P series, AR-N series, and PMMA series. In general, the AR-N series works nicely with NbTiN. In the case of AR-P 6300-13, it sometimes causes issues after the RIE process. These issues did not show up when trying with Sapphire substrates. Therefore, we can conclude that an unknown collective effect with Silicon, resist, and NbTiN yields the issues. PMMA series were one of the most widely used resists before the advent of the AR series. I tried PMMA A8 specifically, and the decision was made based on the achievable thickness after spinning. However, RIE with this resist results in unidentified particles on the etched area as shown in figure 3.3. Figure 3.3(d) is a magnified image of the particle, and considering its shininess in the SEM inspection, they could be NbTiN debris. Even after cleaning with Nitric acid and HF, I could not see any improvement.

Figure 3.4 shows a nano-masking effect that I experienced after RIE process. In this case, I etched the chip two days after developing the resist layer. The particles appear only at the etched area and the shape is vertically elongated. The height of the particle is similar with that of NbTiN thinkness. Considering all these facts, I come to a conclusion that the depositions on the developed parts could act as undesired etching masks. In order to minimize the depositions, it is required to minimize the time between the developing and etching.

It is known that the surface of NbTiN is teflonized by SF_6 during the RIE process. One avenue to suppress this is using oxygen as a buffer gas together with SF_6. However,

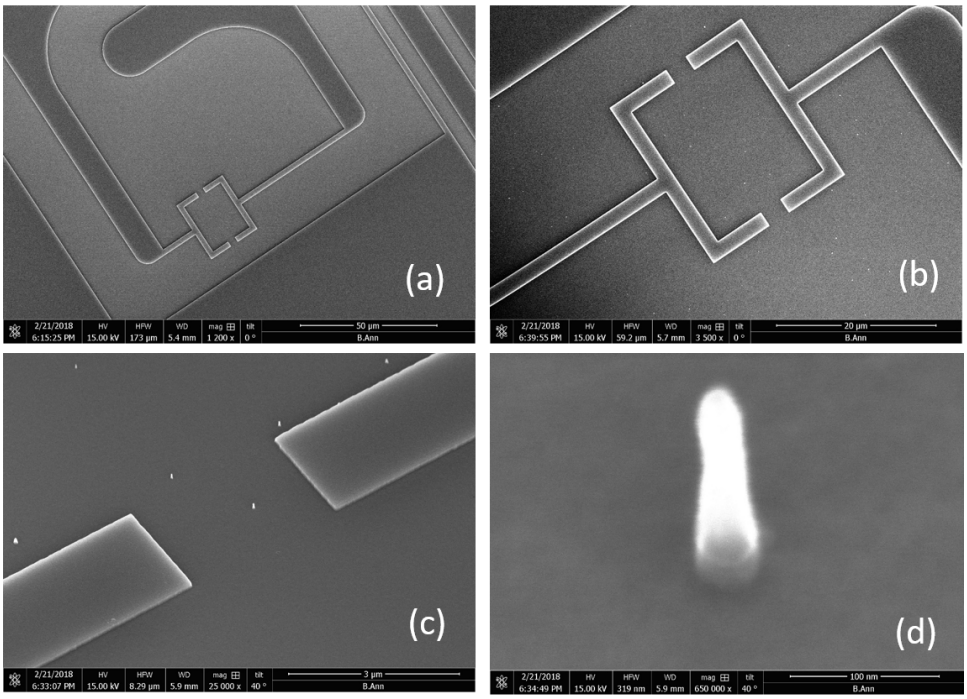

Figure 3.4: Nano-masking effect that appears after RIE process.

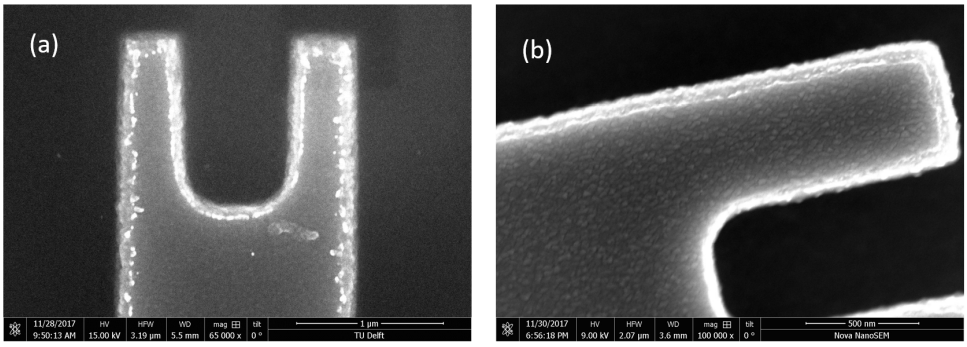

Figure 3.5: SEM images of NbTiN electrode without (a) and with (b) oxygen plasma cleaning after etching.

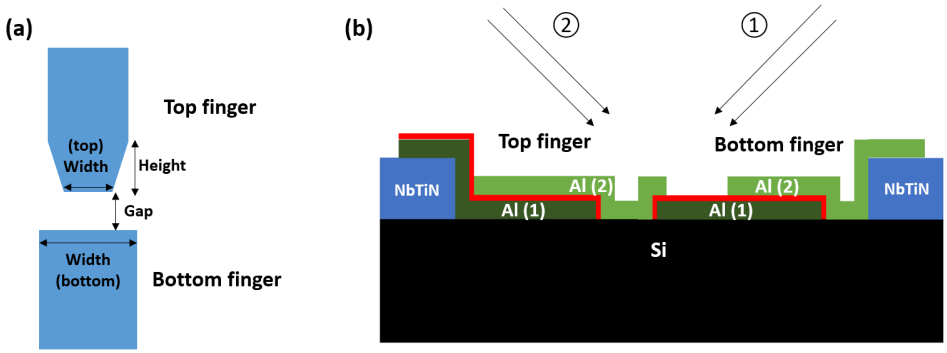

Figure 3.6: Al-AlOx-Al Josephson junction fabrication. (Left) Electron beam lithography pattern for evaporation mask. (Right) Schematic of double-angle shadow evaporation. The number refer to the sequence of deposition.

the teflon seems still remaining through the SEM inspection as shown in figure 3.5(a). The shiny area on a NbTiN electrode feature is suspected of the teflon. I conducted another fabrication where I performed the oxygen plasma cleaning immediately after RIE process (while maintaining the vacuum). Figure 3.5(b) shows the improved result as we cannot identify the shiny area in (a).

3.1.2. JOSEPHSON JUNCTION

Josephson junction is a key element of superconducting qubits. The fabrication method I follow during my PhD is mainly based on double-angle shadow evaporation and Niemeyer-Dolan technique [43]. I choose 'I' type Josephson junction design, which seems the ends of two fingers are overlapped. An oxidation layer is grown between the overlapped area. Figure 3.6(a) describes the design of EBL pattern for the evaporation mask and the schematic of double-angle shadow evaporation. A Dolan bridge is formed between top and bottom finger patterns. In order to make the bridge, I use a PMGI-PMMA double layer. Due to the under-cutting effect, PMGI under the 'gap' area is completely removed while the PMMA layer in this area still remains.

Figure 3.7(a) is an optical microscopy image after developing the resists. When zooming in the area between top and bottom finger pattern as in figure 3.7(b), we can identify the Dolan bridge. A schematic of Josephson junction evaporation is given figure 3.6(b) The first deposition forms the first Aluminum layer (dark green). Then, we inject the oxygen gas into the evaporation chamber to grow an oxidation layer (red). The second deposition forms the 2nd Aluminum layer (bright green), and consequently we have an overlap between the top and bottom fingers. Finally, we obtain the oxide layer between two fingers. It is vital to keep the interface between Aluminum and Silicon/NbTiN extremely clean. For this purpose, I first further clean the residual E-beam resists using oxygen plasma. Afterward, the developed area is cleaned by HF solution shortly before the Aluminum deposition. The time between the HF cleaning and deposition is extremely important. I normally finish this step within 5 mins. The process is completed

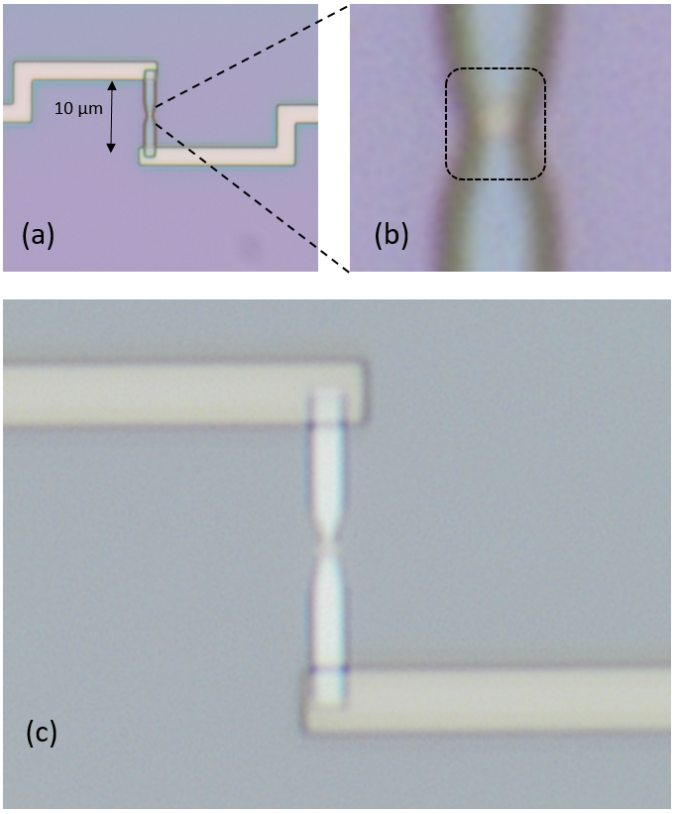

Figure 3.7: Optical microscopy images before and after Aluminum deposition. (a) After developing the E-beam resist. (b) Magnified the Dolan bridge part. We can identify the bridge by the slightly different color. (c) After Aluminum deposition and lift-off. The bright-white part is Aluminum and the dark-white part is NbTiN electrodes.

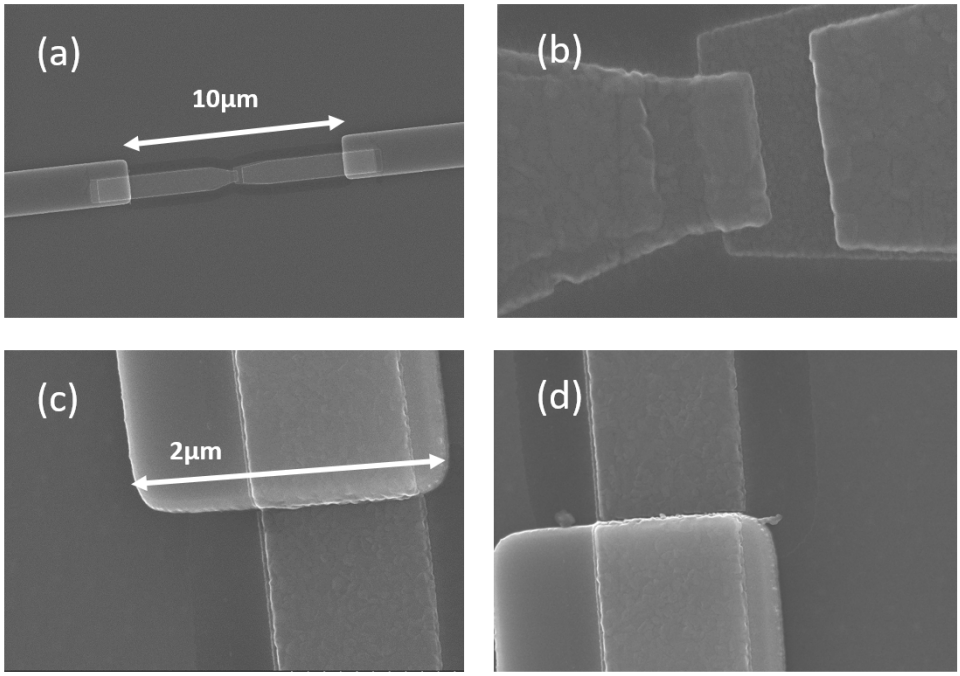

Figure 3.8: SEM images of a complete Josephson junction.[4] (a) An overall view. (b) The overlaps of top and bottom fingers of the Josephson junction. (c-d) Contacts between NbTiN electrodes and Aluminum. The dark shadow near Aluminum is caused by HF cleaning.

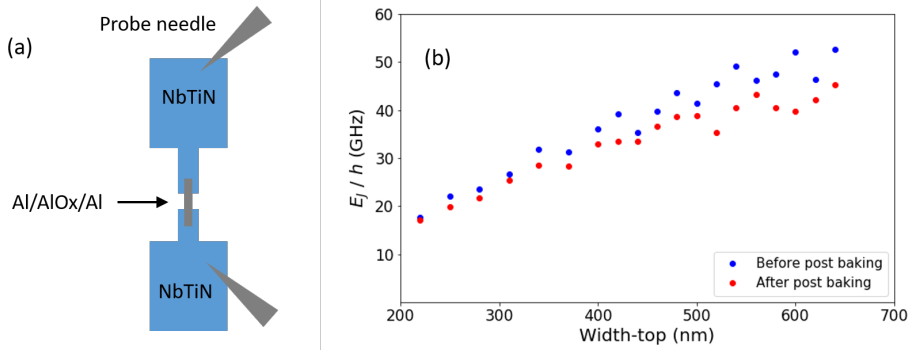

Figure 3.9: Room temperature resistance measurement of Josephson junctions. (Left) Experimental configuration. The Josephson junction under test is contacted to the NbTiN pads. Probe needles contact the pads, and then the junction is serially connected to a resistor with well known resistance. A sufficiently weak voltage not enough to break the junction is biased over the circuit of the serially connected junction and resistor. We can eventually extract the junction's resistance from the amount voltage applied to the junction. (Right) Measurement result. Estimated Josephson energy E_J is plotted with respect to the widths (top) of the evaporation masks corresponding Josephson junctions.

as lifting off all the deposited Aluminum except the Josephson junction part. The optical microscopy image after deposition and lift-off is given in figure 3.6(c). Figure 3.8(a-d) are SEM images of a complete Josephson junction. Please note that these are obtained from a different device other than the one in figure 3.7 (the geometry of NbTiN electrodes are different). The dark shadow around the Aluminum is due to the HF cleaning process.

The detail fabrication procedure and relevant information used for the devices in this thesis is given in Appendix A.

RESISTANCE MEASUREMENT

Even before cooling down, estimating the E_J of a Josephson junction is possible by measuring its resistance at room temperature. For Al-AlOx-Al Josephson junctions, we can rely on the Ambegaokar-Baratoff formula [44] that relates the Josephson energy E_J with the room temperature resistance R_N of the Josephson junctions. The formula reads,

$$E_J = \frac{1}{8e^2 R_N} \approx 140.3/R_N \text{ (GHz/k}\Omega\text{)}. \tag{3.1}$$

Figure 3.9(a) describes the experimental configuration for Josephson junction's resistance measurement. The resistance mainly depends on the top-widths of the E-beam patterns. Figure 3.9(b) shows the result of the measurement. I plot the estimated E_J from the measured resistance with respect to the top-widths of the E-beam patterns. By applying heat to Josephson junctions, we can vary their resistances to some extend. This process is called a thermal annealing. In figure 3.9(b), the red dots indicate the results after baking the Josephson junctions at 250°C for 5 mins. We can see the resistances are slightly downshifted after baking. Baking always downshifts the resistance. Furthermore, the subsequent baking does not lead to any further changes in the resistance.

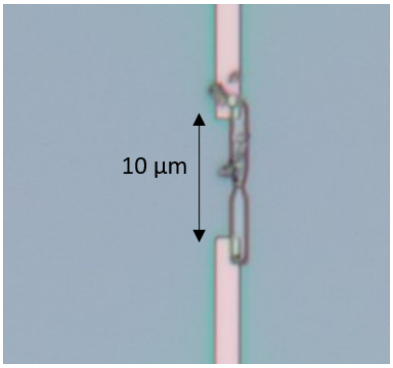

Figure 3.10: Optical microscopy image taken after developing the E-beam resist layer. Two issues can be found in this image. One is the pattern is misaligned, and the other is unknown flakes near the pattern.

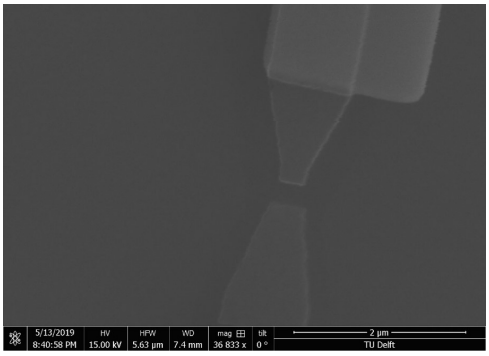

Figure 3.11: SEM image of failure case. In this case, Aluminum is deposited without changing the evaporation angle during the process.

FAILURE CASE STUDY

In this subsection, I shall introduce to two failure with discussions on the sources of the failure and how to improve them. In figure 3.10, the image shows the E-beam pattern after developing the resists. We can identify two problems in the picture. First, the patterned is not well aligned to the NbTiN electrodes. It seems that Aluminum can still make contacts to the electrodes even with this evaporation mask, but better is to have an optimal alignment for not only aesthetic reasons but also minimizing the probabilities to have an open circuit in case that Aluminum deposition is not sufficient. Second, we can find flakes around the pattern in figure 3.10. This happens only after developing the PMGI resist layer, and hence we may well suspect that the flakes are residual PMGI. The chance to have such flakes can be reduced by developing the PMGI layer for a longer time, but then the chance to destroy the Dolan bridge will increase either. Changes in the condition of the EBL machine or resist chemicals could account for this failure case. Therefore, the E-beam dose and developing time should be delicately optimized regularly. We could prevent the flakes by gently shaking the chip while developing the PMGI layer, but excessive shaking can also destroy the bridge. Sonication could be

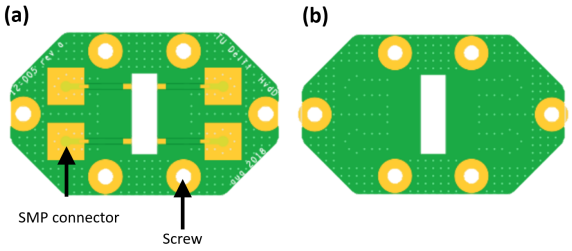

Figure 3.12: Printed circuit board design that suits a 3 by 10 mm chip. Top (a) and bottom (b) view. Gold-coated parts (yellow) are for SMP connectors and screwing. The green area means soldering mask.

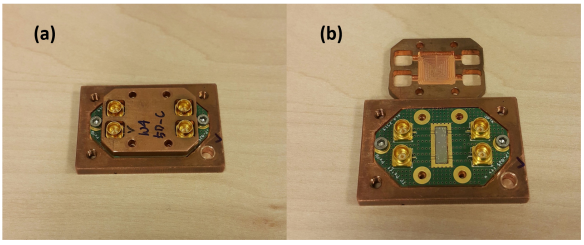

Figure 3.13: Completed device after packaging. A chip is placed on a microwave platform made by copper. The size of the platform is 4 by 2.7 cm. There is a copper cover on the chip to block external radiation. (a) When the copper cover is assembled. (b) When the cover is open. The size of the chip is 3 by 10 mm. The chip is wire-bonded to the PCB.

one possible solution to try. The other failure case is shown in figure 3.11. In this case, the Aluminum is deposited twice with the same evaporation angle. Since the deposition procedure for Josephson junctions is quite complicated, one can be easily lost during the process. Even before taking the SEM image in in figure 3.11, I was able to identify the disconnection through optical microscope. When measuring the resistance of these samples, I obtained very high resistance more than 100 kΩ.

3.1.3. PACKAGING

To feed microwave signals onto the chip and detect the transmitted signals from the chip, we must interface the chip to coaxial cables. This is implemented by wiring the chip to a printed circuit board (PCB). The PCB design used in this thesis is given in figure 3.12. The design suits a 3 by 10 nm size chip and consists of 4 microwave ports. The base of the PCB is comprised of FR-4, and a copper layer is coated on the top of it. Gold (yellow) and soldering mask (green) are coated on the copper layer. The gold coating is only on the places where SMP connectors and screws will be located. Gold and soldering mask are also coated on the backside of the PCB. The chip and PCB are finally placed on the microwave platform as in figure 3.13. The platform is comprised of copper and the size is 4 by 2.7 cm. The chip is covered by a copper sheet to protect it from infrared radiation. I discuss the effects of stray infrared radiation in more detail in the next section.

3.2. INFRASTRUCTURE

We must provide the qubit devices with extreme physical conditions. First of all, the device must be cooled down to the temperature below the critical temperature T_c of the constituent metals. Simultaneously, the devices need to be protected from external noisy environments for their best performance. This section provides descriptions of the measurement infrastructure that meets the above conditions while performing the measurements using room-temperature electronics.

3.2.1. MAGNETIC AND RADIATION SHIELD

The superconducting qubit devices should not be exposed to excessive magnetic noise and infrared radiation. First of all, the random fluctuation of the stray magnetic fields that penetrate the squid loops of the qubits increases the pure dephasing rate. Even if the stray fields are static, they are not welcomed as the qubits' frequencies are unwantedly biased away from the sweet spots. Another adverse effect is the creation of vortices. The magnetic field applied to the superconductor can create superconducting vortices when the field is strong enough, and the vortices degrade the quality factors of the qubits and resonators when the number is excessive. The magnetic dipole moment carried by vortices could also vary the magnetic flux through the squid loops when they are located near the qubits. The infrared radiation is also critical to the superconducting devices. It can create quasi-particles, and these are not anymore resistive-less, unlike Copper pair condensate. The formation of quasi-particles, therefore, results in energy loss.

Consequently, the qubits and resonators should be isolated from these environments as much as possible for their best performance. We need a shield surrounding the device to protect them from the environment. Unfortunately, it contradicts our need for device measurements. Apparently, if we completely isolate the device, then the measurements such as transmission and reflection spectroscopy are not possible. Designing the shield nicely compromising both requirements, is a tricky puzzle to solve. Furthermore, we also should satisfy other conditions. First, the device should be thermally anchored to the mixing chamber plate of the dilution fridge (the detailed explanations will be given in the next section). Second, the total proportion of the shield must suit the allowed space of the fridge. Third, we should take the mechanical stability of the system into consideration.

There is a typical shield design adopted among the experimentalists working with superconducting qubits [35]. The fundamental structure of the shield used in my PhD resembles that of the typical design, but there are some distinct features in detail. Figure 3.14 and 3.15 show the design of the shield drawn by CAD. The shield consists of a cold finger and four cylindrical layers having bottoms. The cold finger is used to mount the total structure to the plate of the dilution fridge. Setting a place where the packaged device is mounted is also essential. In the case of present design, the device is mounted at the bottom of the cold finger. The design intends for the device to see the bottom of the shield as usual. The innermost layer is comprised of copper, whose purpose is to block the radiation. The copper sheet on the top of the chip shown in figure 3.13 also has a radiation shielding effect, but usually not enough by itself. The next layer on the copper is comprised of Aluminium. This layer shields both the radiation and magnetic fields. The next two layers are comprised of Cryoperm, a magnetic shielding alloy that

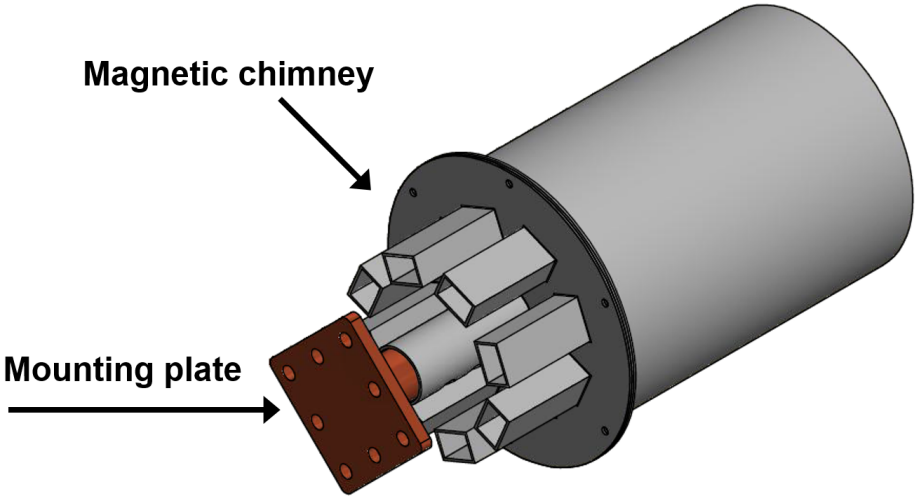

Figure 3.14: 3D CAD drawing of qubit shield and cold finger. Magnetic chimney and mounting plate are indicated by arrows.

shows high permeability at a cryogenic temperature. In order to feed the cable inside the shield, it is inevitable to have holes on the shields. To suppress the chance that the external fields get broken into the shield, there are magnetic chimneys, which are also made by Cryoperm. In order to maximize the radiation shielding effect, I coat inside the copper layer with Silicon Carbide (SiC). The SiC layer inside the copper cylinder absorbs the residual infrared radiation. The picture taken after completing the coating is given in figure 3.16. The detailed procedure of SiC coating is given in Appendix B.[5] There are several distinct features compared with the conventional designs. When fixing each layer onto the cold finger, I use threads instead of screws. This approach is known to be more stable under thermal contraction. Moreover, the present design has cable holders on the cold finger, which make certain that the cables are not disconnected from the device while closing the layers or cooling down the system. The picture is given in figure 3.17.

3.2.2. DILUTION FRIDGE AND WIRING

The device is cooled down at a Bluefors LD400 dilution fridge. The inside structure is shown in figure 3.18(a). Each goal-coated metal plates are thermalized at different temperatures, indicated by the numbers in yellow boxes. In practice, the observed temperatures are different by a 10-20 percent. The device is located at the lowest stage, called mixing chamber plate (MXC). We can identify the shield anchored below the MXC. To feed microwave signals into the device, we need to wire the stages with coaxial cables. Several factors should be taken into account when choosing the types of cables to use. It depends on the temperatures of the plates and the purpose of the lines. Figure 3.18(b) depicts a standard configuration usually adopted in superconducting qubit experiments.

[5] This step was largely assisted by Alessandro Bruno.

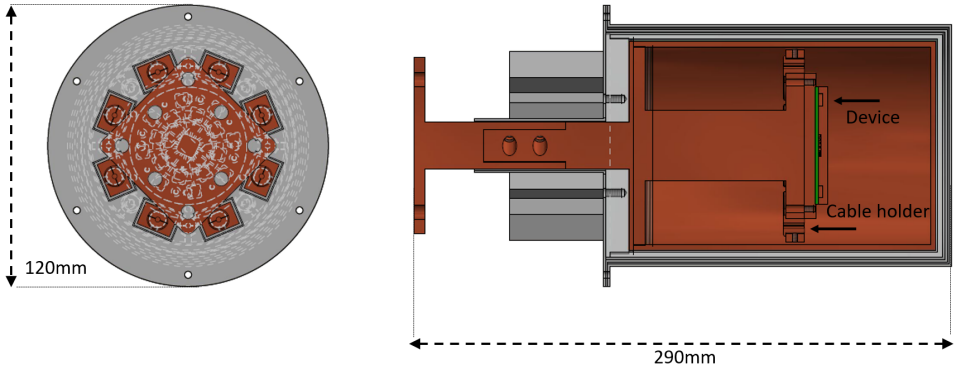

Figure 3.15: Top view and inside structure of qubit shield and cold finger. The mounted device and cable holder are indicated by solid arrows. Dimensions are indicated by dashed arrows.

Figure 3.16: A cylindrical copper shield with a gold coating on the surface. Inside of the shield is coated by SiC, which serves as an absorber for infrared radiation.

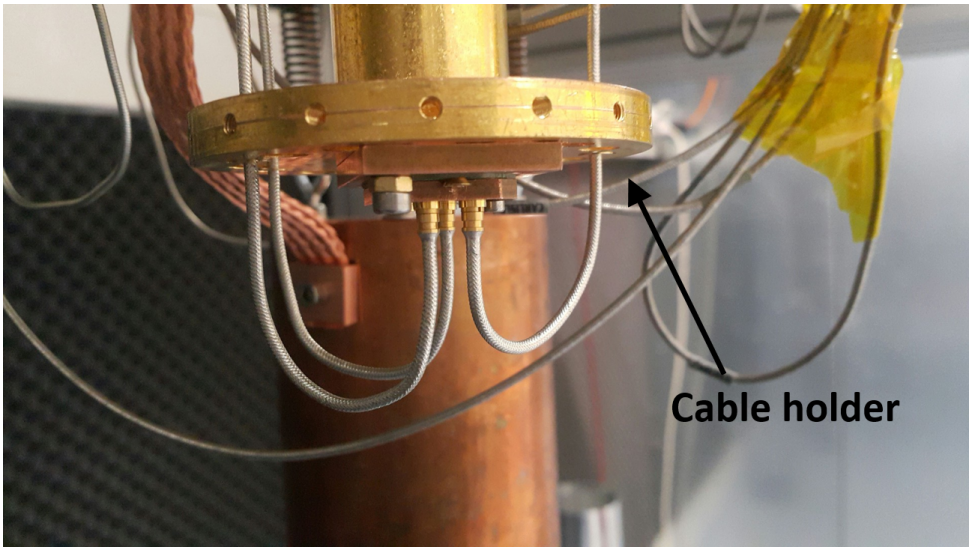

Figure 3.17: Device mounted on the bottom of cold finger. Black arrow indicates one of the cable holders.

In this thesis, we will explore the case when the qubit is strongly driven. If the driving power is excessive, then it could create undesired heat in the fridge. The heat is mainly generated from the attenuators, which include resistive components. Especially the heat from the attenuators at the MXC is the most critical. In order to circumvent this problem, we can adopt alternative configurations, as described in figure 3.19. In the left diagram, a directional coupler is installed at the MXC instead of an attenator. Approximate 99% drive power propagates to the auxline, and at the same time we can protect the device from the thermal noise created at the upper plates. In the right diagram, a reflective low pass filter (VLFX) is employed. We can choose a proper filter whose cutoff frequency is far below that qubit transition frequency, but lower than the desired driving frequencies. Thereby, we can drive the qubit with desired frequencies, and at the same time we can also protect the qubit from the thermal noise created at the upper plates.

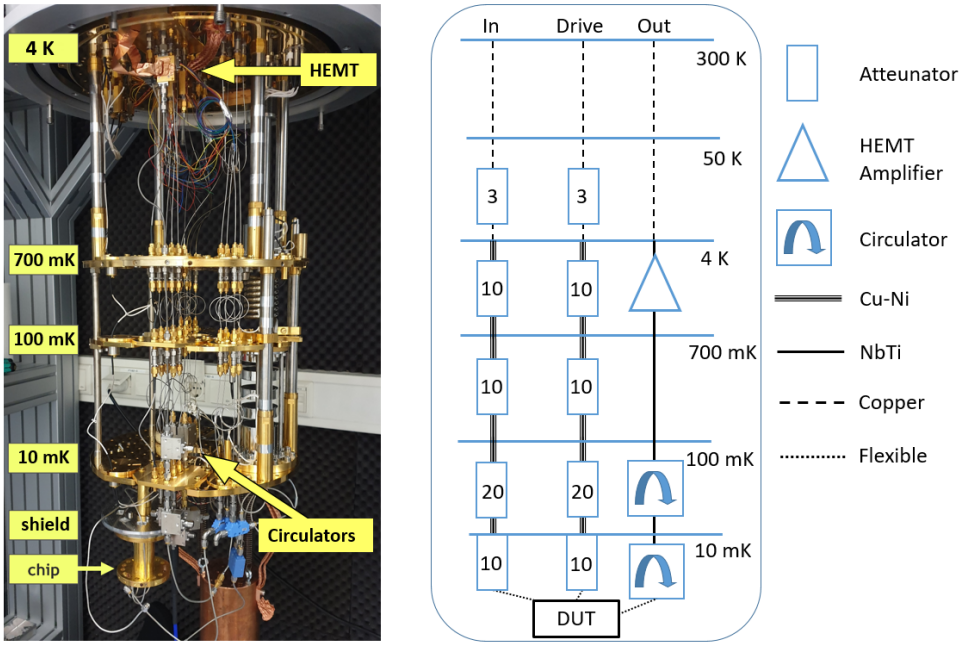

Figure 3.18: Inside look of dilution fridge (lelf) and conventional wiring diagram for superconducting qubit experiments (right).

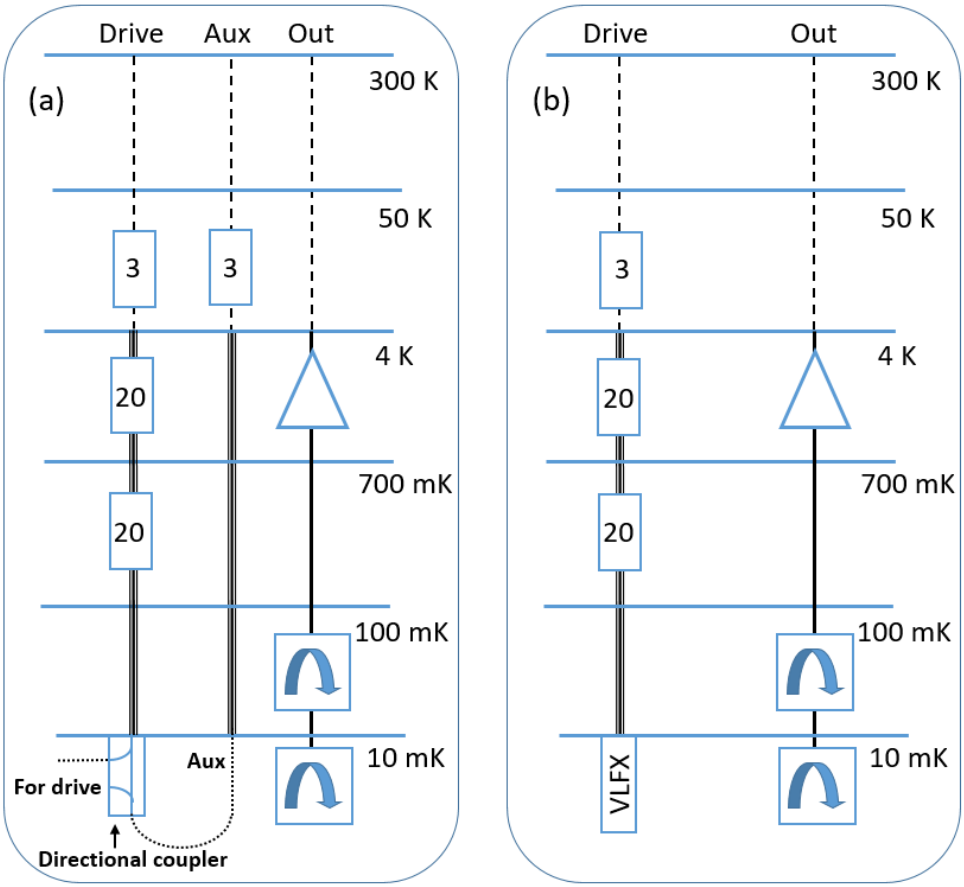

Figure 3.19: Alternative wiring configurations when it is necessary to feed high power into the device.

4

SIDEBAND TRANSITION IN THE QUANTUM RABI MODEL : QUANTITATIVE DISCUSSIONS BEYOND THE ROTATING WAVE APPROXIMATION

In this work, we analytically and numerically study the strongly driven quantum Rabi model (QRM) beyond the rotating wave approximation (RWA). We especially focus on the conditions when the external transverse drive fields induce the first-order sideband transitions. Inducing the sideband transitions between two different systems is an essential technique for various systems, including the QRM. Despite its importance, the analytical study that successfully explains the sideband transition rates in a driven QRM has not been reported yet. In our study, we analytically derive the sideband transition rates without the RWA, which is valid for all ranges of drive frequencies. Based on the perturbation theory to the 2nd order, our analytical derived formula agrees well with the numerical results as long as the drive amplitudes are moderate. Interestingly, we have found the collusion effect between co- and counter-rotating components in the drive Hamiltonian, which eventually accounts for significant corrections to the sideband transition rates expected from the RWA. One can precisely estimate the approximate sideband transition rates in the QRM only from the system and drive parameters based on our work. It will also contribute to the experiments with the systems described by the QRM.

Parts of this chapter will be submitted for publication.

4.1. INTRODUCTION

The quantum Rabi model (QRM) constitutes the essence of the light-matter interactions at the quantum level. It specifically describes the interaction between a two-state system (qubit) and a single cavity mode. The QRM has been extensively studied for fundamental interests as well as applications toward quantum information processing. QRM can describe many systems. It was originally formulated to mathematically describe cavity quantum electrodynamics (QED), studying the interaction between a trapped atom and cavity mode. Beyond atomic physics, it can also be extended to any other systems having an analogy with the cavity-QED, such as a quantum-dot in microcavities and various types of qubits transversely coupled to superconducting cavities. Moreover, the extended versions of the QRM have been widely investigated [45, 46].

One of the important aspects of studying the QRM is how to implement in-situ tuneable state transfer between the qubit and cavity mode (sideband transitions), which is crucial for quantum gate operation using qubit and quantum state engineering of the cavity. There are several ways to achieve this. One approach is to suddenly switch the transition frequency of the qubit (ω_q). If the ω_q is initially far-off resonant from the cavity transition frequency (ω_c), then we consider the qubit and resonator are effectively uncoupled. If the qubit's transition frequency jumps from ω_q to ω_c, then the qubit and cavity become on-resonant, and the coherent state transfer begins. In this way, by shifting the ω_q, we can turn on and off the interaction between the qubit and the cavity. The other approach is to modulate the qubit's transition frequency parametrically. When the modulation frequency ω_m satisfies the matching conditions($\omega_m = |\omega_q \pm k\omega_c|$, k is an integer), the sideband transitions between the qubit and cavity occur.

These approaches require that the frequency of the qubit should be tunable within a short time scale. It is technically feasible if one employs superconducting qubits with SQUID loops and on-chip magnetic flux lines. The sudden frequency switch was realized in [25], where the authors create Fock states in a superconducting cavity. Inducing the first-order sideband transitions by flux modulation was proposed in [36] and experimentally implemented in [37]. In all cases, the given system can be modeled by the QRM. Although the above cases successfully demonstrate the state transfer from the qubit to the cavity, introducing the tuneability in the qubit's transition frequency leads to another side-effect, the pure dephasing induced by external noise. For example, when the tuneability relies on the magnetic flux through the squid loops, the magnetic field noise into the loops accounts for the qubit's pure dephasing.

Meanwhile, we can also induce the sideband transitions without any frequency tuneability of the qubit and cavity, applying the external transverse drive at proper frequencies. This scheme is implementable with a fixed frequency qubit, and therefore the system is insensitive to the external noise and the qubit's dephasing rate is only limited by the qubit's decay rate [47]. There were a number of studies related to how the external drive fields affect the QRM or similar systems [48–51], but only a few studies quantitatively focus on the sideband transition rates [19, 52]. Especially for the first-order sideband transition in the QRM, the most demanded type of transition, the transition is dipole forbidden, and therefore only two or even number photon drive can induce the transition. This fact complicates the analytical derivation of the transition rates as we cannot capture the transitions simply by the first-order perturbation theory.

In this work, we performed a quantitative study on the first-order sideband transition in the QRM induced by two-photon transverse drive fields. We analytically derive the transition rates based on perturbative calculations up-to second order without relying on the rotating wave approximations in the Hamiltonian. We specifically investigate the parameter regimes familiar with circuit quantum electrodynamics (QED) experiments. In circuit QED, the frequency matching condition for sideband transitions often requires the drive parameters beyond the RWA, and therefore, one should not rely on the RWA in the analytical derivation of the transition rates. However, satisfactory quantitative study beyond the RWA regime has not been reported yet.

To our best knowledge, the initial attempt to analytically derive the two-photon sideband transition rates in circuit QED system was given in [19]. In that study, the charge qubit device dispersively coupled to the cavity was modeled by the QRM. However, the analytically derived transition rates are 4 fold smaller than the simulation results. In our work, we found that the RWA significantly distorts the calculated sideband transition rates. We also probe that the transverse drive field accounts for a secondary longitudinal drive effect, which also significantly contributes to the total sideband transition rates. The analytical predictions on the frequency matching conditions and sideband transition rates are well consistent with the numerical results when we have moderate drive amplitudes. Although our analytical model fails to explain the sideband transition rates as the drive strength becomes comparable to the detuning between the qubit and drive, it still yields more precise predictions than the model relying on the RWA.

This chapter is organized as follows. In Sec.4.2, we analytically derive the expected matching frequencies and sideband transition rates based on the perturbation theory up to second-order. The description of the numerical simulation performed in this study is given in Sec. 4.3. We compare the analytical and numerical calculation results in Sec. 4.4 with extensive parameter scanning. In this section, we also discuss the validity and limitation of our theory. We conclude our chapter in Sec. 7.

4.2. THEORETICAL DESCRIPTION

In this section, we derive the analytical formula to predict the matching frequencies and sideband transition rates. We investigate two possible schemes for the first order two-photon sideband transitions in the QRM, which Fig. 4.1 depicts. In the case that the drive field has only single frequency ω_d (monochromatic drive), the possible scheme for the first order sideband transitions is descried in Fig. 4.1a. The downside of this approach is that the only one possible drive frequency is allowed for given qubit and resonator frequencies. When using two different drive frequencies (bi-chromatic drive), we can have a flexibility in the frequency selection. Fig. 4.1b describes the case where one drive frequency is close to the resonator (ω_{dc}, resonator friendly), and the other one is close to the qubit (ω_{dq}, qubit friendly). The solid line and dashed lines refer to the bare and dressed energy states of the QRM respectively.

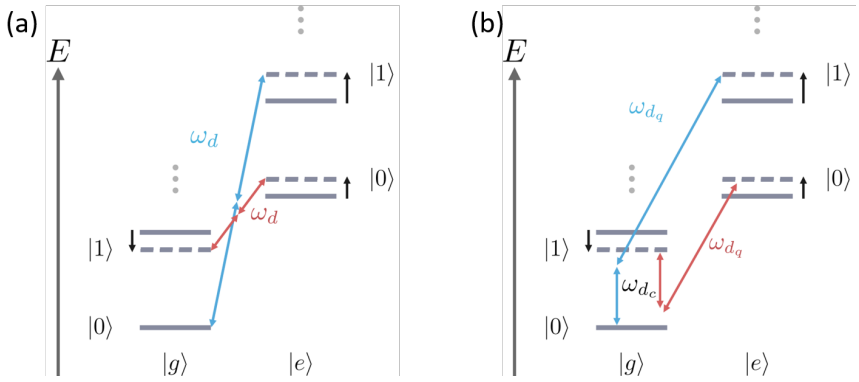

Figure 4.1: The first order red and blue sideband transitions in quantum Rabi model (QRM). The arrows indicate the external drives that satisfy the matching conditions for red and blue sideband transitions (red and blue arrow respectively). Two-photon drive is required since the first order sideband transitions in QRM are dipole forbidden. (a) Single frequency (monochromatic) drives. (b) Two frequency (bi-chromatic) drives. $|gn\rangle$ and $|en\rangle$ (corresponding dashed lines) represent the dressed states of the system. The black arrows indicate the frequency shifts induced by the external drive fields and and qubit-cavity coupling g. The bare states are indicated by solid lines.

4.2.1. SCHRIEFFER-WOLFF TRANSFORMATION

The transversely driven QRM Hamiltonian reads,

$$\hat{H} = \underbrace{\frac{\omega_q}{2}\hat{\sigma}_z + \omega_c \hat{a}^\dagger \hat{a} + g(\hat{a}^\dagger + \hat{a})\hat{\sigma}_x}_{\hat{H}_{\text{QRM}}} + \underbrace{\sum_i \Omega_d^{(i)} \hat{\sigma}_x \cos(\omega_d^{(i)} t)}_{\hat{H}_{\text{drive}}}. \tag{4.1}$$

Here, $\hat{\sigma}_{z,x}$ is z and x components of Pauli operators, and $\hat{a}$ is the cavity field operator. $\omega_{q,c}$ are angular frequencies of the qubit and cavity respectively. $\Omega_d^{(i)}$ and $\omega_d^{(i)}$ refer to i-th component of the drive amplitude and frequency. It is also useful to define $\epsilon_d^{(i)} = \Omega_d^{(i)}/2$, the drive strength for later. We are interested in the dispersive coupling regime where $|\omega_q - \omega_c| \gg g$. We are also interested in the drive frequencies $\omega_d^{(i)}$ are far off resonant to $\omega_{q,c}$, and the drive amplitudes $\Omega_d^{(i)}$ much smaller than the $|\omega_{q,c} - \omega_d|$. With these parameter conditions, $\hat{H}_d$ can be considered as a perturbation to $\hat{H}_{\text{QRM}}$. Then, we can approximately diagonalize the $\hat{H} = \hat{H}_{\text{QRM}} + \hat{H}_{\text{drive}}$ using Schrieffer-Wolff transformation [53]. The transform operator $\hat{U}$ takes a form of $\hat{U} = \exp(\beta^* \hat{\sigma}_+ - \beta \hat{\sigma}_-)$. We define $\hat{X} = \beta \hat{\sigma}_- - \beta^* \hat{\sigma}_+$ in the followings. The transformed Hamiltonian $\hat{H}'$ is given by,

$$\hat{H}' = \hat{U}\hat{H}\hat{U}^\dagger + i(\partial_t \hat{U})\hat{U}^\dagger. \tag{4.2}$$

The first term in Eq. 4.2 can be calculated using the Hausdorff expansion,

$$e^{\lambda \hat{X}} \hat{H} e^{-\lambda \hat{X}} = \hat{H} - \lambda[\hat{H}, \hat{X}] + \frac{\lambda^2}{2}[[\hat{H}, \hat{X}], \hat{X}] + \cdots \tag{4.3}$$

When $\beta \ll 1$, we can truncate the expansion to the low order of λ. In order to capture the two-photon transitions, we should include at least the terms which are $O(\lambda^2)$. In the meantime, the second term in Eq. 4.2 can be approximated by [19],

$$(\partial_t \hat{U})\hat{U}^\dagger \approx \frac{1}{2}(\beta^*\dot{\beta} - \beta\dot{\beta}^*)\hat{\sigma}_z + (\dot{\beta}\hat{\sigma}_- - \dot{\beta}^*\hat{\sigma}_+). \tag{4.4}$$

$\hat{H}'$ is then expressed by,

$$\begin{aligned}\hat{H}' \approx & \underbrace{\frac{\omega_q}{2}\hat{\sigma}_z + \omega_c\hat{a}^\dagger\hat{a} + g(\hat{a}+\hat{a}^\dagger)\hat{\sigma}_x}_{\hat{H}_{\mathrm{QRM}}} + \underbrace{\sum_i \Omega_d^{(i)}\hat{\sigma}_x\cos(\omega_d^{(i)}t)}_{\hat{H}_{\mathrm{drive}}} \underbrace{-\omega_q(\beta^*\hat{\sigma}_+ + \beta\hat{\sigma}_-) - i(\dot{\beta}\hat{\sigma}_- - \dot{\beta}^*\hat{\sigma}_+)}_{\hat{H}_1} \\ & \underbrace{+\sum_i \Omega_d^{(i)}\cos(\omega_d^{(i)}t)(\beta^*+\beta)\hat{\sigma}_z - \omega_q|\beta|^2\hat{\sigma}_z - i\frac{1}{2}(\beta^*\dot{\beta} - \beta\dot{\beta}^*)\hat{\sigma}_z}_{\hat{H}_z} \\ & \underbrace{-g(|\beta|^2+\beta^*)\hat{a}^\dagger\hat{\sigma}_+ - g(|\beta|^2+\beta)\hat{a}\hat{\sigma}_- - g(|\beta|^2+\beta^*)\hat{a}\hat{\sigma}_+ - g(|\beta|^2+\beta)\hat{a}^\dagger\hat{\sigma}_-}_{\hat{H}_{sb}} \\ & \underbrace{+g(\beta^*+\beta)(\hat{a}+\hat{a}^\dagger)\hat{\sigma}_z - \sum_i \Omega_d^{(i)}\cos(\omega_d^{(i)}t)\beta^*(\beta^*+\beta)\hat{\sigma}_+ - \sum_i \Omega_d^{(i)}\cos(\omega_d^{(i)}t)\beta(\beta^*+\beta)\hat{\sigma}_-}_{\hat{H}_2}.\end{aligned} \tag{4.5}$$

The main purpose of the transformation $\hat{U}$ is to eliminate the $\hat{H}_{\mathrm{drive}}$, the largest off-diagonal element in $\hat{H}'$ [26]. We need to chose proper β such $\hat{H}_{\mathrm{drive}} + \hat{H}_1 = 0$. $\hat{H}_z$ accounts for the qubit's frequency shifts and modulations. $\hat{H}_{sb}$ is related with the sideband transitions. $\hat{H}_2$ is irrelevant in the discussions here.

4.2.2. MONOCHROMATIC DRIVE

In this case, we have a drive Hamiltonian $\hat{H}_{\mathrm{drive}} = 2\epsilon_d\cos(\omega_d t)\hat{\sigma}_x$. For this, the proper β is given by,

$$\beta = \frac{\epsilon_d}{\Delta}e^{i\omega_d t} + \frac{\epsilon_d}{\Sigma}e^{-i\omega_d t}. \tag{4.6}$$

Here, Δ and Σ are $\omega_q - \omega_d$ and $\omega_q + \omega_d$ respectively. This β satisfies $\hat{H}_{\mathrm{drive}} + \hat{H}_1 = 0$. We obtain,

$$\hat{H}_z = \hat{\sigma}_z \times \left[(\frac{\epsilon_d^2}{\Delta} + \frac{\epsilon_d^2}{\Sigma})(1 + 2\cos(2\omega_d t)) - \frac{2\omega_q\epsilon_d^2}{\Delta\Sigma}\cos(2\omega_d t) \right], \tag{4.7}$$

which explains the qubit frequency shifts $\delta\omega_q$ and modulation with an amplitude $\Omega_m = 2\epsilon_m$ as given below.

$$\begin{aligned}\delta\omega_q &\approx 2\frac{\epsilon_d^2}{\Delta} + 2\frac{\epsilon_d^2}{\Sigma}, \\ \epsilon_m &\approx 2\frac{\epsilon_d^2}{\Delta} + 2\frac{\epsilon_d^2}{\Sigma} - 2\frac{2\omega_q\epsilon_d^2}{\Delta\Sigma}.\end{aligned} \tag{4.8}$$

The matching frequency can be found considering $\delta\omega_q$ and the lamb shift $\pm\chi$ in the qubit and cavity induced by bare coupling g. We can approximate χ by $g^2/\Delta_{qc} + g^2/\Sigma_{qc}$, where $\Delta_{qc} = \omega_q - \omega_c$ and $\Sigma_{qc} = \omega_q + \omega_c$. The conditions are given by,

$$\begin{aligned} 2\omega_d &= \omega_q + \delta\omega_q + \omega_c + 2\chi \ \text{(blue sideband)}, \\ 2\omega_d &= |\omega_q + \delta\omega_q - \omega_c + 2\chi| \ \text{(red sideband)}. \end{aligned} \tag{4.9}$$

When ω_d satisfies each blue and red sideband conditions, then the $\hat{H}_{sb}$ at the qubit and cavity rotating frame is reduced to,

$$\begin{aligned} &\hat{H}_{sb} = \\ &-g\left(\frac{\epsilon_d^2}{\Delta^2} + \frac{2\epsilon_d^2}{\Delta\Sigma}\right)\hat{a}^\dagger\hat{\sigma}_+ + \text{h.c.} \ \text{(blue sideband)}. \\ &-g\left(\frac{\epsilon_d^2}{\Delta^2} + \frac{2\epsilon_d^2}{\Delta\Sigma}\right)\hat{a}^\dagger\hat{\sigma}_- + \text{h.c.} \ \text{(red sideband)}, \omega_q > \omega_c. \\ &-g\left(\frac{\epsilon_d^2}{\Sigma^2} + \frac{2\epsilon_d^2}{\Delta\Sigma}\right)\hat{a}^\dagger\hat{\sigma}_- + \text{h.c.} \ \text{(red sideband)}, \omega_q < \omega_c. \end{aligned} \tag{4.10}$$

We define $\Omega_{sb}^{(0)}$ the transition rates obtained from Eq. 4.10. In addition to $\Omega_{sb}^{(0)}$, there is additional contribution from the qubit frequency modulation ϵ_m [37]. We define this contribution $\Omega_{sb}^{(1)}$, which amounts to $2gJ_1(2\epsilon_m/\Delta_{qc})$, where $J_n(x)$ is the first kind of Bessel function of order of n.

4.2.3. BI-CHROMATIC DRIVE

Now, we consider the drive Hamiltonian given by $\hat{H}_{\text{drive}} = 2\epsilon_{dq}\cos(\omega_{dq}t)\hat{\sigma}_x + 2\epsilon_{dc}\cos(\omega_{dc}t)\hat{\sigma}_x$. The subscription dq and dc refer to qubit friendly and cavity friendly drives as depicted in Fig. 4.1. In this case, we chose β as below,

$$\beta = \frac{\epsilon_{dq}}{\Delta_1}e^{i\omega_{dq}t} + \frac{\epsilon_{dq}}{\Sigma_1}e^{-i\omega_{dq}t} + \frac{\epsilon_{dc}}{\Delta_2}e^{-i\omega_{dc}t} + \frac{\epsilon_{dc}}{\Sigma_2}e^{i\omega_{dc}t}. \tag{4.11}$$

Here, $\Delta, \Sigma_1 = \omega_q \pm \omega_{dq}$ and $\Delta, \Sigma_2 = \omega_q \pm \omega_{dc}$. The drive induces the frequency shifts δ_q as given in Eq. 4.8. It also modulations the qubit frequency with angular speeds of $\omega_{dq} - \omega_{dc}$ and $\omega_{dq} + \omega_{dc}$. The amplitude of the modulations is also given in Eq. 4.8.

$$\begin{aligned} \delta\omega_q &\approx 2\frac{\epsilon_{dq}^2}{\Delta_1} + 2\frac{\epsilon_{dq}^2}{\Sigma_1} + 2\frac{\epsilon_{dc}^2}{\Delta_2} + 2\frac{\epsilon_{dc}^2}{\Sigma_2}, \\ \epsilon_m &\approx \epsilon_{dq}\epsilon_{dc}\left[\frac{1}{\Delta_1} + \frac{1}{\Delta_2} + \frac{1}{\Sigma_1} + \frac{1}{\Sigma_2}\right]. \end{aligned} \tag{4.12}$$

Then, the matching conditions are given by,

$$\begin{aligned} \omega_{dq} + \omega_{dc} &= \omega_q + \delta\omega_q + \omega_c + 2\chi \ \text{(blue sideband)}, \\ |\omega_{dq} - \omega_{dc}| &= |\omega_q + \delta\omega_q - \omega_c + 2\chi| \ \text{(red sideband)}. \end{aligned} \tag{4.13}$$

As in Sec. 6.2.2, we reduce $\hat{H}_{sb}$ like below when the above frequency matching condition satisfy.

$$\begin{aligned}
&\hat{H}_{sb} = \\
&-g\left(\frac{2\epsilon_{dq}\epsilon_{dc}}{\Delta_1\Delta_2}+\frac{\epsilon_{dq}\epsilon_{dc}}{\Delta_1\Sigma_2}+\frac{\epsilon_{dq}\epsilon_{dc}}{\Delta_2\Sigma_1}\right)\hat{a}^\dagger\hat{\sigma}_+ + \text{h.c.} \\
&\quad \text{(blue sideband)}. \\
&-g\left(\frac{\epsilon_{dq}\epsilon_{dc}}{\Delta_1\Delta_2}+\frac{\epsilon_{dq}\epsilon_{dc}}{\Delta_2\Sigma_1}+\frac{\epsilon_{dq}\epsilon_{dc}}{\Sigma_1\Sigma_2}\right)\hat{a}^\dagger\hat{\sigma}_- + \text{h.c.} \\
&\quad \text{(red sideband)}, \omega_q > \omega_c). \\
&-g\left(\frac{\epsilon_{dq}\epsilon_{dc}}{\Delta_1\Delta_2}+\frac{\epsilon_{dq}\epsilon_{dc}}{\Delta_1\Sigma_2}+\frac{\epsilon_{dq}\epsilon_{dc}}{\Sigma_1\Sigma_2}\right)\hat{a}^\dagger\hat{\sigma}_- + \text{h.c.} \\
&\quad \text{(red sideband)}, \omega_q < \omega_c).
\end{aligned} \tag{4.14}$$

We also take the effect from ϵ_m as in Sec. 6.2.2. $\Omega_{sb}^{(1)}$ in this case takes the same expression as in the monochromatic drive case, that is, $\Omega_{sb}^{(1)} = 2gJ_1(2\epsilon_m/\Delta_{qc})$.

4.2.4. ROTATING WAVE APPROXIMATION

Under the rotating wave approximation (RWA), $\hat{H}_{\text{drive}}$ is approximated to,

$$\hat{H}_{\text{drive}}^{(\text{RWA})} \approx \sum_i \frac{\Omega_d^{(i)}}{2}(\hat{\sigma}_+ e^{-i\omega_d^{(i)}t} + \hat{\sigma}_- e^{i\omega_d^{(i)}t}). \tag{4.15}$$

This amounts to taking $\Sigma \to \infty$ in $\Omega_{sb}^{(0,1)}$ and other quantities. The RWA converges to the full model results when $\Sigma \gg \Delta$. However, this condition often breakdowns with typical circuit QED device parameters. In Sec. 4.4, we perform the analytical calculation both based on the full and RWA model. The more detailed discussions will be provided there.

4.3. METHOD FOR NUMERICAL SIMULATION

The dynamics of the system can be described by the equation,

$$d\hat{\rho}_{sys}/dt = -i[\hat{H}_{\text{QRM}} + \hat{H}_{\text{drive}}, \hat{\rho}_{sys}]. \tag{4.16}$$

Here, $\hat{\rho}_{sys}$ is a density matrix of the qubit and cavity. We do not take the dissipation into consideration. In the numerical study in this work, we rigorously benchmark the real experiments. We set the rising and falling in the sideband drive strength as in the real experiments. Specifically, $\epsilon_d(t)$ is defined as a pulse with 10-ns of Gaussian rising and falling time. Then we scan the pulse length and plot the quantum states of the system at the end of each pulses. We do not include the rising and falling times in the definition of the pulse length.

Fig. 4.2 provides a step-by-step description of our numerical simulation method. The simulation parameters used in Fig. 4.2 are $\omega_q, \omega_c, \omega_d, \epsilon_d, g = 2\pi \times (6.5, 4.0, 0.1, 0.2, 5.278)$ GHz. The monochromatic drive frequency ω_d satisfies the matching condition for the

blue sideband transition. Fig. 4.2a show the dynamics of the system under the sideband drive pulse with a length of 480 ns. Fig. 4.2b magnifies the area enclosed by the square in Fig. 4.2a. One can identify the fast but small oscillation in the quantum state of the system. This oscillation originates from the Hamiltonian's time dependence. We can remove the time dependence by moving to the rotating frame at ω_d, and removing all the fast rotating components. This is what amounts to the rotating wave approximation (RWA). However, the RWA is only available when the ϵ_d and $|\omega_q - \omega_d|$ are small enough. For the two-photon sideband transition with circuit QED parameters, these conditions hardly satisfy. To tackle this oscillation, which allegedly does not exist in the real experiments, we repeat the simulations varying the pulse lengths, and plot the states at the end of the pulses (when the pulse falling finishes). The result is given in Fig. 4.2c. We obtain a clear sinusoidal curve.

The procedure described above is analogous with the real experiment. This explains why one still can see clear sinusoidal dynamics in the experiment even with very strong drive strength. We calculate $P(e1) - P(g0)$ for the blue sideband traitions, and $P(e0) - P(g1)$ for the red sideband transitions in this work. Here, P refers to the probability to find the system in that states. Once we obtain sinusoidal oscillation, then we determine the sideband transition rate Ω_{sb} from the period of the oscillation.

For monochromatic drive cases, we sweep the ω_d until the resonant sideband transition takes place to find the matching frequencies. The procedure is somewhat complicated for bi-chromatic drive cases. First we fix $\omega_{dc}/2\pi$ by $\omega_c/2\pi - 500$ MHz. We parameterize the $\epsilon_{dq}/2\pi$ and $\epsilon_{dc}/2\pi$ with a real positive parameter η. Both are given by $\epsilon_{dq}/2\pi = \eta \cdot 25$ MHz and $\epsilon_{dc}/2\pi = \eta \cdot 317$ MHz respectively. With these conditions, we sweep the ω_{dq} until the resonant sideband transition takes place. One result is given in Fig. 4.3. All the simulation parameters are the same in Fig. 4.2 except that $\epsilon_d/2\pi$ is 500 MHz. The matching frequency for blue sideband transition is found at $\omega_d/2\pi = 5.474$ GHz in this case. The asymmetric shape is attributed to the fact that the frequency shift of qubit changes while sweeping the drive frequency.

4.4. RESULTS AND DISCUSSIONS

4.4.1. OVERALL

In this section, we perform the numerical simulation with several system parameter sets. We define the drive frequency, transition frequencies of the qubit and cavity as $f_d = \omega_d/2\pi$, $f_q = \omega_q/2\pi$, and $f_c = \omega_c/2\pi$ respectively. We investigate the cases of $f_{q,c} = 6.5, 4.0$ GHz and $f_{q,c} = 4.0, 6.5$ GHz in this work. In Fig. 4.4, we present the simulated time domain dynamics when the two-photon sideband transitions take place. $g/2\pi$ in both cases is fixed by 200 MHz. Fig. 4.4-a shows the results under a monochromatic drive with $\epsilon_d/2\pi = 300$ MHz. Fig. 4.4-b shows the results under a bi-chromatic drive with $\epsilon_{dq}/2\pi = 25$ MHz and $\epsilon_{dc}/2\pi = 317$ MHz respectively. The definitions of ϵ_d, ϵ_{dq}, and ϵ_{dc} are the same as in the previous section. We can also confirm that whether the qubit is red or blue detuned to the cavity results in a difference in sideband transition rates. This is already predictable from Sec. 4.2.

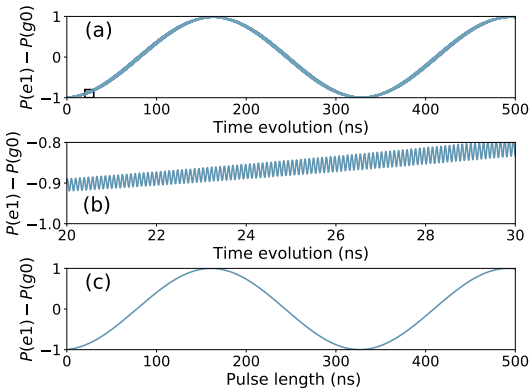

Figure 4.2: Time-domain numerical simulation. (a) A direct solution of the master equation when the drive field satisfies the blue sideband transition. Please see the text for the detail conditions in the simulation. We consider 10 ns Gaussian rising and falling time in the drive amplitude. (b) Zoom in on the black rectangular box in (a). We identify the fast micro-oscillation and the frequency of this oscillation is the same as the drive frequency. (c) We plot the $P(e1) - P(g0)$ at the end of the pulse with respect to the pulse length without rising and falling times. A clear sinusoidal oscillation is obtained.

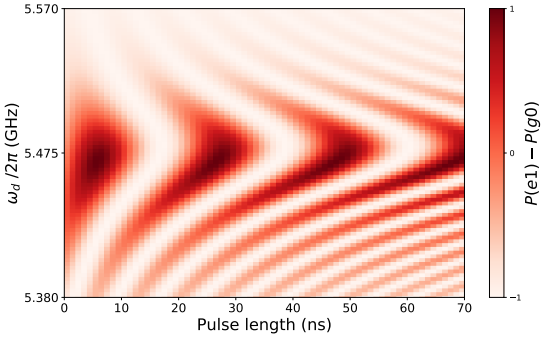

Figure 4.3: Finding a matching frequency. The plot shows the dynamics of the two-state system (qubit) when we sweep the monochromatic drive frequency around the matching frequency that satisfies the resonant blue sideband transition. Please see the text for the detailed conditions in the simulation.

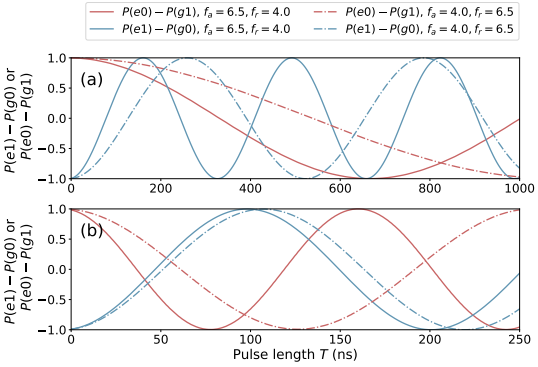

Figure 4.4: The first order two-photon sideband transitions in the QRM with various system configuations. 8 different cases are present. The red and blue lines indicate the red and blue sideband transitions respectively. (a) The sideband transitions by the monochromatic drive fields. (b) The sideband transitions by bi-chromatic drive fields. Please see the text and legend for detail conditions in the numerical simulation.

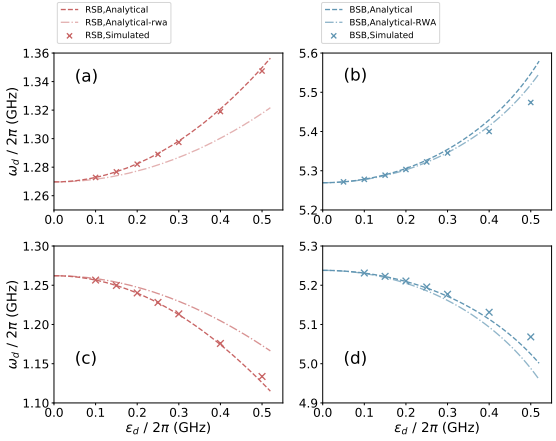

Figure 4.5: Matching frequencies (ω_d) for two-photon red and blue sideband transitions induced by monochromatic drive fields (ω_d). The single and double dashed lines indicate the analytically calculated matching frequencies the red and blue sideband transitions respectively. These are based on the full (single-dashed) and RWA model (double-dashed). The cross marks indicate the numerically simulated results based on the full model. (a,b) f_q = 6.5 GHz and f_c = 4.0 GHz. (c,d) f_q = 4.0 GHz and f_c = 6.5 GHz.

4.4.2. MONOCHROMATIC DRIVES

We deal with only the monochromatic drive cases in this subsection. All the system parameters $f_{d,a,r}$ are the same in Sec. 4.4.1. The lines in Fig. 4.5 shows the predicted matching frequencies analytically calculated. Single, and double-dashed lines indicate the results based on the full and RWA drive Hamiltonians respectively. We divided the cases into four different ones (see caption). Except the case in Fig. 4.5b, the full analytical model explains the numerical simulation results (cross). In the meantime, the lines in Fig. 4.6 shows the the predicted sideband tranition rates based on Eq. 4.10. Single, and double-dashed lines indicate the result based on the full and RWA drive Hamiltonians respectively. We first obtained the matching frequencies based on Eq. 4.9, and plug the values in Eq. 4.10 to calculate the sideband transition rates. In Fig. 4.6a-b, the red sideband transition rates predicted by the full model excellently agree with the numerical simulation, whereas the RWA model fails to explain the simulation. The full model provides more precise prediction in Fig. 4.6d either. As in matching frequency predictions, the case of Fig. 4.6b shows an exceptional trend.

The discrepancy between the simulation and analytical predicition in the blue sideband cases is larger than that of the red sideband cases. This is because the matching drive frequency f_d is much closer to the f_q in the blue sideband case, and consequently the validity condition ($\epsilon_d/|\omega_q - \omega_c| \ll 1$) for perturbative approach used in Sec. 4.2 becomes weakened.

We need to contemplate the results in Fig. 4.5b and Fig. 4.5d further. In these cases, the full analytical model is still more accurate than the RWA model in the low ϵ_d regime. A magnified view around $\epsilon_d/2\pi$= 100 MHz is present in Fig. 4.7. As ϵ_d becomes larger, the analytical calculation based on the full model deviates from the numerical simulation data faster than that of the RWA model. The deviation itself is reasonable since the our perturbative approach in Sec. 4.2 should breakdown as the drive strength increases. Since the predicted Ω_{sb} from the full model is larger than that of the RWA model, the deviation from the simulation is also faster for the full model. From these consideration, we conclude the better consistency between the simulation and the RWA model is a coincidence.

4.4.3. BI-CHROMATIC DRIVES

We investigate the bi-chromatic drive cases in this subsection. All the system parameters $f_{d,q,c}$ are the same in Sec. 4.4.1. We define the qubit and cavity friendly drive frequencies as f_{dq} and f_{dc} respectively. We analytically find the proper f_{dq} based on the Eq. 4.11 and Eq. 4.12, fixing the f_{dc}. ϵ_{dq} and ϵ_{dc} are parameterized as described in Sec. 4.3. We also analytically calculate the sideband transitions based on Eq. 4.13.

In Fig. 4.8, we compare the matching frequencies obtained from the simulation (cross) and analytical theories (line). The theory based on the full model gives more consistent results with the simulation in general although the RWA model also shows almost equal consistency in the case of Fig. 4.8a-b at large drive strengths. This can be attributed by the same reason we discussed for Fig. 4.5b. Fig. 4.9 compares the sideband transition rates calculated by the numerical simulation (cross) and analytical theories (line). The errors between the numerical simulations and analytical calculations at the large drive strengths are noticeably larger than those of monochromatic drive cases. This indicates

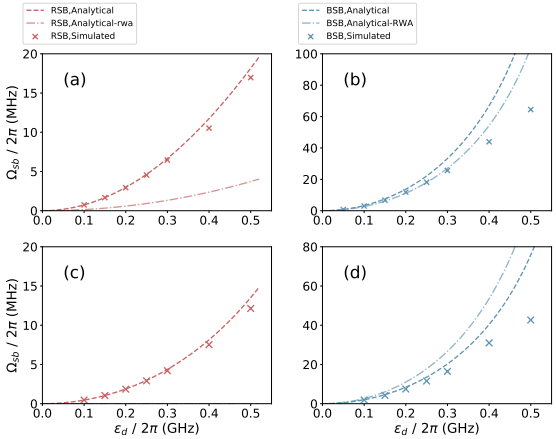

Figure 4.6: Red and blue sideband transition rates (Ω_{sb}) induced by monochromatic drive fields. The single and double dashed lines indicate the analytically calculated sideband transition rates on the full and RWA model respectively. The cross marks indicate the numerically simulated results based on the full model. (a,b) f_q = 6.5 GHz and f_c = 4.0 GHz. (c,d) f_q = 4.0 GHz and f_c = 6.5 GHz. In the case of (c), the predicted Ω_{sb} based on the RWA model is zero.

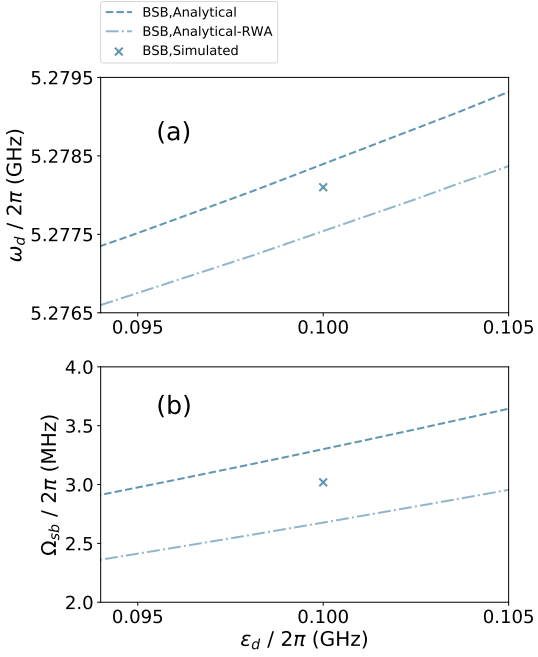

Figure 4.7: Magnified views of Fig. 4.5(b) and 4.6(b) near $\epsilon_d/2\pi$ = 100 MHz.

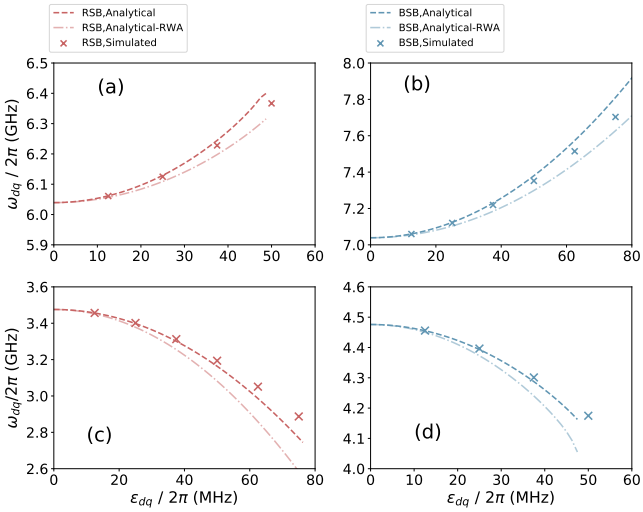

Figure 4.8: Matching frequencies (ω_{dq}) for two-photon red and blue sideband transition induced by bichromatic drive fields when ω_{dc} is fixed by ω_c-2$\pi\times$ 500MHz. ϵ_{dq} and ϵ_{dc} are parameterized as described in Sec. 4.3. The single and double dashed lines indicate the analytically calculated matching frequencies the red and blue sideband transitions respectively. These are based on the full (single-dashed) and RWA model (double-dashed). The cross marks indicate the numerically simulated results based on the full model. (a,b) f_q = 6.5 GHz and f_c = 4.0 GHz. (c,d) f_q = 4.0 GHz and f_c = 6.5 GHz.

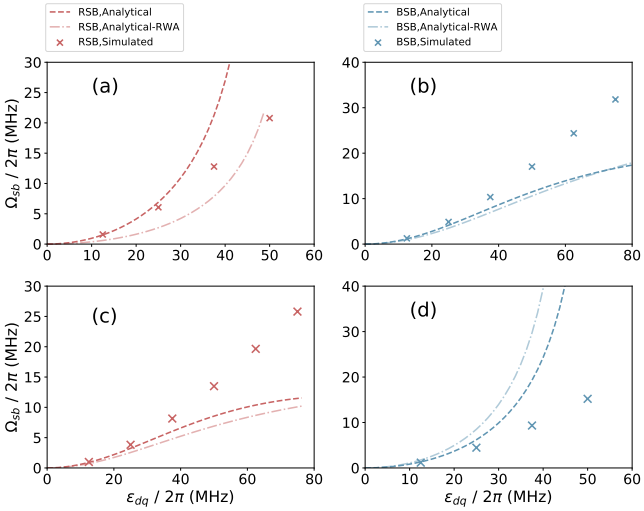

Figure 4.9: Red and blue sideband transition rates Ω_{sb} for various configurations induced by bi-chromatic drive fields. The single and double dashed lines indicate the analytically calculated sideband transition rates on the full and RWA model respectively. The cross marks indicate the numerically simulated results based on the full model. ω_{dc} is fixed by ω_c-2π× 500MHz. ϵ_{dq} and ϵ_{dc} are parameterized as described in Sec. 4.3 (a,b) f_q = 6.5 GHz, f_c = 4.0 GHz. (c,d) f_q=4.0 GHz, f_c = 6.5 GHz.

that the accuracy of the perturbative method in Sec. 4.2 becomes worse with more components of the drive Hamiltonian. Nonetheless, we can observe that the theory and simulation converge with small drive strength limit. This suggests that our analytical approach in Sec. 4.2 is correct as long as the approximation conditions $\epsilon_{dc,dq}/|\omega_q - \omega_c| \ll 1$ nicely hold.

4.4.4. ULTRASTRONG COUPLING REGIME

So far, we have fixed $g/2\pi$ by 200 MHz. In this subsection, we perform the simulation with different g while fixing the drive strengths and the other system parameters. We use f_q = 4.0 GHz and f_c = 6.5 GHz in the simulation. We scan g from 100 MHz (strong coupling regime) to 500 MHz (ultrastrong coupling regime).

In Fig. 4.10, we plot the matching frequencies and transition rates for red (a,c) and blue (b,d) sideband transitions induced by monochromatic drives. $\epsilon_d/2\pi$ used to induce the red and blue sideband transitions are 100 MHz and 300 MHz, respectively. The full analytical model explains the numerical simulation results better than the RWA model does. We can see the discrepancy between the full analytical model and numerical simulation in Fig. 4.10-d as g becomes larger whereas the full analytical model excellently explains the simulation results for all range of g in Fig. 4.10-c.

In Fig. 4.11, we plot the case of bi-chromatic drives. We also use f_q = 4.0 GHz and f_c = 6.5 GHz in the simulation. In these plots, we fix $\omega_{dc}/2\pi$ by $\omega_c/2\pi - 500$ MHz and paramterize ϵ_{dq} and ϵ_{dc} as in Sec. 4.4.3. The predicted matching frequencies are con-

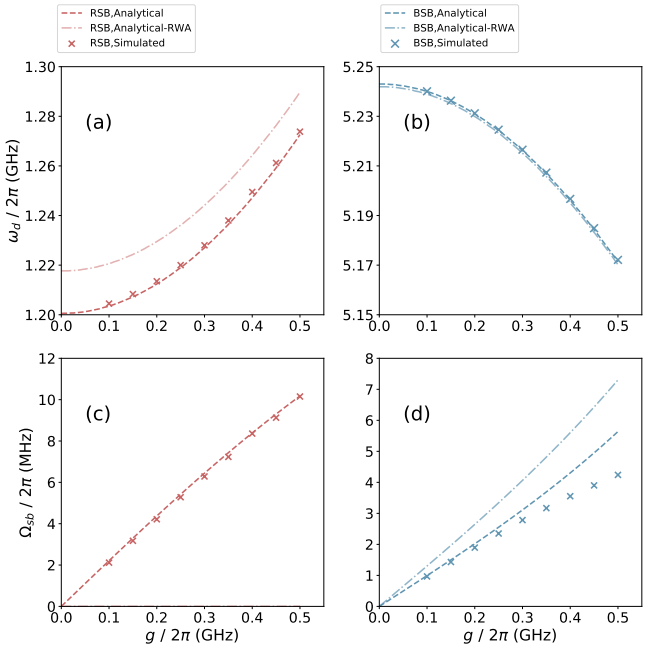

Figure 4.10: The matching frequencies ω_d (a,b) and sideband transition rates Ω_{sb} (c,d) while sweeping the qubit and cavity bare coupling g. Only monochromatic drive cases are present here. f_q = 4.0 GHz and f_c = 6.5 GHz in the simulation. (a,c) Red sideband transition with $\epsilon_d/2\pi$ = 100 MHz. (b,d) Blue sideband transition with $\epsilon_d/2\pi$ = 300 MHz. In the case of (c), the predicted Ω_{sb} based on the RWA model is zero.

sistent with the numerical simulation results. The sideband transition rates agrees well with the numerical simulation in the small g limit, and the full model always provides better predictions for Ω_{sb} than the RWA model does. We can see noticeable discrepancy between them with larger g in both red and blue sideband transitions.

4.5. CONCLUSION

In this work, we analytically and numerically study the first order sideband transitions induced by two-photon drives in quantum Rabi Hamiltonian. We confirm that both matching frequencies and sideband transition rates can be excellently predicted based on the analytical calculations when the parameters are in the perturbative regime, where $\epsilon/|\omega_q - \omega_d| \ll 1$ holds. We also confirm that the RWA significantly mislead the prediction on the matching frequencies and sideband transition rates except a few special cases.

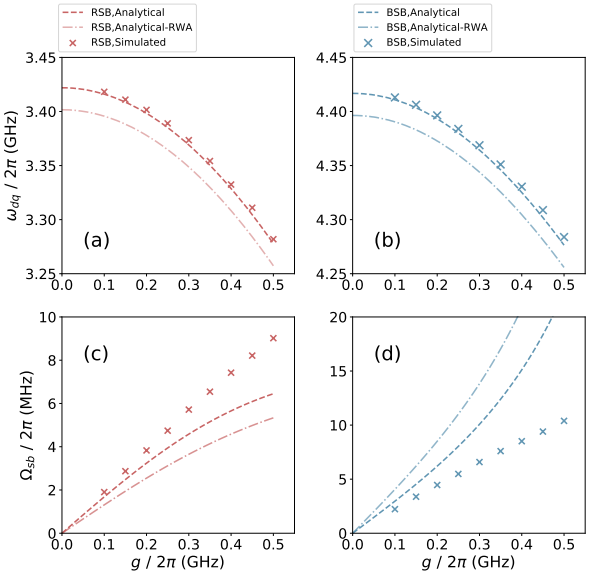

Figure 4.11: The matching frequencies (a,b) and sideband transition rates (c,d) while sweeping the qubit and cavity bare coupling g. (a,c) Red sideband transition. (b,d) Blue sideband transition. Only bi-chromatic drive cases are present here. $f_q = 4.0$ GHz and $f_c = 6.5$ GHz in the simulation. ω_{dc} is fixed by $\omega_c - 2\pi\times$ 500MHz. In all cases, we set $\epsilon_{dq}/2\pi = 25$ MHz and $\epsilon_{dc}/2\pi = 317$ MHz.

5

SIDEBAND TRANSITIONS IN A TWO-MODE JOSEPHSON CIRCUIT DRIVEN BEYOND THE ROTATING WAVE APPROXIMATION

Driving quantum systems periodically in time plays an essential role in the coherent control of quantum states. The rotating wave approximation (RWA) is a good approximation technique for weak and nearly resonance driving fields, experiments often require large detuning and strong driving fields, for which the RWA may not hold. In this work, we experimentally, numerically, and analytically explore strongly driven two-mode Josephson circuits in the regime of strong driving and large detuning. Specifically, we investigate beam-splitter and two-mode squeezing interaction between the two modes induced by driving two-photon sideband transition. Using numerical simulations, we observe that the RWA is unable to correctly capture the amplitude of the sideband transition rates, which we verify using an analytical model based on perturbative corrections. Interestingly, we find that the breakdown of the RWA in the regime studied does not lead to qualitatively different dynamics, but gives the same results as the RWA theory at higher drive strengths, enhancing the coupling rates compared to what one would predict. Our work provides insight into the behavior of time-periodically driven systems beyond the RWA, and provides a robust theoretical framework for including these in the calculation and calibration of quantum protocols in circuit quantum electrodynamics.

Parts of this chapter will be published in Physical Review Research.

5.1. INTRODUCTION

Time periodic driving is a prominent technique for the $in-situ$ coherent control of quantum dynamical processes. However, exactly solving the quantum dynamics of the system with time-varying Hamiltonian is particularly difficult [28, 31]. As long as the drive is weak enough and nearly resonant with the quantum state transition of a target observable, the rotating wave approximation (RWA) may provide a good estimate of the dynamics. However, understanding the physics of quantum systems beyond the RWA is required from both from a fundamental and a practical perspective. In the realm of faithful quantum information processing (QIP), the need for fast gates in order to suppress quantum errors requires drives strengths that could exceed those valid for the RWA. Motivated by this, theortical effort has been directed to understanding quantum driven systems beyond the RWA [28, 31], along with many experimental works under strong driving across many different physical systems. [54–61]. Existing studies exploring driven systems beyond the RWA, however, focus on a single driven mode and do not address the coupling of different degrees of freedom, such as the use of driving fields to induce sideband transitions between modes.

Sideband transitions ubiquitously appear in a variety of physical systems [26, 62–68]. Driving systems with appropriately chosen frequencies can yield engineered interactions among different degrees of freedoms. For engineering a specific interaction, it is important to accurately estimate the transition rates. In many cases such as trapped ions, cavity-optomechanics, and Raman transitions [65–68], the driving parameters for sideband transitions typically satisfy the requirements of the RWA. However, this is often not the case for the circuit quantum elecrodynamics (cQED) platform, one of the most promising QIP platforms in recent years, where a strong and far off resonant driving beyond the RWA is often required. Nonetehless, current approaches of such quantitative analysis still rely on the application of the RWA. When the sideband driving frequencies are far off-resonant from the transition frequencies of the system, in which the conditions for the application of the RWA should not hold, it is unclear if it is currently possible to make reliable predictions of the transition rates.

In this chapter, we study the sideband transition rates in a two-mode Josephson circuit induced by strong external time-periodical driving. The circuit comprises transmon [20] dispersively coupled to a resonator mode. Specifically, we study beam splitter (BS) and two-mode squeezing (TMS) interactions between each mode, which are the most fundamental forms of the sideband transitions in such two-mode systems. For our device, the required driving parameters are close to (TMS coupling), or far beyond (BS coupling) the RWA regime. We confirm a simple relation between the transition rates and frequency shifts that explains the data in both regimes at once.

We furthermore perform numerical simulations to support our findings, and derive an analytical perturbation expansion going beyond the RWA that is validated by our numerical results. Our findings indicate that although the RWA is clearly violated and significantly underestimates the mode frequency shifts and the sideband transition rates for a known driving strength, the breakdown of the RWA does not result in qualitatively different behaviour, but instead its effects in our measurements can be reproduced by the RWA theory using a larger drive field. Although the confirmation of breakdown of the RWA is therefore only possible through an independent calibration of the drive field,

our results show the importance of including counter-rotating terms for accurate calculations of the sideband transition rates.

5.2. THEORETICAL DESCRIPTION

We derive an analytical expression taking a similar approach in [26, 69] but breaking the RWA. The total Hamiltonian is given by,

$$\begin{aligned}\hat{H}^{(0)}_{sys} \approx\ & (\omega^{(0)}_t + \chi^{(0)}_t)\hat{\alpha}^\dagger\hat{\alpha} + \omega^{(0)}_r\hat{\beta}^\dagger\hat{\beta} + g(\hat{\alpha}+\hat{\alpha}^\dagger)(\hat{\beta}+\hat{\beta}^\dagger) \\ & + \chi^{(0)}_t(\hat{\alpha}+\hat{\alpha}^\dagger)^4/12.\end{aligned} \tag{5.1}$$

Here, $\omega^{(0)}_t$ and $\omega^{(0)}_r$ are the resonant frequencies of each mode. $\hat{\alpha}$ and $\hat{\beta}$ are the mode destruction operators of the transmon and the resonator modes, respectively. χ_t is a Duffing nonlinearity of the transmon mode. g is a transverse coupling between the transmon mode and the resonator mode. In addition to $\hat{H}^{(0)}_{sys}$, there is the driving Hamiltonian $\hat{H}^{(0)}_d = \Omega_d \cos\omega_d t(\hat{\alpha}+\hat{\alpha}^\dagger)$, where Ω_d and ω_d are the driving amplitude and frequency, respectively. Then the total Hamiltonian $\hat{H}^{(0)}_{tot}$ is give by $\hat{H}^{(0)}_{sys} + \hat{H}^{(0)}_d$.

It is often useful to rewrite above Hamiltonian in the normal mode basis (The normal mode annihilation operators are $\hat{a}$ and $\hat{b}$):

$$\begin{aligned}\hat{H}^{(1)}_{sys} \approx\ & (\omega^{(1)}_t + \chi_t)\hat{a}^\dagger\hat{a} + \omega^{(1)}_r\hat{b}^\dagger\hat{b} \\ & - \frac{1}{12}\left[\chi^{1/4}_t(\hat{a}+\hat{a}^\dagger) + \chi^{1/4}_r(\hat{b}+\hat{b}^\dagger)\right]^4.\end{aligned} \tag{5.2}$$

With typical circuit QED parameters, χ_t is approximately the same with $\chi^{(0)}_t$. χ_r is the inherited Duffing nonlinearity to the resonator mode by the coupling g. In the dispersive coupling regime ($|\omega_t - \omega_r| \gg g$), $\hat{\alpha}$ in $\hat{H}_d$ can be approximated by $\hat{a}$ [26, 70]. Then, the driving Hamiltonian can be approximated to $\hat{H}^{(1)}_d = \Omega_d \cos\omega_d t(\hat{a}+\hat{a}^\dagger)$.

The total Hamiltonian in the normal mode basis is then given by $\hat{H}^{(1)}_{tot} = \hat{H}^{(1)}_{sys} + \hat{H}^{(1)}_d$. This can be perturbatively diagonalized by taking Schrieffer–Wolff (S–W) transformation [53] $\hat{U}(t) = e^{\hat{S}}$ with an appropriate generator $\hat{S} = \xi(t)\hat{a}^\dagger(t) - \xi(t)^*\hat{a}$. When $\Delta \gg \chi_t$, we can choose $\xi(t) = \frac{\Omega_d}{2\Delta}e^{-i\omega_d t} + \frac{\Omega_d}{2\Sigma}e^{i\omega_d t}$. Here, $\Delta = \omega^{(1)}_t + \chi_t - \omega_d$ and $\Sigma = \omega^{(1)}_t + \chi_t + \omega_d$. In this work, we treat beam splitter ($\hat{a}\hat{b}^\dagger + \hat{a}^\dagger\hat{b}$) and two-mode squeezing ($\hat{a}\hat{b} + \hat{a}^\dagger\hat{b}^\dagger$) interactions induced by two-photon driving. These appear with frequency matching conditions $2\omega_d \approx |\omega^{(1)}_t \pm \omega^{(1)}_r|$.

After taking Schrieffer–Wolff transformation, collecting only the original and relevant derived terms yields,

$$\begin{aligned}\hat{H}^{(1)}_{tot} \approx\ & (\omega^{(1)}_t + \delta\omega^{(1)}_t + \chi_t)\hat{a}^\dagger\hat{a} + (\omega^{(1)}_r + \delta\omega^{(1)}_r)\hat{b}^\dagger\hat{b} \\ & - \frac{1}{12}\left[\chi^{1/4}_t(\hat{a}+\hat{a}^\dagger) + \chi^{1/4}_r(\hat{b}+\hat{b}^\dagger)\right]^4 + \hat{H}_{sb},\end{aligned} \tag{5.3}$$

where $\hat{H}_{sb} = \Omega^{(1)}_{sb}/2(\hat{a}\hat{b}^\dagger e^{i2\omega_d t} + \hat{a}^\dagger\hat{b}e^{-i2\omega_d t})$ when $2\omega_d \approx |\omega^{(1)}_t - \omega^{(1)}_r|$, and $\hat{H}_{sb} = \Omega^{(1)}_{sb}/2(\hat{a}\hat{b}e^{i2\omega_d t} + \hat{a}^\dagger b^\dagger e^{\hat{-i2\omega_d t}})$ when $2\omega_d \approx |\omega^{(1)}_t + \omega^{(1)}_r|$. Here, $\Omega^{(1)}_{sb}$ is the interaction rate for both the BS

and TMS interactions. $\delta\omega_{t,r}^{(1)}$ and $\Omega_{sb}^{(1)}$ can be expressed by,

$$\begin{aligned}\delta\omega_{t,r}^{(1)} &= \frac{1}{2}\Omega_d^2\chi_{t,tr}\times(\frac{1}{\Delta^2}+\frac{2}{\Delta\Sigma}+\frac{1}{\Sigma^2}),\\ \Omega_{sb}^{(1)} &= \frac{1}{2}\Omega_d^2\chi_t^{3/4}\chi_r^{1/4}\times(\frac{1}{\Delta^2}+\frac{2}{\Delta\Sigma}+\frac{1}{\Sigma^2}).\end{aligned} \tag{5.4}$$

In the low excitation limit, the total Hamiltonian can be reduced to,

$$\begin{aligned}\hat{H}_{tot}^{\textbf{low}} \approx\ &(\omega_t+\delta\omega_t)\hat{a}^\dagger\hat{a}+(\omega_r+\delta\omega_r)\hat{b}^\dagger\hat{b}-\frac{A_t}{2}\hat{a}^\dagger\hat{a}^\dagger\hat{a}\hat{a}\\ &-\frac{A_r}{2}\hat{b}^\dagger\hat{b}^\dagger\hat{b}\hat{b}-2A_{tr}\hat{a}^\dagger\hat{a}\hat{b}^\dagger\hat{b}+\hat{H}_{sb}.\end{aligned} \tag{5.5}$$

$\omega_{t,r}$ and $A_{t,r,tr}$ ($A_{tr}\approx\sqrt{A_tA_r}$) correspond to the transition frequencies and anharmonicities that we observe in the experiments. We can obtain $A_{t,r,tr}$ by numerically diagonalize Eq. B.1 [71]. The difference between A and χ is due to the off diagonal elements in Eq. 5.3. We empirically find that $\delta\omega_{t,r}^{(1)}$ and $\Omega_{sb}^{(1)}$ in Eq. 6.7 should be renormalized to $\delta\omega_{t,r}$ and Ω_{sb},

$$\begin{aligned}\delta\omega_{t,r} &= \frac{1}{2}\Omega_d^2A_{t,tr}\times(\frac{1}{\Delta^2}+\frac{2}{\Delta\Sigma}+\frac{1}{\Sigma^2}),\\ \Omega_{sb} &= \frac{1}{2}\Omega_d^2A_t^{3/4}A_r^{1/4}\times(\frac{1}{\Delta^2}+\frac{2}{\Delta\Sigma}+\frac{1}{\Sigma^2}).\end{aligned} \tag{5.6}$$

When applying the RWA, they are given by,

$$\begin{aligned}\delta\omega_{t,r}^{(\mathrm{RWA})} &= \frac{1}{2}\Omega_d^2A_{t,tr}\times\frac{1}{\Delta^2},\\ \Omega_{sb}^{(\mathrm{RWA})} &= \frac{1}{2}\Omega_d^2A_t^{3/4}A_r^{1/4}\times\frac{1}{\Delta^2}.\end{aligned} \tag{5.7}$$

It is also interesting to investigate the case where only the counter-rotating terms in $\hat{H}_d$ affects the system. In this case the frequency shifts and sideband transition rates are given by,

$$\begin{aligned}\delta\omega_{t,r}^{(\mathrm{CR})} &= \frac{1}{2}\Omega_d^2A_{t,tr}\times\frac{1}{\Sigma^2},\\ \Omega_{sb}^{(\mathrm{CR})} &= \frac{1}{2}\Omega_d^2A_t^{3/4}A_r^{1/4}\times\frac{1}{\Sigma^2}.\end{aligned} \tag{5.8}$$

The detailed derivation is provided in Appendix 5.6.1. When knowing $\delta\omega_t$, replacing Δ and Σ with $\Delta+\delta\omega_t$ and $\Sigma+\delta\omega_t$ provides more accurate estimates. It is worthy to point out that in many previous studies, the derivation stops at Eq. 6.2. However, the discrepancies between $A_{t,r,tr}$ and $\chi_{t,r,tr}$ are sometimes significant depending on the system parameters. Renormalization of $\delta\omega_{t,r}$ and Ω_{sb} is therefore of great importance for the accurate prediction of the quantities.

Eq. 5.6 and Eq. 5.7 suggests that the RWA significantly underestimates $\delta\omega_{t,r}$ and Ω_{sb} when $\Delta\sim\Sigma$ but the ratios among them are identical regardless of whether using the RWA or not. It is also interesting to note that there is correlation between the co- and counter-rotating terms that gives a significant contribution to the frequency shifts and sideband transition rates.

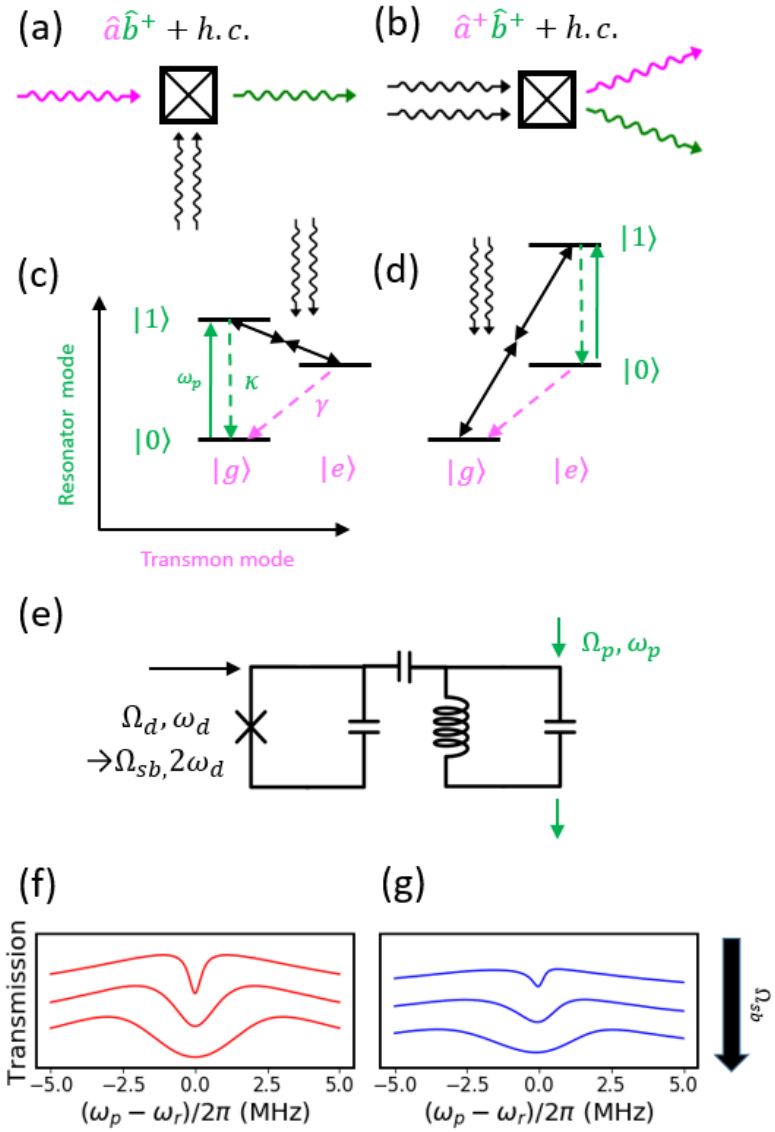

Figure 5.1: Overview of the experiment. (a,b) Schematics of the beam splitter (a) and two-mode squeezing (b) interactions. Black, magenta and green wavy arrows indicate driving, transmon mode and resonator mode photon respectively. (c,d) Energy level diagrams. Dashed arrows indicate decay of transmon and resonator. Solid green arrow represents probe tone through resonator. (e) Simplified circuit diagram of the device. (f,g) Electromagnetically induced transparency (EIT) spectrum of the resonator calculated by the numerical model in 5.5 when $\Omega_{sb}/2\pi$ is 2, 4 and 6 MHz respectively (from top to bottom). Red and blue curves correspond to the BS and the TMS interaction respectively. See main text for detail simulation conditions.

5.3. EXPERIMENT

Both the BS and the TMS interaction are schematically described in Fig. 5.1a and Fig. 5.1b. Two black wavy arrows indicate the two-photon drive. Fig. 5.1c and Fig. 5.1d denote energy diagram descriptions. In all descriptions, the resonator and the transmon mode are colored by green and magenta respectively. In addition to the two-photon drive, we have a weak probe field (green) through the resonator mode to estimate Ω_{sb} through the resonator response. The decay rate of both modes are κ and γ, respectively. The energy levels of the resonator mode are denoted by $|0\rangle$, $|1\rangle$, $|2\rangle$,... and those of the transmon mode are denoted by $|g\rangle$, $|e\rangle$,...

Fig. 5.1e depicts a simplified circuit diagram of the system. We drive the transmon mode through a direct driveline and probe the resonator mode through another feedline coupled to the resonator. Fig. 5.1f and Fig. 5.1g show how the probe transmission through the resonator varies with increasing Ω_{sb} for both BS (f) and TMS (g) interaction. The curves are obtained by solving a numerical model based on Eq. 5.5 with dissipation operators. The decay rates of the resonator and transmon modes in the calculation are $\kappa/2\pi \approx 10.2$ MHz and $\gamma/2\pi \approx 129$ kHz. These parameters are similar to those in the experiment. $\Omega_{sb}/2\pi$ is set by 2,4, and 6 MHz in both BS and TMS interaction. The detailed information on the experimental setup and device is provided in Appendix 5.8.1.

In the experiment, we deliberately design a large κ to facilitate the detection of the interactions through the resonator transmission even with small Ω_{sb}. As long as Ω_{sb} is smaller than $|\gamma - \kappa|$, our system satisfies the condition for electromagnetically induced transparency (EIT) [72]. In this regime, Ω_{sb} and the other parameters independently feature the transparency window in the middle of the transmission spectrum of the resonator. Thereby, we extract Ω_{sb} by fitting the resonator transmission. The resonator linewidth is overwhelmingly larger than the linewitdth of the qubit and therefore the system is in the EIT condition as long as Ω_{sb} is less than around 10 MHz.

The observed $\omega_{t,r}$ are $2\pi\times$ 6.8112 and 4.0755 GHz respectively. The observed A_t is $2\pi \times 150$ MHz and A_r can be deduced by $A_{tr} \approx \sqrt{A_t A_r}$. Since the resonator has a broad linewidth, we cannot simply extract A_{tr} from photon number splitting of the resonator or the transmon spectrum. We obtained $A_{tr}/2\pi \approx 497$ kHz from another calibration method in Appendix 5.8.2. From these observations, we can calculate the system parameters in Eq. 5.1 and Eq. B.1.

In Fig. 5.2, we present the procedure used for determining the frequency matching conditions for both the BS and the TMS interactions. If we do not take into account that the driving field shifts the resonance frequencies of the modes, the matching frequencies ω_{mat} satisfies $2\omega_{mat} = |\omega_t \pm \omega_r|$. In reality the resonances undergo shifts, $\omega_{t,r} \rightarrow \omega'_{t,r} = \omega_{t,r} + \delta\omega_{t,r}$ and in our system we have $\delta\omega_t \gg \delta\omega_r \approx 0$. Thus, we need a careful adjustment of ω_d around the expected frequency matching conditions. We define $2\omega'_{mat} = |\omega'_t \pm \omega_r|$ as driving frequencies satisfying the matching condition considering $\delta\omega_{t,r}$. We swept the driving frequency and find the condition $\omega_d \approx \omega'_{mat}$. We obtain the matching conditions when the transparency window is located at the center in the transmission spectrum. Also, from ω'_{mat}, we can extract $\delta\omega_t$. Roughly, $\omega_{mat}/2\pi \approx$ 1.36 and 5.44 GHz are expected for both the BS and the TMS interaction, respectively. For the BS interaction, ω'_{mat} is extremely far off-resonant ($\Delta/\Sigma \approx 0.6$). This regime of the driving parameter has not been explored. On the other hand, for TMS interaction, ω'_{mat}

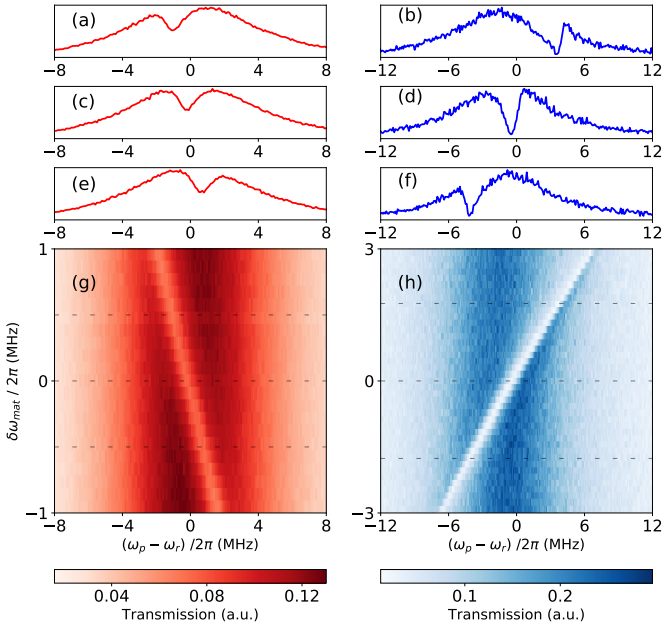

Figure 5.2: Spectroscopic observation of sideband transitions. (g) Drive frequency sweep around the matching condition for beam splitter (BS) interaction. (h) The same for two-mode squeezing (TMS) interaction. $\delta\omega_{mat}$ is the deviation of the driving frequencies from the matching conditions ($\omega_d - \omega'_{mat}$). (a-f) The cross section of the dashed lines in (g) and (h) respectively.

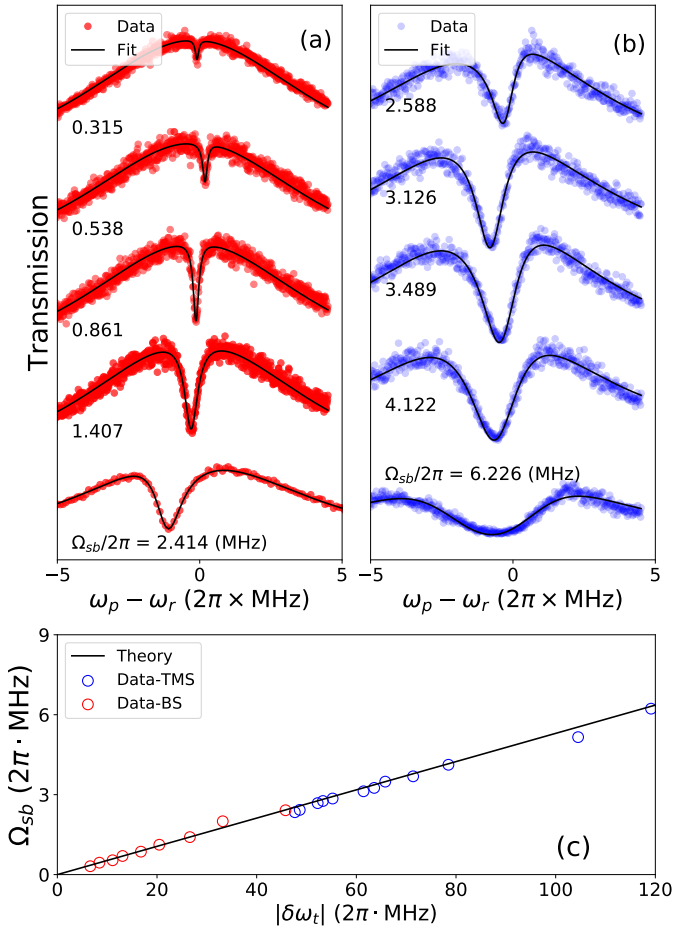

Figure 5.3: Driving power dependence of sideband transition rates. Left (red) : BS interaction. Right (blue) : TMS interaction. (a,b) Resonator transmission spectrum (circle) with increasing driving amplitude (top to bottom) while keeping $\omega'_{mat} \approx \omega_d$. Solid curves are fits to the data based on numerical model. From these fits we extracted Ω_{sb} and $\delta\omega_t$. The probe amplitude Ω_p is $2\pi\times130.6$ kHz except that Ω_p is ten times larger for the lowest data of (a). (c) Observed Ω_{sb} with respect to corresponding $\delta\omega_t$ (circles). Solid line indicates a theory based on Eq. 5.6. Fitting errors in Ω_{sb} are around 1% and not plotted in the figures.

is relatively closer to the RWA regime ($\Delta/\Sigma \approx 0.11$).

In Fig. 5.3 a–b, we plot a portion of the transmission spectrum observed in the experiment. We scan the sideband driving power preserving the condition $\omega_d \approx \omega'_{mat}$. The solid curves are the fits based on the numerical model that we used in Fig. 5.1f–g. In the fitting process, the free parameters are Ω_{sb}, γ and $\delta\omega_{mat}$, while the other parameters are fixed. As increasing the driving amplitudes, one can readily see the transparency windows behave as expected from Fig. 5.1f–g. In Fig. 5.3c, we plot Ω_{sb} with respect to the corresponding $\delta\omega_t$, both of which are extracted from the fitting. The statistical errors in extracting Ω_{sb} from the fitting are around only 1% and thus not presented in the figures. We can find a linear correlation between $\delta\omega_t$ and Ω_{sb}. The slope of the solid line is obtain from Eq. 5.6, with no free parameters. It is intriguing to point out that both BS and TMS data lie on the same theoretical plot, although the driving parameters for each lives in distinct regimes.

In order to directly identify the breakdown of the RWA, we need to calibrate Ω_d from an independent method not relying on the transmon frequency shifts. If we know the microwave power at the device (P_d), and the coupling rate between the transmon and drive line (γ_{ex}), then Ω_d is simply given by $\sqrt{P_d\gamma_{ex}}$. However, the uncertainty in the driveline attenuation set a challenge. Only 1 dB error in the attenuation induces a 10% error in Ω_d, which is critical to our study. In the future study, this challenge can be circumvented by using an additional 'sensor' qubit as recently demonstrated in [73].

5.4. NUMERICAL SIMULATION

We performed a comprehensive numerical analysis with the experimental conditions. We simulated the system's time domain dynamics by solving the $d\hat{\rho}_{sys}/dt = -i[\hat{H}^{(0)}_{sys} + \hat{H}^{(0)}_d, \hat{\rho}_{sys}]$ without including any dissipation. $\hat{\rho}_{sys}$ is the density matrix of the system. As in the experiment, we swept the driving frequency for a given Ω_d and find the frequency with which a full oscillation takes place in transitions $|e0\rangle \Longleftrightarrow |g1\rangle$ (BS) or $|g0\rangle \Longleftrightarrow |e1\rangle$ (TMS). Ω_{sb} is then given by the frequency of the oscillation. More detail descriptions on the method of the numerical simulation are given in Appendix 5.7.

In Fig. 5.4, we present the numerical calculation results (circles, triangles and squares) and corresponding analytical calculation results (solid, dashed and dotted line). The circles and solid lines refer to the results with the $\hat{H}^{(0)}_{sys} + \hat{H}^{(0)}_d$. In the plots, triangles and squares refer to the simulation results dropping the counter-rotating and co-rotating driving terms in $\hat{H}^{(0)}_d$. The analytical calculation is based on the Eq. 5.6. The dashed and dotted lines are obtained by Eq. 5.7 and Eq. 5.8 respectively.

In Fig. 5.4a–b, we compare sideband transition rates obtained by the numerical simulations (circles, triangles and squares) with the analytically calculated values (solid, dashed and dotted line). In Fig. 5.4 c–d, we present the frequency shifts of the transmon mode under the matching conditions for given the driving amplitudes in x-axes. The driving frequencies for each data points are set to satisfy the matching conditions for the given driving amplitudes. Although the RWA significantly distort the Ω_{sb} and $\delta\omega_t$, the breakdown of the RWA is not visible in the Ω_{sb} versus $\delta\omega_t$ relation as seen in Fig. 5.4 e-f. The simulation data with the RWA perfectly lie on the data without the RWA. Therefore, a careful treatment is required when estimating Ω_d through Ω_{sb} or $\delta\omega_t$. Relying on the

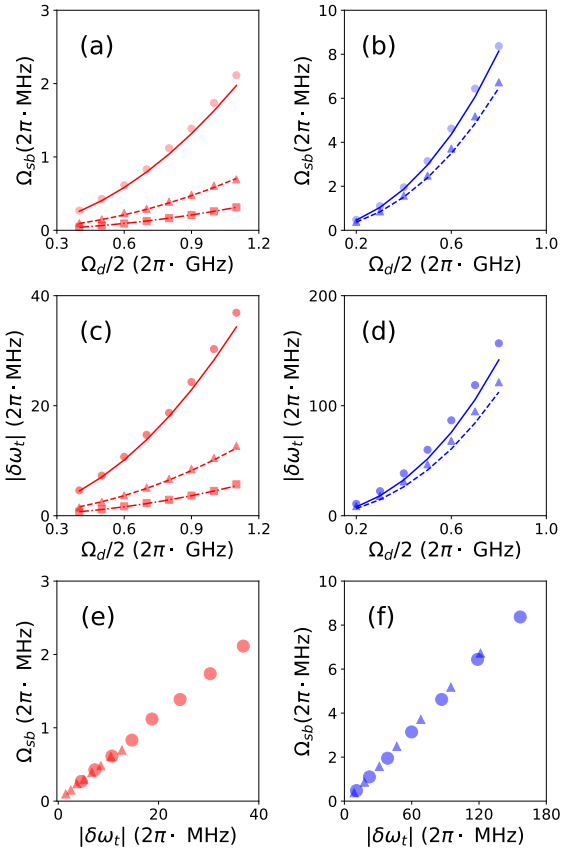

Figure 5.4: Influence of counter rotating terms of the driving on the sideband transition rates and the mode frequency shifts for BS (red, left) and TMS (blue, right) interactions. Symbols: numerical simulations with $\hat{H}^{(0)}_{tot}$ (circle), under the rotating wave approximation (RWA) keeping only co-rotating terms in $\hat{H}^{(0)}_{d}$ (triangle), and keeping only counter-rotating (CR) terms in $\hat{H}^{(0)}_{d}$ (squares). Lines: analytical theory for $\hat{H}^{(0)}_{d}$ (solid), the RWA in $\hat{H}^{(0)}_{d}$ (dashed), and only CR terms in $\hat{H}^{(0)}_{d}$ (dotted). Dynamics beyond the RWA is clearly observed for in the transition rates (a,b) and frequency shift (c,d) for both red and blue sideband driving. For the red sideband, even the purely counter-rotating terms lead to a non-zero coupling, although the deviation of the full result from the sum of the RWA and purley-CR calculations indicates additional contributions from correlations of the two. (e,f) Although discarding the CR terms leads to large correction of the Ω_{sb}, the relation between Ω_{sb} and $\delta\omega_t$ for the full $\hat{H}^{(0)}_{d}$ remains the same and fall on the same line (circles, triangles): the error that arises in discarding the CR terms is an incorrect value of both Ω_{sb} and $\delta\omega_t$ for a given known driving strength.

RWA results in significant overestimation of Ω_d.

5.5. CONCLUSION

To summarize, we performed the quantitative investigation of the two-photon assisted four-wave interactions in the superconducting circuit. Over the entire range of the driving amplitudes in this work, our theoretical, numerical and experimental values excellently agree with one another, suggesting that the faithful quantitative expectation of sideband transition rates is possible. This work expands our understanding in the strongly driven quantum systems. The findings through this work would not be restricted within the system we investigate here.

Kerr or Duffing type nonlinearity ubiquitously appears in many physics disciplines other than circuit QED such as nonlinear optics, cavity optomechanics, and atomic physics [74–77]. Therefore, we believe our findings can influence a variety of types of research. This work also uses multi-photon assisted transition, which is widely adopted when a desired transition is dipole forbidden [19, 49, 62, 63, 78–88]. In a perspective that the studies of multi-photon transition beyond the RWA are mainly limited to theoretical cases [89–91], our work would attract attention.

5.6. APPENDIX-THEORETICAL DESCRIPTIONS

5.6.1. DERIVATION OF SIDEBAND TRANSITION RATES

We perturbatively diagonalize the total Hamiltonian by applying the unitary transformation $\hat{U}(t)$ to the total Hamiltonian $\hat{H}^{(1)}_{tot} = \hat{H}^{(1)}_{sys} + \hat{H}^{(1)}_{d}$, where $\hat{H}^{(1)}_{sys}$ and $\hat{H}_d$ are defined in the main text. The transformed Hamiltonian $\hat{H'}_{tot}$ is given,

$$\hat{H'}^{(1)}_{tot} = \hat{U}\hat{H}\hat{U}^{\dagger} + i(\partial_t \hat{U})\hat{U}^{\dagger}. \tag{5.9}$$

Here, $\hat{U}(t) = e^{\xi(t)\hat{a}^{\dagger} - \xi(t)^{*}\hat{a}}$ and $\xi(t) = \frac{\Omega_d}{2\Delta}e^{-i\omega_d t} + \frac{\Omega_d}{2\Sigma}e^{i\omega_d t}$. $\hat{U}(t)$ simply displaces the field operator $\hat{a}(\hat{a}^{\dagger})$ by -ξ(-ξ^{*}). Finally, $\hat{H'}^{(1)}_{tot}$ can be expressed by,

$$\begin{aligned}\hat{H'}^{(1)}_{tot} \approx\ & (\omega_t^{(1)} + \chi_t)\hat{a}^{\dagger}\hat{a} + \omega_r^{(1)}\hat{b}^{\dagger}\hat{b} \\ & - \frac{1}{12}\left[\chi_t^{1/4}(\hat{a} + \hat{a}^{\dagger} - \xi(t) - \xi^{*}(t)) + \chi_r^{1/4}(\hat{b} + \hat{b}^{\dagger})\right]^4.\end{aligned} \tag{5.10}$$

For given ω_d, collecting the non-rotating terms at the transmon and resonator rotating frame in Eq. 5.10 yields Tab. 5.1. We only list the terms that represent the interactions between different modes or the frequency shifts of each mode.

5.6.2. MODELING TRANSMISSION SPECTRUM

The resonator transmission spectrum is proportional to $\mathrm{Tr}_t[\hat{\rho}_{ss}\hat{b}]$. Here, $\hat{\rho}_{ss}$ is a steady state density matrix of the transmon and resonator system, and Tr_t indicates trace over

Operator	Magnitude ($\times\Omega_d^2/4$)	Matching condition ($\omega_d \sim$)
$\hat{a}^\dagger\hat{a}$	$\chi_{t,r}$ $\times(2\frac{1}{\Delta^2}+\frac{2}{\Delta\Sigma}+\frac{1}{\Sigma^2})$	None
$\hat{b}^\dagger\hat{b}$	$\chi_{t,r}\times(2\frac{1}{\Delta^2}+\frac{2}{\Delta\Sigma}+\frac{1}{\Sigma^2})$	None
$\hat{a}\hat{b}^\dagger$	$\chi_t^{3/4}\chi_r^{1/4}\times(\frac{1}{\Delta^2}+\frac{2}{\Delta\Sigma}+\frac{1}{\Sigma^2})$	$\lvert\omega_t^{(1)}-\omega_r^{(1)}\rvert/2$
$\hat{a}^\dagger\hat{b}^\dagger$	$\chi_t^{3/4}\chi_r^{1/4}\times(\frac{1}{\Delta^2}+\frac{2}{\Delta\Sigma}+\frac{1}{\Sigma^2})$	$\omega_t^{(1)}+\omega_r^{(1)}/2$
$\hat{a}\hat{b}^{\dagger 2}$	$\chi_t^{1/4}\chi_r^{3/4}\times(\frac{1}{\Delta}+\frac{1}{\Sigma})$	$\lvert 2\omega_r^{(1)}-\omega_t^{(1)}\rvert$
$\hat{a}^\dagger\hat{b}^{\dagger 2}$	$\chi_t^{1/4}\chi_r^{3/4}\times(\frac{1}{\Delta}+\frac{1}{\Sigma})$	$2\omega_r^{(1)}+\omega_t^{(1)}$
$\hat{a}^2\hat{b}^\dagger$	$\chi_t^{3/4}\chi_r^{1/4}\times(\frac{1}{\Delta}+\frac{1}{\Sigma})$	$\lvert 2\omega_t^{(1)}-\omega_r^{(1)}\rvert$
$\hat{a}^{\dagger 2}\hat{b}^\dagger$	$\chi_t^{3/4}\chi_r^{1/4}\times(\frac{1}{\Delta}+\frac{1}{\Sigma})$	$2\omega_t^{(1)}+\omega_r^{(1)}$

Table 5.1: List of a portion of the non-rotating terms at the transmon and resonator rotating frame for given ω_d derived from the forth power term of Eq. 5.10.

5

the transmon states. $\hat{\rho}_{ss}$ can be calculated based on the below Eq. 5.11,

$$\frac{d\hat{\rho}}{dt} = -\frac{i}{\hbar}\left[\hat{H}_{\text{low}}+\hat{H}_p(t),\hat{\rho}(t)\right] + \frac{\gamma}{2}\mathscr{D}[\hat{a}]\hat{\rho}+\frac{\kappa}{2}\mathscr{D}[\hat{b}]\hat{\rho}. \tag{5.11}$$

$\hat{H}_p(t)=\Omega_p\cos(\omega_p t)$ is the Hamiltonian of the prove field. $\mathscr{D}[\hat{\mathscr{O}}]\hat{\rho}$ is defined by $2\hat{\mathscr{O}}\hat{\rho}\hat{\mathscr{O}}^\dagger - \hat{\mathscr{O}}^\dagger\hat{\mathscr{O}}\hat{\rho}-\hat{\rho}\hat{\mathscr{O}}^\dagger\hat{\mathscr{O}}$. κ is the decay rate of the resonator mode, and γ is that of the transmon mode. We neglect the pure dephasing rate of the transmon mode. Since we employ a single Josephson junction design, it is expected that the coherence time of the transmon mode is only limited to the decay time. For a steady state, we have $\frac{d\hat{\rho}_{ss}}{dt}=0$, then we can calculate $\hat{\rho}_{ss}$ from Eq. 5.11.

Transmission spectrum is a function of a set of variables (ω_d, ω_p, Ω_p, Ω_{sb}, ω_t', ω_r, A_t, A_r, A_{tr} κ, and γ). Here, ω_p is the independent variable in the fitting process. We fix κ, ω_r, A_t, A_r, and A_{tr} by the values we obtain from the independent measurement without driving field. These quantities are hardly shifted under the driving. ω_d is given by the experiment. The free fitting parameters are ω_t, Ω_{sb}, Ω_p, and γ. These quantities are extracted from the fitting process.

5.7. APPENDIX-NUMERICAL SIMULATIONS

In this section, we describe the detail procedures of the time-domain numerical simulations. The dynamics of the system is governed by the equation, $d\hat{\rho}_{sys}/dt=-i[\hat{H}_{sys}^{(0)}+\hat{H}_d^{(0)}(t),\hat{\rho}_{sys}]$, where $\hat{H}_{sys}^{(0)}$ and $\hat{H}_d^{(0)}$ follow the same definition in the main text. Here, $\hat{\rho}_{sys}$ is density matrix of the transmon and resonator. We do not take the dissipation into consideration in the time-domain dynamic simulations. Fig. 5.5a shows the simulated dynamics (blue line) when the driving frequency satisfies the matching condition for two-mode squeezing (TMS) interaction. The system parameters used in the simulation are the same with the experimental conditions. The sideband drive ($\Omega_d(t)$, green line) is

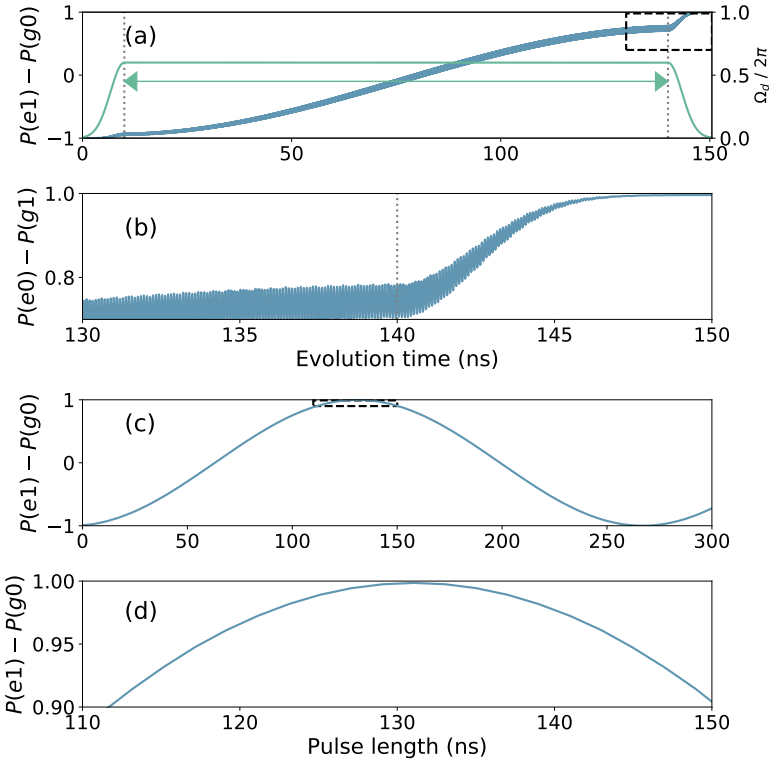

Figure 5.5: Illustration of the method of the numerical simulations. (a) The blue line indicates the dynamics of the system when the driving frequency satisfies the matching condition of the TMS interaction for given driving amplitude ($2\pi \times 300$ MHz). $P(e1)$ and $P(g0)$ refer to the population of each state. We assume the time-dependence in the sideband driving amplitude (green line), with 10 ns rising and falling time. The definition of the driving pulse length is graphically depicted by green arrow. We adjust the pulse length such that almost a full state transfer from $|e1\rangle$ to $|g0\rangle$ takes place. (b) The area enclosed by the dashed square in (a) is zoomed in. A significant change in $P(e1)$-$P(g0)$ can be identified. (c) We repeat the simulation with a various pulse length and plot $P(e1)$-$P(g0)$ at the end of each pulse. (d) The area enclosed by the dashed square in (c) is zoomed in. The fidelity of the state transfer from $|e1\rangle$ to $|g0\rangle$ is 99.85 %.

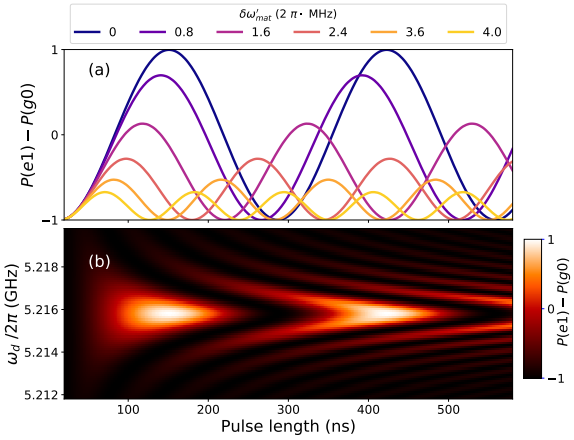

Figure 5.6: Driving frequency sweep in the numerical simulation. (a) Time-domain simulations of TMS interaction with various $\delta\omega'_{mat}$. (b) Continuously scanning the driving frequency near the matching condition. Given driving amplitude is $2\pi \times 300$ MHz. See the text for the system parameters used in the simulation.

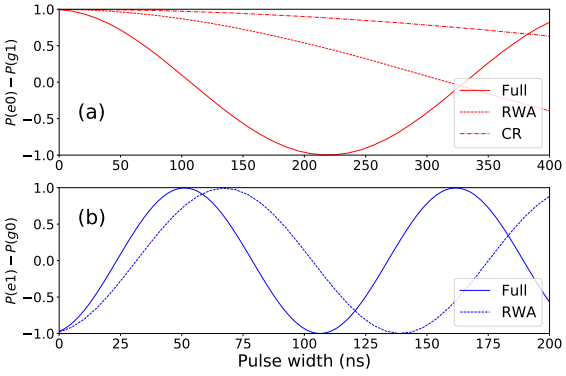

Figure 5.7: Time-domain plots of the numerical simulation results. The plots in Top (a) and bottom (b) panels are time-domain dynamics of the BS and TMS interactions respectively. In both cases, $\omega_q^{(0)} = 2\pi\times$ 6.5 GHz $\omega_q^{(0)} = 2\pi\times$ 4.0 GHz, $g/2\pi$ =200 MHz, $\chi_t/2\pi$=200 MHz and $\Omega_d/2\pi$=600 MHz are chosen. Full : Simulations with $\hat{H}_{tot}^{(0)}$. RWA : With only co-rotating driving terms in $\hat{H}_d^{(0)}$, CR : With only counter-rotating driving termsin $\hat{H}_d^{(0)}$

.

given as a pulse with 10-ns of Gaussian rising and falling. The arrow indicates the length of the pulse. Fig. 5.5b shows the area enclosed by the dashed square in Fig. 5.5a. One can identify the qubit and resonator states significantly vary during the rising and falling duration of the sideband pulse. In Fig. 5.5c, we sweep the length of the sideband pulse and plot the states of the system at the end of the pulse. We obtain a clear sinusoidal curve. Fig. 5.5d shows the area enclosed by the dashed square in Fig. 5.5c.

We sweep the driving frequency for each simulation data point and find the optimal frequency that yields the resonant sideband transitions. This procedure is described in Fig. 5.6. We chose the w_d when the oscillation has a maximum contrast. We present the simulation data with different driving Hamiltonian in Fig. 5.7. The solid lines refer to the results with a full driving Hamiltonian containing both co- and counter-rotating terms. The dotted lines (dashed lines) are obtained by the simulations with only co-rotating (counter-rotating) terms in the driving Hamiltonian. See the caption for the detail conditions in the simulations.

5.8. APPENDIX-EXPERIMENTAL METHODS

5.8.1. EXPERIMENTAL SETUP

An optical microscope image of the device is given in Fig. 5.8a. The device is comprised of a transmon and two co-planar waveguide resonators. The design of the device is the same as the one used in our previous work [47]. Only one of the resonator was used in the experiment. Besides, there is a drive line directly coupled to the transmon. The base layer of the circuit is fabricated from 100 nm niobium titanium nitride (NbTiN) film on a Silicon substrate. The detail precudure to prepare the NbTiN film is described in [39]. The transmon is comprised of a Al-AlOx-Al Josephson junction and a finger capacitor. The transmon is not flux tuneable and therefore the frequecy is insensitive to the external magnetic field noise.

A cryogenic wiring diagram and measurement electronics are given in Fig. 5.8b. The device is mounted at the mixing chamber plate of a Bluefors LD-400 dilution fridge. The temperature of the plate is around 10 mK during the measurements. The device is enclosed within a cylindrical cooper shield to block the infrared radiation. To block the external magnetic fields, the copper can is enclosed by a Aluminum shield and two Mu-metal shields. The shields are not represented in the figure. We used a vector network analyzer (Keysight N5222A) to measure the resonator transmissions. An additional microwave source (Keysight N5183B) was used for sideband drivings. We used a non-dissipative low pass filter (Minicircuit VFL-3800+) in the drive line (third column).

5.8.2. DEVICE PARAMETERS EXTRACTION

In this section, we provide the procedure to calibrate the cross anharmonicty (A_{tr}) between the transmon and resonator modes in the experiment. We use the fact that the EIT transmission spectrum of the resonator depends on the A_{tr} in the nonlinear response regime. In Fig. 5.9, we simulate the resonator transmission spectrum with a beam spliter interaction ($\Omega_{sb}/2\pi$ = 1.2 MHz). The model we used in the simulation is based on Eq. (3) in the main text including dissipation operators. Also, we set $\delta\omega_{mat}/2\pi$ by -300 kHz. In the simulation, the linewidths of the resonator and transmon modes are the same with

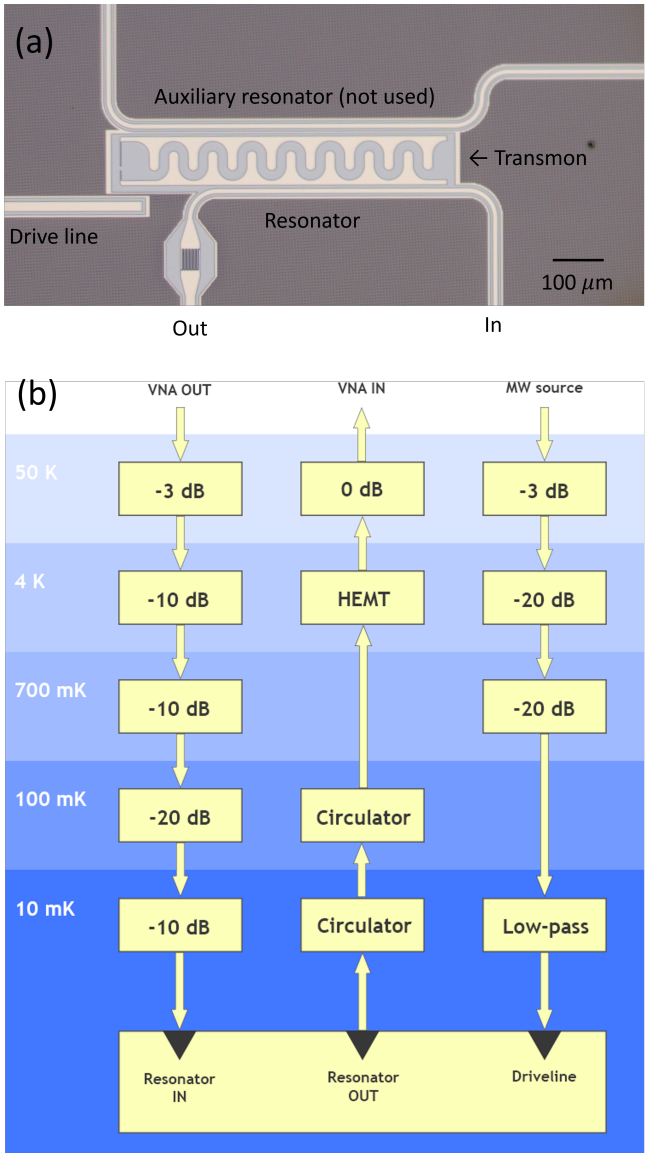

Figure 5.8: Experimental setup. (a) An optical microscope image of the device used in the experiment. (b) A cryogenic wiring diagram and measurement electronics.

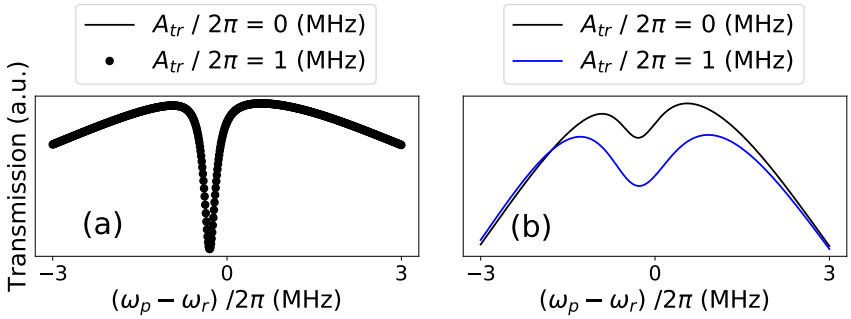

Figure 5.9: Effect of the cross anharmonicity (A_{tr}) in the resonator transmission when a beam spliter interaction is applied. The beam spliter interaction between the transmon and resonator modes are applied in the simulation. (a) In the linear response regime (weak probe, $\Omega_p/2\pi$ = 10kHz), the cross anharmonicity does not make a difference in the spectrum. (b) In the nonlinear regime (strong probe, $\Omega_p/2\pi$ = 3MHz), we can easily confirm the effect of the A_{tr} from the spectrum.

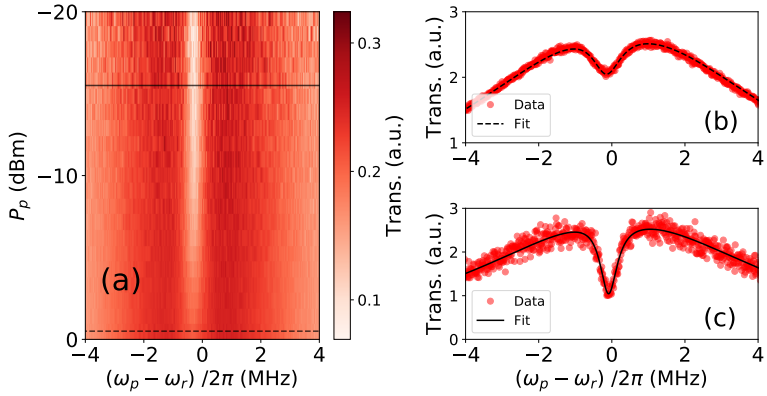

Figure 5.10: Calibration of the cross anharmonicity (A_{tr}). (a) The transmission spectrum of the resonator while scanning probe power (P_{in}). The transmon and the resonator modes are coupled by a beam splitter interaction. Horizontal dashed and solid line indicate the data when P_{in} is 0 dBm and -15dBm respectively. (b-c) The spectrum at the probe powers indicated in (a) with horizontal lines. The circles are experimental data and the solid curves are fits based on Eq.3 in the main text. From the linear response date (c), we extract Ω_{sb}, ω_d, ω_r,κ and γ by the fitting. When fitting the data in (b), these quantities are fixed with the extracted values obtained from (c). Then we extract Ω_p and A_{tr}

.

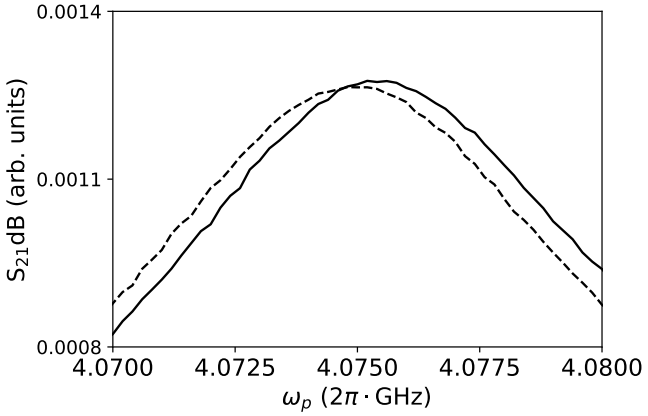

Figure 5.11: Calibration of the cross anharmonicity (A_{tr}) from the resonator response. The lines indicate the resonator transmission when the transmon is the ground state (solid) and approximately 50:50 mixed state between the ground and first excitation states (dashed). The resonance is shifted by 520 kHz.

those in the experiment. We simulate in both linear response (Fig. 5.9a) and nonlinear response (Fig. 5.9b) regimes. In linear response regime, we cannot distinguish the A_{tr} from the transmission. Meanwhile, the effect of the A_{tr} is prominent in the nonlinear response regime.

Fig. 5.10a shows the measured resonator transmission spectrum while sweeping the probe power. P_p is the resonator probe power measured at the output port of the vector network analyzer (VNA). One can notice that the contrast of the transparency window near the center decreases with increasing probe power. We first fit the resonator transmission data in the linear response regime (solid line), setting Ω_{sb}, ω_d, ω_r, κ and γ as free parameters. Then, we fit the data in the nonlinear response regime (dashed line) while fixing all the parameters obtained from the first fitting and only Ω_p and A_{tr} are free fitting parameters. When fitting the data in the linear response regime, we set $A_{tr} = 0$ and $\Omega_p/2\pi$=10 kHz. The choice of A_{tr} can be justified since we already know A_{tr} hardly affects the transmission in the linear response regime. Fitting results in both regimes are given in Fig. 5.10b and Fig. 5.10c. We obtain $A_{tr}/2\pi$=497 kHz and $\Omega_p/2\pi$=4.35 MHz from the data in the nonlinear regime.

We can also obtain A_{tr} from the fact that the resonator transition frequency depends on the transmon's quantum states. Fig. 5.11 shows how the resonator transmission spectrum changes as populating the transmon's first excited state. We drive the transmon mode with its resonant frequency and increase the power until we cannot see the further shift in the resonator frequency. With this drive power, we can approximate the transmon's state 50:50 mixed state between the ground and first excited states. We observe a frequency shift of 520 kHz, which can be interpreted as A_{tr}.

A_{tr} extracted from Fig. 5.11 is slightly larger than the value obtained from Fig. 5.10. The discrepancy of the expected sideband transition rates based on both is about 2 percent. In the main text, we use $A_{tr}/2\pi$=497 kHz obtained from Fig. 5.10. This approach is

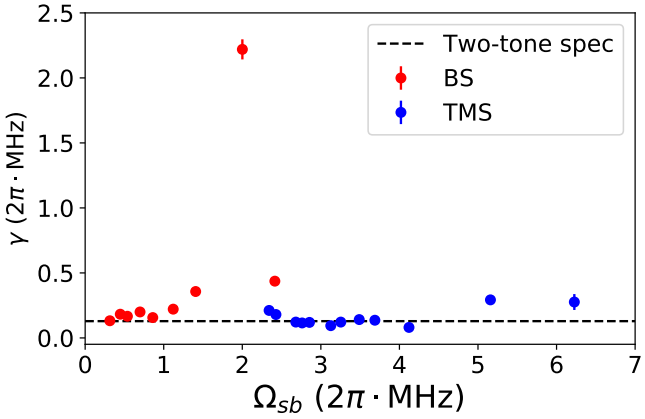

Figure 5.12: Comparison between the qubit decay rates (γ) extracted from the EIT spectrum fitting (dots) and the two-tone spectroscopy with a low probe and spectroscopy power (solid line).

advantageous as we can extract the resonator probe power and A_{tr} simultaneously, and consequently it guarantees more consistency.

5.8.3. TRANSMON DECAY RATE ANALYSIS

In the fitting process to extract the sideband transition rates, the free fitting parameters other than Ω_{sb} are γ and $\delta\omega_{mat}$. We also present the extracted values for γ and $\delta\omega_{mat}$ in [92]. In this section, we especially focus on the γ. Fig. 5.12 shows the fitted γ (dots) with respect to corresponding Ω_{sb}. These values are consistent with the γ from the low power two-tone spectroscopy (dashed line) in general. For BS interaction case, some data points far deviate from the dashed line. We attribute this to the undesired higher order sideband interactions. The matching frequency for BS interaction is close to the matching frequency for single-photon assisted sideband interaction between $|e0\rangle$ and $|g2\rangle$. Since the resonator mode has a much larger decay rate, this undesired interaction can increase the effective decay rate of the transmon mode. The rightmost two data of TMS interaction case also far deviate from the solid line. We cannot find the systematic reason for the discrepancy. We could attribute it to the fluctuation of the transmon's decay rate with respect to time.

5.9. APPENDIX-ADDITIONAL ANALYTICAL AND NUMERICAL ANALYSIS

In this section, we confirm that Eq. 5.6 more accurately predicts the $\delta\omega_t$ and Ω_{sb} than Eq. 6.7. In Fig. 5.13, we compare the analytical calculation based on Eq. 6.7 and numerical simulation results in Fig. 5.4. We can clearly see the discrepancy between the analytical and numerical results becomes larger than that in Fig. 5.4.

In Fig 5.14, we perform the additional simulation with various system parameters and compare the numerically simulated sideband transition rates (Ω_{sb}-Sim) to the the-

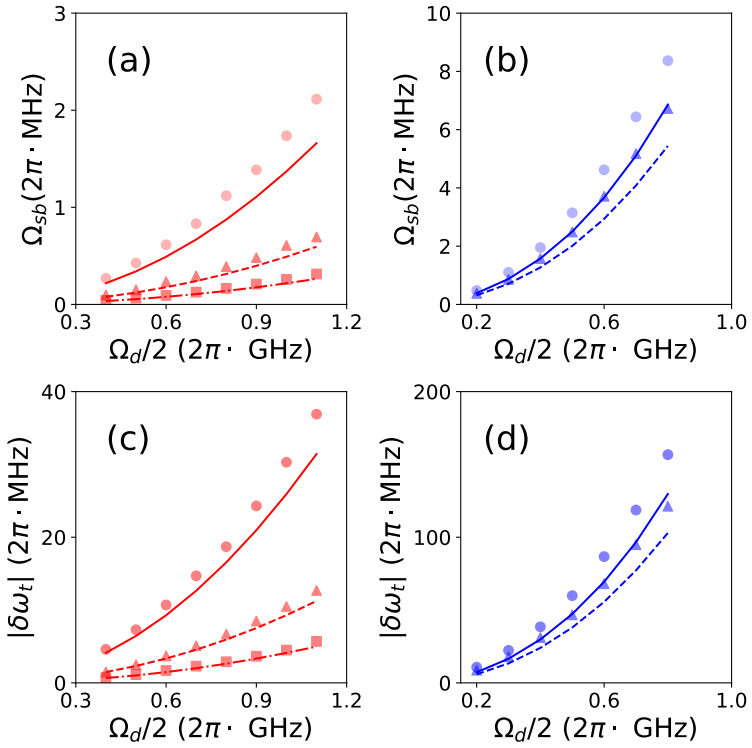

Figure 5.13: comparison between analytical and numerical calculations. All the contents in the figures are the same as Fig 5.4 except that the lines are obtained based on Eq. 6.7.

oretical calculations (Ω_{sb}-Th). We compare two different theoretical approaches based on Eq. 6.7 and Eq. 5.6 respectively. Except the one case (Fig 5.14-d), Ω_{sb}-Th based on Eq. 5.6 are closer to Ω_{sb}-Sim. Even in Fig 5.14-d, Ω_{sb}-Th based on Eq. 5.6 is more accurate with low driving amplitudes.

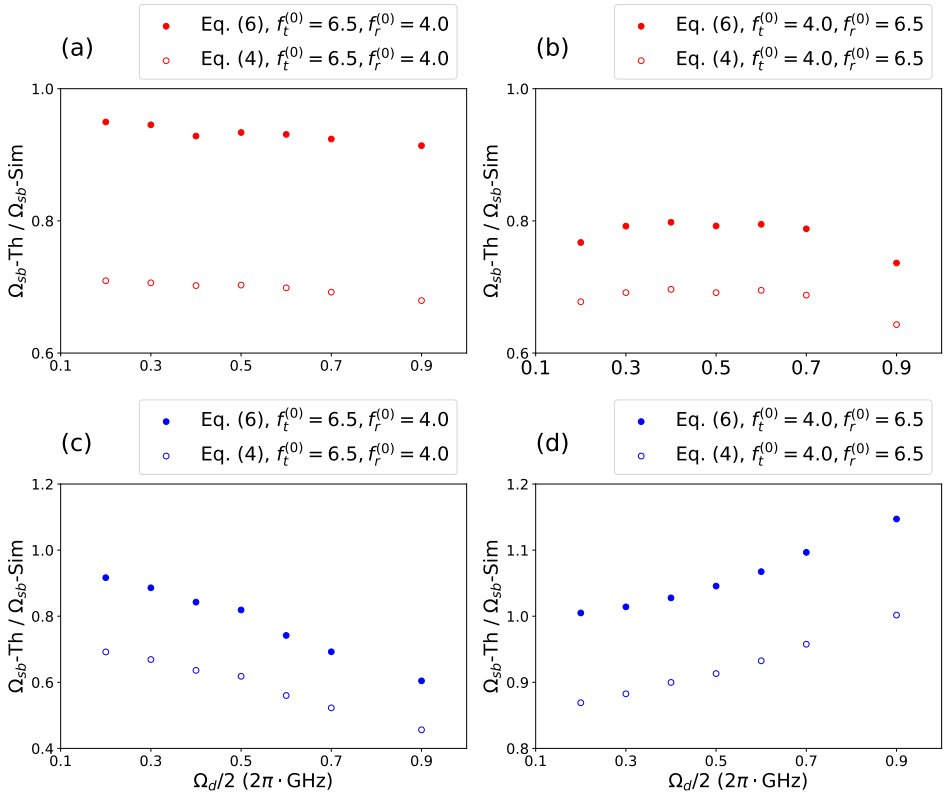

Figure 5.14: Additional simulation results (Ω_{sb}-Sim) and comparison to the analytical theory (Ω_{sb}-Th). (a-b) BS interaction. (c-d) TMS interaction. Simulation is performed with four different system parameters (see legend). $f_{t,r}^{(0)}$ are defined by $\omega_{t,r}^{(0)}/2\pi$. $g/2\pi$ in the simulation is 200 MHz. $f_{t,r}^{(0)}$ in (a,c) are 6.5 and 4.0 GHz respectively. $f_{t,r}^{(0)}$ in (b,d) are 4.0 and 6.5 GHz respectively.

6

TUNEABLE AND WEAKLY-INVASIVE PROBING OF A SUPERCONDUCTING RESONATOR BASED ON ELECTROMAGNETICALLY INDUCED TRANSPARENCY

Superconducting cavities with high quality factors play an essential role in circuit quantum electrodynamics and quantum computing. In measurements of the intrinsic loss rates of high frequency modes, it can be challenging to design an appropriate coupling to the measurement circuit in such a way that the resulting signal is sufficiently strong but also that this coupling does not lead to unwanted loading circuit, obscuring the intrinsic internal loss rates. Here, we propose and demonstrate a spectroscopic probe of high-Q resonators based on the phenomena of electromagnetically-induced transparency (EIT) between the resonator and qubit in the weak dispersive coupling regime. Applying a sideband drive signal to the qubit, we observe an interference dip originated from EIT in the qubit spectroscopy, originating from the quantum interference between the qubit probe signal and sideband transition. From the width and the depth of the dip, we are able to extract the single-photon linewidth of the resonator from an analytical model. Working in a previously unexplored regime in which the qubit has a larger linewidth than the resonator reduces the technical challenge of making a high-coherence qubit and is advantageous for remaining in the weakly-invasive limit of coupling to the resonator. Furthermore, the sideband and the dispersive coupling between the resonator and the qubit can be tuned in situ controlling the strength of the sideband drive power. This in-situ tuneability allows the technique to be applied for efficient measurement of the resonator loss

Parts of this chapter has been published in Physical Review A **102** 053721 (2020).

rate for any quality factor below a fixed upper bound, on the order of 10^8 *for our device, allowing a wide range of quality factors to probed using a single design.*

6.1. INTRODUCTION

Superconducting resonators with high quality factors play an important role in the fields of quantum science and information. One example includes quantum computing based on encoding of quantum information in the bosonic modes represented superconducting resonators, which is particularly attracive for the implementation of quantum error correction [[22], [23]]. In this scheme, a harmonic system such as an ion's mechanical mode or a photonic mode carries the quantum information instead of a two-level quantum bit [[23], [24]]. For these, and many other, applications, a longer lifetime of the resonator is highly desired. However, in order to implement near-lossless resonators, it is crucial to have a technique that is able to determine what the intrinsic linewidth is of the superconducting resonator at the single photon level.

A common spectroscopy approach for determining the loss rate of a superconducting resonator is to couple the resonator to external transmission lines and measure its transmission or reflection spectrum. A disadvantage of this approach is that the resonator loss rate induced by the external channel (κ_e) can dominate the total loss rate κ of the resonator. In principle, internal and external loss rates ($\kappa_{i,e}$) can still be independently extracted, although in practice imperfections in the microwave impedance of the measurement setup can result in asymmetric lineshapes that complicate the independent determination of the two [93], [94]. In particular, extracting κ_i can become challenging when $\kappa_e \gg \kappa_i$. One approach for mitigating this problem is to ensure that $\kappa_e \ll \kappa_i$, in which case the internal loss rate is determined by the total linewidth [95]. A disadvantage of this approach, however, is that the signal-to-noise ratio of the measurement is reduced, and it can become challenging to measure at single-photon excitation levels.

Determining the appropriate value of κ_e to design for such spectroscopy requires *a priori* estimate of the order of magnitude of κ_i, which presents a challenge as the value of κ_i can be difficult to predict. This is a problem in particular in planar resonators, in which κ_i can be strongly affected by surface contamination that is difficult to control. An alternative non-invasive technique, which is unaffected by the possible unknown impedances of external circuitry and in which the coupling to the resonator can be tuned in-situ, could be advantageous for spectroscopy of superconducting cavities.

Here, we present a weakly-invasive spectroscopic probe of a superconducting resonator using a qubit in the weak dispersive coupling limit. The underlying principle is based with electrically induced transparency (EIT) [96–102]. When the qubit has a broader linewidth than that of the resonator, if the sideband coupling is smaller than the difference between them (EIT regime), we can find a narrow dip in the qubit population spectrum, which is a strong indication of EIT. From these measurements, The qubit and resonator decay rate can be extracted independently using a model of the EIT process. As long as the sideband coupling can be made the same order of magnitude as the resonator linewidth, one can extract the decay rate of the resonator in a way that is insensitive to the error in the qubit decay rate.

The EIT-based spectroscopy approach is weakly invasive in the sense that it is sufficient that the qubit and the resonator are in the weak dispersive coupling, in which there is very little direct hybridisation between the two. Consequently, loss rate through the qubit (κ_q) can be chosen to be negligible. In the presence of a sideband drive of ap-

propriate frequency, the drive induces a predictable and tunable hybridisation between the qubit and resonator through sideband transitions, which is the technique we apply here to perform resonator spectroscopy. Furthermore, being based on inducing a small EIT window in the qubit spectrum, our approach does not require high coherence qubit, and wide ranges of values of κ_i of the resonator can be accurately probed in spectroscopy by tuning the sideband drive power.

We experimentally demonstrate this scheme with experimental observations using a device based on a transmon qubit [20] coupled to a coplanar waveguide (CPW) resonator. The work presented here demonstrates a application of EIT related physics in a weak dispersive coupling regime. EIT with a circuit quantum electrodynamics (QED) platform has already been reported in several configurations [99–102] but the present paper is the first study of EIT related phenomena with a dispersively coupled resonator and a qubit system when the qubit has a broader linewidth.

This chapter is organized as follows. In Sec. 6.2, we discuss theoretical background of this work. We present experimental results in Sec. 6.3. We provide analysis of the results, discussion on a major error source and a further direction of the study in Sec. 6.4. A summary of this work is given in Sec. 6.5.

6.2. THEORETICAL DESCRIPTION

6.2.1. QUBIT POPULATION SPECTRUM UNDER SIDEBAND DRIVING

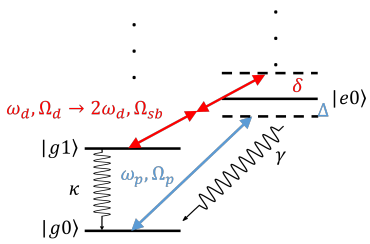

Figure 6.1: Energy level diagram describing the system of a dispersively coupled target resonator and qubit. Red arrows indicates an off-resonant two-photon drive field for enabling two-photon sideband transitions. The blue arrow indicates a weak resonant field for probing the qubit. The readout resonator is omitted in the diagram.

The system studied is depicted in Fig. 6.1. A two-level qubit is dispersively coupled to a target resonator whose internal loss rate is our interest. We induce a first order sideband transition with a coupling rate of Ω_{sb} that couples $|g,n\rangle$ and $|e,n-1\rangle$ (red arrows) through an external coherent drive with frequency ω_d. The first order sideband transition is dipole forbidden for transmon qubits as described in [19]. Therefore, a two-photon process is used to enable this transition in this work.

In the figure, $|g\rangle$ and $|e\rangle$ refer to the ground and excited state of the qubit. The numbers refer to the photon number of the target resonator. The target resonator frequency and the Stark-shifted transition frequency of the qubit are ω_t and ω_q respectively. Their decay rates are given by κ and γ respectively. A weak field (blue arrow) probes the qubit transition. We define the detuning between qubit and probe $\omega_q - \omega_p$ to be Δ. Also, we de-

fine δ as $\omega_q - \omega_t - 2\omega_d$. These definition are also graphically presented in Fig. 6.1. In the real device, we additionally have a readout resonator coupled dispersively to the qubit, which is not present in Fig. 6.1. We will also omit the readout resonator in the following mathematical derivation since it has no role in featuring the EIT.

The effective Hamiltonian of the system in Fig. 6.1 is

$$\begin{aligned}\hat{\mathscr{H}} = &\frac{\omega_q}{2}\hat{\sigma}_z + \omega_t \hat{a}^\dagger \hat{a} - 2\chi_{qc}\hat{\sigma}_z \hat{a}^\dagger \hat{a} \\ &+ \frac{\Omega_{sb}}{2}\left(\hat{a}\hat{\sigma}_+ e^{-2i\omega_d t} + \hat{a}^\dagger \hat{\sigma}_- e^{+2i\omega_d t}\right) \\ &+ \frac{\Omega_p}{2}\left(\hat{\sigma}_+ e^{-i\omega_p t} + \hat{\sigma}_- e^{+i\omega_p t}\right),\end{aligned} \tag{6.1}$$

where $\hat{\sigma}_z$ denotes the Hamiltonian of the two-level qubit, $\hat{\sigma}_\pm$ are the raising and lowering operators of the qubit state, and $2\chi_{qt}$ is the dispersive shift between the qubit and the resonator. The external drive results in a negligible change of the dispersive shift [19] and is therefore neglected. By applying the following time-dependent unitary transform,

$$\hat{\mathscr{U}} = \exp\left[i(\omega_p - 2\omega_d)t\hat{a}^\dagger \hat{a} + i(\omega_p)t\hat{\sigma}_z\right]. \tag{6.2}$$

the Hamiltonian can be simplified to

$$\begin{aligned}\hat{\mathscr{H}}' = &\frac{(\omega_q - \omega_p)}{2}\hat{\sigma}_z + (\omega_c + 2\omega_d - \omega_p)\hat{a}^\dagger \hat{a} - 2\chi_{qt}\hat{\sigma}_z \hat{a}^\dagger \hat{a} \\ &+ \frac{\Omega_{sb}}{2}\left(\hat{a}\hat{\sigma}_+ + \hat{a}^\dagger \hat{\sigma}_-\right) \\ &+ \frac{\Omega_p}{2}\left(\hat{\sigma}_+ + \hat{\sigma}_-\right).\end{aligned} \tag{6.3}$$

Here, we can use the definitions of $\Delta = \omega_q - \omega_p$ and $\delta = \omega_q - \omega_t - 2\omega_d$; Both Δ and δ are as defined in Fig. 6.1 to simplify the expression. Then, the Hamiltonian takes the form

$$\begin{aligned}\hat{\mathscr{H}}' = &\frac{\Delta}{2}\hat{\sigma}_z + (\Delta - \delta)\hat{a}^\dagger \hat{a} - 2\chi_{qt}\hat{\sigma}_z \hat{a}^\dagger \hat{a} \\ &+ \frac{\Omega_{sb}}{2}\left(\hat{a}\hat{\sigma}_+ + \hat{a}^\dagger \hat{\sigma}_-\right) \\ &+ \frac{\Omega_p}{2}\left(\hat{\sigma}_+ + \hat{\sigma}_-\right).\end{aligned} \tag{6.4}$$

The dynamics of the system is then given by the Lindblad equation:

$$\begin{aligned}\frac{d\hat{\rho}}{dt} = &-\frac{i}{\hbar}\left[\hat{\mathscr{H}}'(t), \hat{\rho}(t)\right] \\ &+ \frac{\gamma}{2}\mathscr{D}[\hat{\sigma}_-]\rho + \frac{\kappa}{2}\mathscr{D}[\hat{a}]\rho + \frac{\gamma_\phi}{2}\mathscr{D}[\hat{a}^\dagger \hat{a}]\rho,\end{aligned} \tag{6.5}$$

where $\mathscr{D}[\hat{\mathscr{O}}]\hat{\rho} = 2\hat{\mathscr{O}}\hat{\rho}\hat{\mathscr{O}}^\dagger - \hat{\mathscr{O}}^\dagger\hat{\mathscr{O}}\hat{\rho} - \hat{\rho}\hat{\mathscr{O}}^\dagger\hat{\mathscr{O}}$, κ is the decay rate of the target resonator, and γ is that of the qubit. γ_ϕ is the pure dephasing rate of qubit. From the steady state solution $\hat{\rho}_{ss}$ that satisfies $d\hat{\rho}_{ss}/dt$=0, one can obtain the steady state qubit population by tracing out the resonator state, $\rho_{ee} = \mathrm{Tr}_{res}[\hat{\rho}_{ss}(1+\hat{\sigma}_z)/2]$.

6.2.2. RESONATOR SPECTROSCOPY AT SINGLE-PHOTON LEVELS USING SIDEBAND TRANSITIONS

When $|\gamma+2\gamma_\phi-\kappa|>\Omega_{sb}$ and $\gamma+2\gamma_\phi>\kappa$, the sideband transition leads to a narrow transparency window in the qubit transmission spectrum. This results from the interference between two different transitions, $|g,n+1\rangle\rightarrow|e,n\rangle$ and $|g,n\rangle\rightarrow|e,n\rangle$. In this work, we measure the population of qubits ρ_{ee} rather than the transmission $\mathrm{Im}[\rho_{eg}]$. We define the qubit spectrum as the response of its average population as a function of the probe frequency $\rho_{ee}(\omega_p)$. In Fig. 6.2(a), we simulate the qubit population spectrum with reasonable parameters satisfying the EIT condition based on the master equation in Section 6.2.1. We can also find the same features of the transmission spectrum in the qubit population spectrum as well. A Lorentzian dip in the qubit population spectrum, in the following we will refer to this as an 'interference dip', is characterized by its width (w) and minimum population (d).

In the linear response limit ($\Omega_p\ll\Omega_{sb}$) and for zero detuning ($\delta=0$), the width and depth of the dip are given by $w\sim\gamma+2\gamma_\phi+\kappa-\sqrt{(\gamma+2\gamma_\phi+\kappa)^2-\Omega_{sb}^2}$, $d\sim\omega_p/(\gamma+2\gamma_\phi+\frac{\Omega_{sb}^2}{\kappa^2})$ and the total linewidth is $h\sim\gamma+2\gamma_\phi$ [102]. When Ω_p and χ_{qt} are known, κ,γ,γ_ϕ and Ω_{sb} together characterize the population spectrum and thus one can extract these by fitting the spectrum to the model calculated by the master equation in Section 6.2.1.

Too small a value of Ω_p requires an excessive measurement time. Fortunately, although $\Omega_p\ll\Omega_{sb}$ does not hold in the present simulation in Fig. 6.2(a), we can clearly see the dip in the spectrum unless the Ω_p is excessively large. Nevertheless, the upper bound on Ω_p sets a limit to the feasibility of our approach for investigating a single-photon level resonator loss rate. In the experiment, Ω_p is separately calibrated as described in Appendix 6.9. Also, χ_{qt} can be calculated from the device parameters. In this work, since the qubit is weakly coupled to the resonator, the calculated χ_{qt} is only $2\pi\times7.8$ kHz. With this magnitude, it hardly affects the spectrum and we confirm that neglecting χ_{qt} does not make a significant difference in the fitting results.

In order to achieve the EIT condition, it is possible to achieve a sufficient sideband coupling rate Ω_{sb} for spectroscopy even with a very weak dispersive coupling between the qubit and the resonator. To be able to extract the intrinsic resonator linewidth accurately from the fits, one needs to be in the regime of $\Omega_{sb}\sim\kappa$. By using a strong sideband drive strength, this can be achieved in a limit where the dispersive coupling to the qubit results in a negligible modification of the resonator linewidth.

Specifically, the contribution of the dispersive coupling to the qubit to the resonator loss rate, which we denote as κ_q, scales with $(g_{qt}/\Delta_{qt})^2$, where g_{qt} and Δ_{qt} are bare coupling rate and detuning between the qubit and the target resonator respectively. By arranging a large detuning between the qubit and the target resonator, this can be made negligbly small. The sideband coupling Ω_{sb}, however, scales as $g_{qt}(\Omega_d/\Delta_{qd})^2$, where Δ_{qd} is $\omega_q-\omega_d$. The large Δ_{qd} can be compensated for by a large sideband drive strength. In this way, the EIT spectroscopy technique can be made minimally invasive on the resonator it is probing. This is in contrast, for example to other qubit-based spectroscopy approaches [103] that requires a strong dispersive coupling. We also note that while the sideband drive strength is strong, it is highly off-resonant from the resonator itself and the occupation number of the resonator remains negligible.

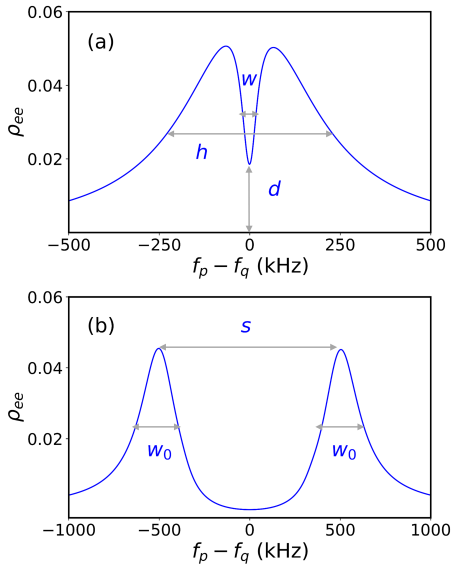

Figure 6.2: Single-photon resonator spectroscopy through sideband transition. δ is set to 0 for both the EIT and ATS regime simulations. (a) Simulated qubit population spectrum in EIT regime when the parameters $\Omega_{sb}, \Omega_p, \gamma, \gamma_\phi, \kappa, \chi_{qt}$ are $2\pi\times$(100,100,400,0,30,10) kHz (solid line). As an indication of the electromagnetically induced transparency, a Lorentizan dip (interference dip) appears in the qubit population spectrum, which is characterized by its width w and minimum population d. (b) Simulated qubit population spectrum in ATS regime when the parameters $\Omega_{sb}, \Omega_p, \gamma, \gamma_\phi, \kappa, \chi_{qt}$ are $2\pi\times$(1000,100,400,0,30,10) kHz (solid line). In this regime, the spectrum has two peaks separated by s and their widths are both w_0. In the simulation, we set $\gamma_\phi = 0$, typically condition for the fixed frequency transmon qubit used in our experiment. In Sec. 6.6, we present additional simulation results that show how the γ_ϕ changes the qubit population spectrum.

In Fig. 6.2(b), we also simulate the qubit population spectrum when the Auther—Towns splitting [104] condition $\left|\gamma+2\gamma_\phi-\kappa\right|<\Omega_{sb}$ holds. Unlike EIT, ATS arises from the result of electromagnetic pumping that results in a dressed normal mode splitting of the two modes in the rotating frame of the pump. In circuit QED platform, ATS is also widely explored in several configurations [104–107]. When $\delta=0$, the spectrum has two symmetric peaks separated by Ω_{sb} and each linewidth is equal to $(\gamma+2\gamma_\phi+\kappa)/2$. Both the qubit and resonator decay equally characterize the linewidth of each peak. Thus, one cannot set both κ and γ as free fitting parameters and thus the qubit decay rate should be separately calibrated. This can be more problematic if an extremely small decay rate of resonator is expected. In this case, the measured resonator decay rate becomes sensitive to the error in the qubit decay rate measurement, unless the qubit decay rate is much smaller than the resonator's decay rate, which imposes a challenging requirement on the preparation of the device.

6.3. EXPERIMENT

6.3.1. DEVICE CONFIGURATION

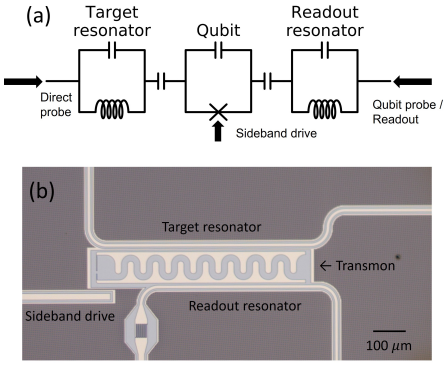

Figure 6.3: Experimental setup. (a) Simplified circuit diagram of the device used in the experiment. (b) Optical microscopy image of the superconducting circuit.

Fig. 6.3(a) presents a simplified circuit diagram of the device used in the experiment. More detailed information on the circuit design and related electronics can be found in Appendix 6.7. A transmon qubit ($\omega_{q0}/2\pi$=6.723 GHz, without sideband drive) is capacitively coupled to two $\lambda/4$ co-planar waveguide (CPW) resonators. One is the target resonator ($\omega_t/2\pi$=2.9 GHz). The other is the readout resonator ($\omega_r/2\pi$=4.07 GHz) to measure the qubit population more efficiently. Both are dispersively coupled to the qubit with dispersive coupling $\chi_{qt}/2\pi$=7.8 kHz and $\chi_{qr}/2\pi$=1.3 MHz to the target and readout resonators respectively. The bare coupling between each resonator and qubit is estimated by $g_{qt}/2\pi=58$ MHz and $g_{qr}/2\pi=193$ MHz respectively. Qubit decay rate γ is around $2\pi\times$400 kHz. Each resonator is inductively coupled to different feedlines. These values yield qubit limited resonator decay rate $\kappa_q/2\pi\approx 100$Hz, which is far below than typically achieved internal loss rate in our lab (around $2\pi\times 5-20$ kHz.)

We use a single-junction fixed frequency qubit and therefore its transition frequency

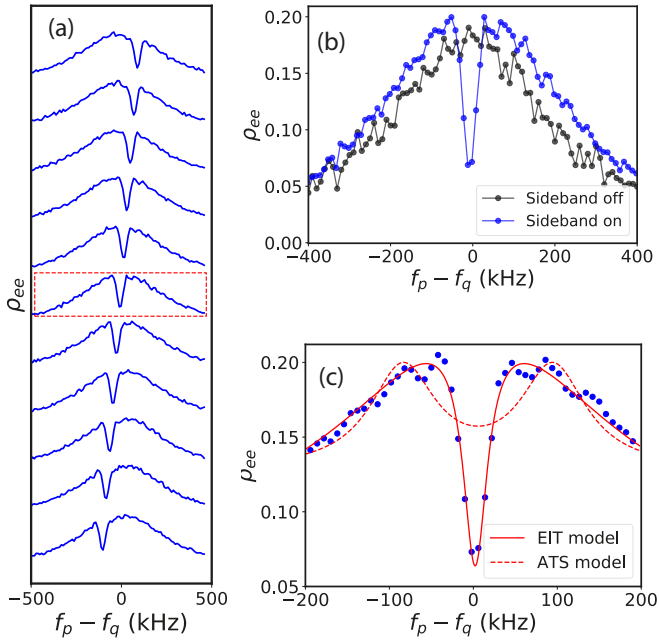

Figure 6.4: Observation of interference dip in a qubit population spectrum. (a) Observation of interference dip in qubit population spectrum while scanning δ from -200 to 200 kHz. The spectrum when $\delta = 0$ is enclosed by a red box. (b) Comparison between qubit population spectrum with (blue) and without (black) sideband field. (c) A separate measurement near the interference dip with finer step. The validity of the EIT model is confirmed while the ATS model breaks down.

is insensitive to magnetic flux noise, a strong source of dephasing in flux tuneable transmon qubits. This is also experimentally confirmed by the observation of $T_2 \simeq 2T_1$ in separate time domain measurements given in Appendix 6.8. Although it is not necessary in our case, it could be advantageous to use a flux tuneable qubit, with which κ_q is *in situ* tuneable by adjusting the detuning to the ressonator. The technique and analysis present here is also applicable for the flux tuneable qubit. We discuss how our scheme is extended for the flux tuneable qubit in Sec. 6.4.4.

The optical microscopy image of the circuit can be found in Fig. 6.3(b). The transmon qubit and CPW resonators were patterned on a 100 nm niobium titanium nitride (NbTiN) film on a Silicon substrate [39]. The Josephson junction of the qubit is made by Al-AlOx-Al.

6.3.2. EXPERIMENTAL RESULTS

We apply the sideband drive directly to the Josephson junction of the circuit through the direct drive line (middle arrow in Fig. 6.3(a)). The qubit probe Ω_p is applied through the feedline coupled to the readout resonator (right arrow). In addition, we have a direct probe of the target resonator (left blue arrow). We use in all four microwave sources in the experiment. One is used for the qubit probe, another for the qubit readout, another for the sideband drive, and the remaining one for the direct resonator probe. In order to avoid measurement induced broadening in the qubit population spectrum, we performed the measurement in pulsed configuration. First, a 20-μs long probe pulse is applied, rapidly followed by a 200-ns long readout pulse. Using this pulsed readout scheme, the qubit population spectrum is unaffected by the photons in the readout resonator during qubit measurement.

Fig. 6.4(a) shows the measured interference dip in the qubit population spectrum, which results from a sideband transition between the qubit and the target resonator. The sideband drive frequency ω_d is swept around $2\omega_d = \omega_q - \omega_c$ and we find $\delta \approx 0$ when $\omega_d/2\pi$=1.945 45 GHz. The interference dip is conspicuously identified in the comparison to the spectrum without sideband transition in Fig. 6.4(b). The probe amplitude Ω_p is $2\pi \times 264$ kHz according to the calibration method presented in Appendix 6.9. The value we chose is a compromise between the high contrast of the interference dip and the proper measurement time. The sideband drive also shifts the qubit frequency. In Appendix 6.10, we present the data for how much the qubit frequency is shifted when we obtain a sufficient sideband coupling.

In addition to the process of EIT, observations similar to those in Figure 6.4 can also arise from the process of ATS. In order to distinguish EIT from ATS, one can numerically fit the data by given simplified model in linear response limit [108]. A system in the EIT regime can be modeled by

$$\rho_{ee,\mathrm{EIT}}(\omega_p) = \frac{C_+^2}{\Delta^2 + \gamma_+^2} - \frac{C_-^2}{\Delta^2 + \gamma_-^2} \tag{6.6}$$

When the system is in the ATS regime, ρ_{ee} in the linear response limit is

$$\rho_{ee,\mathrm{ATS}}(\omega_p) = \frac{C^2}{(\Delta - \Delta_0)^2 + \gamma_0} + \frac{C^2}{(\Delta + \Delta_0)^2 + \gamma_0}. \tag{6.7}$$

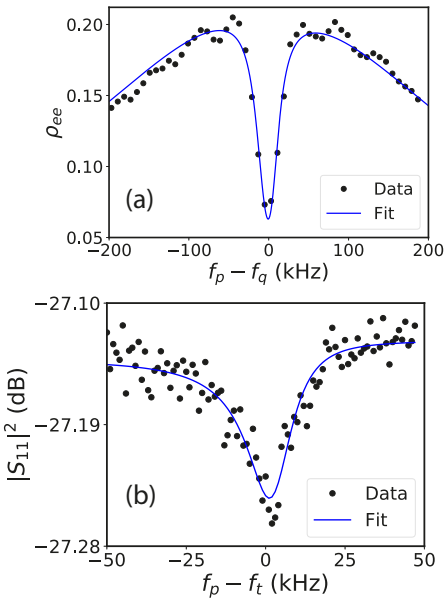

Figure 6.5: Two different spectroscopic measurement of a superconducting resonator. (a) Spectroscopy of the superconducting resonator mode using interference dip. From numerical fitting of the qubit population spectrum calculated using the master equation, we extract a resonator linewidth of $\kappa/2\pi = 20.3 \pm 1.5$ kHz. (b) A direct reflection measurement of the resonator through the weakly coupled port. Even for very weak external coupling, the resonator displays an asymmetric lineshape due to Fano resonance. From a fit to a Fano resonance lineshape, we extract a linewidth $\kappa/2\pi = 17.2 \pm 1.8$ kHz, in agreement with the results of the spectroscopy based on interference dip within the experimental error.

All the parameters in these expressions are free fitting parameters except Δ. Here, $\gamma_{0,\pm}$ is not necessarily the same with γ and γ_ϕ. We perform a numerical fit with the two different fitting models above corresponding to each phenomenon. The results are given in Fig. 6.4(c). The data is taken with the same conditions as in (b) but a different range and step of probe frequencies. While the EIT model Eq. B.1 shows excellent agreement with the data (solid line), the ATS model Eq. 6.7 fails to explain the data well. Accordingly, the fact that the system is in the EIT regime is clearly demonstrated. It is notable that the EIT model is still applicable to the data even when $\Omega_p \ll \Omega_{sb}$ does not hold.

We fit the qubit population spectrum with the numerical model in Section 6.2.1 to extract the target resonator's linewidth κ. The result is presented in Fig. 6.5(a). The data is the same as in Fig. 6.4(c). From the data, $\kappa/2\pi \approx 20.3 \pm 1.5$ kHz, $\gamma/2\pi \approx 445.95 \pm 2.4$ kHz and $\Omega_{sb}/2\pi = 112 \pm 0.5$ kHz are extracted. When $f_p = f_q$, the photon number in the target resonator is approximately 0.3, based on the master equation solution with extracted parameters. The estimated κ_q is only $2\pi \times$ 104 Hz.

We also measured the single-photon level κ by the normal reflection spectrum via a weakly coupled port in Fig. 6.5(b) to verify the above result. A Fano resonance is also considered in the fitting process. From the fitting, $\kappa/2\pi \approx 17.2 \pm 1.8$ kHz is obtained. The upper bound of the resonator photon number is approximately 1.25 based on the input power from the source of the probe, the room temperature, and the cryogenic wiring. The κ's extracted from both approaches agree within the overlapping statistical error.

6.4. DISCUSSION AND OUTLOOK

6.4.1. ANALYSIS OF THE RESULTS

We measured the single-photon level κ of the target resonator through two independent approaches. The target resonator is coupled to the external environment through the qubit (κ_q) and also the external feedline(κ_e). Both coupling rates are $2\pi \times$ 104Hz and $2\pi \times$ 112Hz respectively based on the measurement. Although these two quantities are similar, one can see significant difference in the contrast of the spectroscopic signal. In Fig. 6.5(a), the suppression of the qubit population in the EIT based spectroscopy is more than 5 dB. On the contrary, the suppression of the reflection in Fig. 6.5(b) is only 0.1 dB. This clearly shows that our approach covers much wider range of κ_i.

For given design in our work, considering an error margin of 10% on κ_q, our EIT based spectroscopy works nicely for the resonator with an internal quality factor (Q_i) up to 10^8 and a resonance frequency of 10 GHz. Since it is difficult to obtain single-photon level Q_i more than 10^8 for planar resonators, the design is already optimized for such types of device.

6.4.2. EFFECT OF QUBIT DECAY RATE FLUCTUATION ON THE MEASUREMENT

It is often observed that the decay time of a superconducting qubit can fluctuate in time [109]. If one cannot finish the measurement before the fluctuation happens, there is a resulting distortion in the qubit population spectrum. In this subsection, we model such distortion and simulate how it affects the fitted κ depending on the degree and the tendency of the fluctuation.

We assume that we rapidly sweep the frequencies, faster than the time scale of the

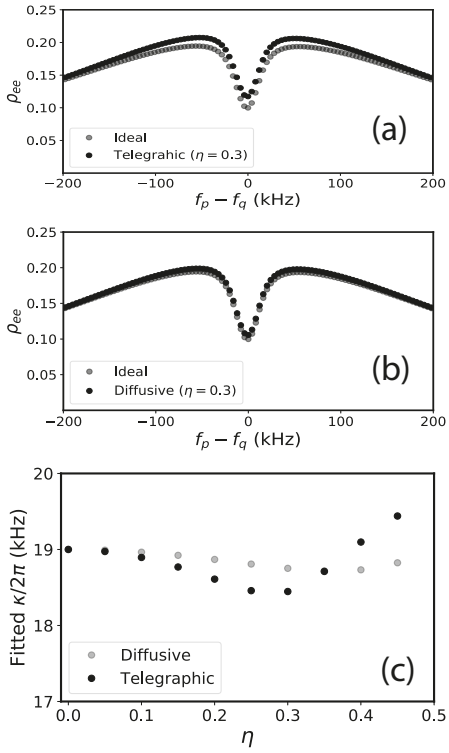

Figure 6.6: Investigation of systematic error induced by fluctuation in qubit decay rate. See main text for the detailed method and a definition of η. (a) and (b) How the qubit population spectrum varies when the qubit decay rate fluctuates in a telegraphic way (a) and a drifty way (b) when η is 0.3 for both cases. (c) Effect of the qubit decay rate fluctuation on fitted $\kappa/2\pi$. Telegraphic fluctuation (gray) has a larger effect than a drifty fluctuation (black) for given η. Mean qubit decay rate over measurement duration (γ_0) is $2\pi\times$450 kHz and $\Omega_{sb}, \Omega_p, \kappa, \chi_{qt}$ are $2\pi\times$(100,264,19,7.8) kHz in the simulation.

fluctuation, but repeat the sweeping enough to obtain an adequate signal to noise ratio. We consider two different trends in the fluctuation: telegraphic fluctuation and diffusive fluctuation[109]. In the simulation, the qubit decay rate varies from $\gamma_i = (1-\eta)\gamma_0$ to $\gamma_f = (1+\eta)\gamma_0$ during the measurement. For the telegraphic case, we assume the decay rate jumps at the middle of the measurement. For the diffusive case, the decay rate varies at a constant rate over time.

We define $\rho_{ee}(\omega_p;\gamma)$ as the qubit population spectrum when the qubit decay rate is γ. For telegraphic fluctuation, the spectrum is expressed by

$$\rho_{ee}^{tele}(\omega_p) = \frac{1}{2}[\rho_{ee}(\omega_p;\gamma_i) + \rho_{ee}(\omega_p;\gamma_f)]. \tag{6.8}$$

For diffusive fluctuation from γ_i to γ_f homogenously, the spectrum is expressed by

$$\rho_{ee}^{diff}(\omega_p) = \frac{1}{n}[\Sigma_k^n \rho_{ee}(\omega_p;\gamma_i + 2\eta k/n)], \tag{6.9}$$

where n is the number of sweeps during the measurement, set to 100 in our simulation here.

The results of the simulation can be found in Fig. 6.6. In Fig. 6.6(a) and (b), we compare the qubit population spectrums with and without qubit decay rate fluctuation for $\eta = 0.3$. The gray curves indicate the spectrum when γ is fixed at γ_0=$2\pi\times$450 kHz. The black curves indicate the spectrum distorted by fluctuations in γ. In Fig. 6.6(c), we fit the distorted spectrum with the ideal fitting model from Section 6.2.1 and how the extracted κ is affected.

6.4.3. FURTHER DIRECTION OF THE STUDY

In this work, we rely on a two-photon assisted transition, the achieved sideband coupling strength is only 0.1 percent of the bare coupling strength between the qubit and the resonator. Achieving larger couplings could be achieved by introducing other types of qubit, for example a flux qubit, with which one can address the first order sideband transition to the resonator with a single photon transition. In that case, the required bare coupling for the desired sideband coupling strength becomes significantly smaller, along with a smaller requirement for κ_q to stay in the EIT regime.

The resonator spectroscopy scheme presented here is extensible to the case of many target resonators having different frequencies, as long as a qubit is coupled to them with the proper coupling strength. Typically, the spectroscopy of multiple resonators on a chip requires a circuit design with a long feedline so that all the resonators are properly coupled to the feedline. Such a structure could induce some slotline mode and limit the scalability of the design. For our method, such a long feedline is not necessary as one only needs to feed the probe and readout pulse to the qubit, providing a relatively simple measurement technique for the spectroscopy of multiple resonators on a chip. For for this, an X-mon [110] or star-mon [111] design for the qubit, for example, would allow the single qubit to couple to multiple resonators.

6.4.4. EXTENSION TO FLUX-TUNEABLE QUBIT

As we discuss above, employing a flux-tunenable qubit enables $in-situ$ control of κ_q. This is useful when we need control $in-situ$, which is not necessary in our work. In this

case, unlike the case of the fixed frequency qubit, we need to take the pure dephasing rate of the qubit (γ_ϕ) into account. This however does not add complexity in using our scheme. As long as we have $\kappa_q \ll \kappa_i$ and $\gamma \sim \gamma_\phi$, the effect of the pure dephasing of the qubit to the resonator is still negligible. In fitting process, we would only need to include γ_ϕ in the master equation model. The effect of the pure dephasing in the qubit population spectrum is distinguishable from other parameters and therefore we can sucessfully extract the κ from the fitting even with non-zero γ_ϕ.

6.5. CONCLUSION

To summarize, we have demonstrated a single-photon resonator spectroscopy using a weakly coupled qubit. From the appearance of an electromagnetically induced transparency in the qubit population spectrum, we obtained a single-photon linewidth of a high-Q resonator. We validated our result using an independent measurement of the resonator linewidth through a separate transmission line. Our spectroscopy method here is compatible with a resonator of an even smaller loss rate than that in the present work, without demanding a high coherence qubit, due to its being weakly invasive. This work offers a method for reliable estimates of the loss rates of superconducting resonators and enables the study of EIT in a weak dispersive regime of circuit QED.

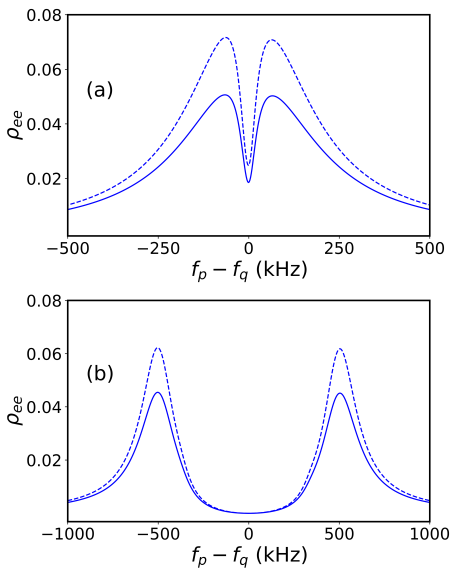

Figure 6.7: Comparison between the qubit population spectrum with and without considering the pure dephasing rate of the qubit. (a) Simulated qubit population spectrum in EIT regime when the parameters $\Omega_{sb}, \Omega_p, \gamma, \gamma_\phi, \kappa, \chi_{qt}$ are $2\pi\times$(100,100,400,0,30,10) kHz (solid line) and $2\pi\times$(100,100,300,50,30,10) kHz (dashed line). (b) Simulated qubit population spectrum in ATS regime when the parameters $\Omega_{sb}, \Omega_p, \gamma, \gamma_\phi, \kappa, \chi_{qt}$ are $2\pi\times$(1000,100,400,0,30,10) kHz (solid line) and $2\pi\times$(1000,100,300,50,30,10) kHz (dashed line).

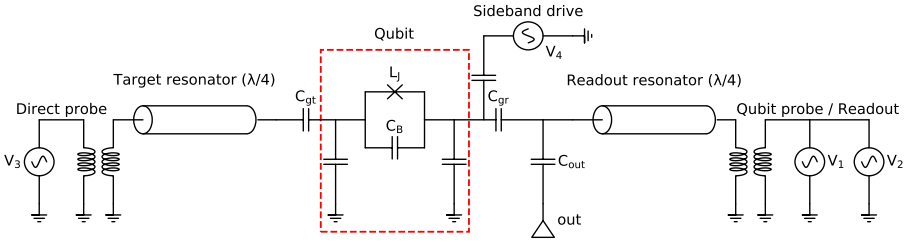

Figure 6.8: A diagram of the device and related electronics used in the experiment.

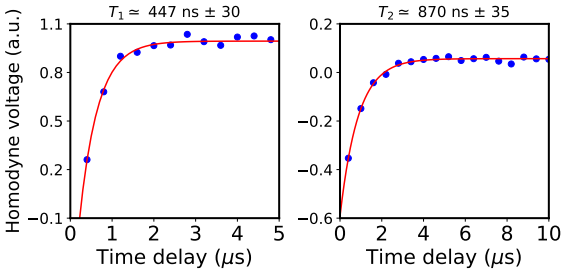

Figure 6.9: T_1 and T_2 measurement of the qubit used in the experiment.

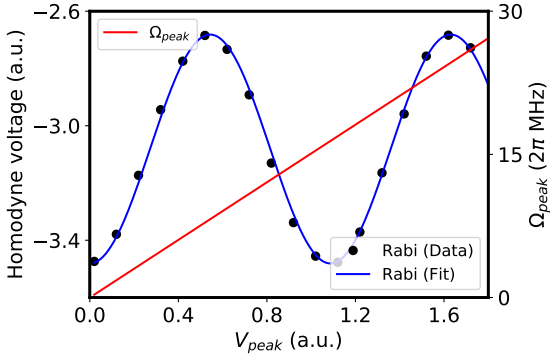

Figure 6.10: Qubit probe amplitude calibration. A Gaussian Rabi pulse was applied through the readout resonator at the qubit resonant frequency. The peak voltage of the pulse measured at room temperature is converted to the probe amplitude (red line) in units of angular frequency based on the phase of the oscillation in the homodyne readout signal (black dot and blue line).

6.6. APPENDIX-EFFECT OF PURE DEPHASING RATE IN QUBIT POPULATION SPECTRUM

In Fig. 6.7, we present additional simulation results of the qubit population spectrum. For both dashed and solid lines, the qubit have the same total linewidth but different pure dephasing rate, γ_ϕ. For dashed line,γ_ϕ is $2\pi \times 50$kHz whereas for solid line, γ_ϕ is zero. One can find that even the total linewidth is the same, we can extract γ_ϕ from the qubit population spectrum. This is particularly important when using flux-tuneable qubits that normally has significant γ_ϕ comparable to γ when the flux is tuned out of the sweep spot.

6.7. APPENDIX-CIRCUIT DETAIL

In Fig. 6.8, we depict the device and related electronics in the experiment. A qubit (red dashed box) is coupled to two co-planar waveguide (CPW) resonators. Each resonator is inductively coupled to a separate feedlines. In all, four microwave sources ($V_{1\sim4}$) are used in the experiment: one each for the qubit driving, qubit readout, direct resonator probing, and sideband driving. The device is anchored to the mixing chamber plate of a LD250 Bluefors dilution refrigerator with a base temperature under 7 mK.

6.8. APPENDIX-DEVICE TIME DOMAIN CHARACTERISTIC

In Fig. 6.9, we present a time domain characterization of the qubit used in the experiment. T_1 and T_2 are 447 ± 30 ns and 870 ± 35 ns respectively. Since $2T_1 \simeq T_2$ holds approximately, it justifies our decision in Section 6.2.1 to neglect the pure dephasing in the master equation model.

6.9. APPENDIX-PROBE AMPLITUDE CALIBRATION

We applied a 60-ns long Gaussian pulse with a width of σ=15 ns at the qubit resonant frequency through the source V1, which was followed by a 200-ns long readout pulse from the same source. The Rabi oscillation swept the peak voltage of the pulse envelop V_{peak} as depicted in Fig. 6.10. The phase θ of this oscillation is given by $\theta = \Omega_{peak}\int_{-2\sigma}^{2\sigma} \exp[-t^2/(2\sigma^2)]dt$. For $\theta = \pi$, $\Omega_{peak} = 2\pi \times 13.94$ MHz and $V_{peak} = 0.54$ arb. unit. This yields a conversion factor Ω_{peak}/V_{peak} =25.81 MHz/arb. unit. If the probe field frequency is near the qubit transition frequency, then the probe amplitude Ω_p is readily calibrated from V_p using this conversion factor.

6.10. APPENDIX-QUBIT RESONANCE SHIFT

The sideband drive induces not only a sideband transition but also shifts the qubit transition frequency. A significant frequency shift (12 MHz downward) is observed when $\Omega_{sb} \approx 2\pi \times 100$ kHz. The data are given in Fig. 6.11.

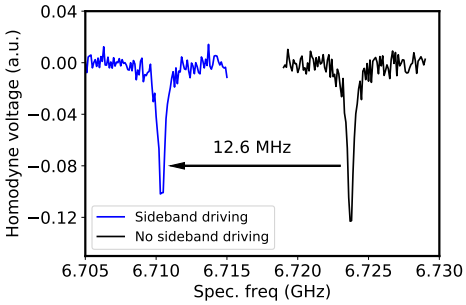

Figure 6.11: Qubit frequency shift under the sideband driving. The amount of the shift is 12.6 MHz when $\Omega_{sb} \approx 2\pi \times 100$ kHz.

7

CONCLUSION AND OUTLOOK

7.1. CONCLUSION

We have discussed circuit quantum electrodynamics (QED) systems focusing on implementing the tuneable interaction between qubits and resonators. It is of great importance for quantum state engineering as well as quantum gate operation. Although there are several possible approaches using flux controls, the flux tuneability in the qubit's frequency introduces a formidable drawback, the pure dephasing of the qubit induced by the flux noise. Instead, here we are using the external transverse driving fields. This approach is implementable even with fixed frequency qubits, and therefore the qubit's coherence time is limited solely by the decay rate. I have given quantitative studies on the sideband transition rates induced by the transverse drive fields. I also cover the regime beyond the regime of the rotating wave approximation (RWA). In total, we have discussed two popular systems, one is the quantum Rabi model and the other is a dispersively coupled transmon-resonator, both of which frequently appear in circuit QED research. In addition to the discussions on quantifying the sideband transition rates, I have also discussed a possible application of the sideband transition in the precise resonator spectroscopy. The representative added values made out of this thesis are summarized as follows.

First, the rotating wave approximation significantly underestimates the sideband transition rates as well as the qubit frequency shifts. The latter one is already well known, but the former one has been hardly investigated. This thesis proves the effect of the RWA in the sideband transition rates in analytical, numerical, and experimental ways.

Second, the breakdown of the rotating wave approximation is not explicitly shown in the conventional experiments, where we simply measure the transition rates and qubit frequency shifts without any independent calibration for the driving power. We typically calibrate the driving power from the qubit frequency shifts, and estimate the transition rates based on this calibration. Since the RWA distorts both simultaneously, one cannot identify the effect whether the RWA breakdowns or not. For precise estimation of the required drive power, this fact can critically mislead the experimentalist. This finding should concern the quantum technology community.

Third, electromagnetically induced transparency (EIT) can be used for non-invasive spectroscopy techniques when probing high-quality factor resonators. The conventional approach to measuring the internal quality factor of the superconducting resonators is coupling them to the external feed line and investigating the transmission or reflection signals. To keep the internal quality factor high, the external coupling strength should be much smaller than the internal loss rate of the resonator, which results in very poor contrast in the resonator spectroscopy signal. This challenge can be circumvented by using a sensor qubit weakly coupled to the resonator. By creating EIT in the qubit's population spectrum, one can measure the resonator's quality factor without the external feedline. The sensor qubit also mediates the coupling between the resonator and environment as the external feedline does. However, the obtainable contrast is much better than that of the conventional approach.

Forth, an accurate numerical simulation methodology is presented in this thesis in chapter 4 and 5. It explains why the micro-oscillation in the quantum dynamics does not exist in the real experiments. Repeating the simulations with different pulse lengths and Gaussian rising and falling, it has been proven that precisely benchmarking real ex-

periment is feasible. Clear sinusoidal oscillations are obtained in the simulation, which are in fact consistent with those observed in the experiments.

7.2. OUTLOOK

7.2.1. PROPERTIES OF TRANSMON UNDER TIME-PERIODICAL DRIVE

This thesis has mainly discussed the implementation and quantification of the qubit and resonator tuneable interface through external transverse drives. In chapters 4,5, and 6, we also have learned that the external drive fields also can induce the qubit's frequency shifts. Then, we can naturally raise a question: Is there any other significant changes in qubit's characteristic other than frequency shifts? The answer to this question is yes. At the final stage of my PhD, I have realized that the external drive fields also can significantly change two essential properties of the transmon. One is transmon's anharmonicity, and the other one is dispersive coupling strength to the resonator. I have also studied these phenomena analytically, numerically, and experimentally. However, I could not include the results of these studies in this thesis due to the time restriction. The results will be presented in papers 8 and 9 in my publication list.

7.2.2. DIRECTION OF FURTHER STUDY

The main advantage of using the external drive for the tunable interfaces among the circuit elements is that it can be implementable without flux tunability. Fixed frequency qubits have several subtaintial advantages over flux tunable qubits. First of all, the fixed frequency qubit is insensitive to the flux noise, known as the most significant source of the qubit's pure dephasing. Removing the flux lines also decreases the complexity in the fabrication and control of the device. Nonetheless, there are several downsides together in using fixed frequency qubits. Hence, the direction of the further study should go in a way to maximize the advantages and minimize the disadvantages.

Frequency crowding problem [112, 113] is one of the possible issues often remarked as a downside of using fixed frequency qubits. It takes place when multiple qubits having similar frequencies are coupled to a single resonator or a qubit is coupled to multiple neighboring qubits with similar frequencies. When performing single qubit gates on a specific qubit in this situation, the gate operations can couple the qubit to neighbor qubits' transitions (leakage) or induce other unwanted transitions on the third qubit. To suppress this problem, we can distribute the qubits to multiple resonators that are totally decoupled to one another. Also, if all the individual qubits have different drivelines, we can make sigle qubit gate operations to each qubit independent. Another potential issue is fridge heating. Tunable coupling based on the external drive fields relies on the nonlinear process and requires high drive power. The required total drive power to the fridge linearly increases the number of qubits on the device. Although I have already provided a method I used to avoid this issue in chapter 3, this approach should break down at some point with the large qubit number. All these problems are not fundamental but technical. In the future study, they need to be solved for large scale qubit device without flux control.

A

APPENDIX-A

A

A.1. FABRICATION RECIPE FOR SUPERCONDUCTING QUBIT DEVICES

A.1.1. BASE LAYER

The below recipe is applicable when using a 100 nm NbTiN film on a Silicon substrate. If the thickness is different, then the thickness of the EBL resist and the etching time should be also different.

- Spin coat EBL resist. ARN 7780-13 at 4000 rpm and bake at 95°C for 90 seconds [1].
- EBL with a dose of 130 $\mu C/cm^2$.
- Develop ARN layer using MF321 for 2 mins and 30 seconds.
- Reactive ion etching. Use SF_6 and O_2 as etching gas. The flow rates are 145 sccm for SF_6, and 120 sccm for O_2. Applied AC power is 50 Watt. Typical etching time is around 2 min 30 seconds.
- Eliminate remaining EBL resist using PRS or NMP.

A.1.2. JOSEPHSON JUNCTION

- Spin coat EBL resists. PMGI SF7 at 1500 rpm and bake at 185°C for 5 minutes[2]. PMMA A3 950k at 2500 rpm and bake at 185°C for 10 minutes[3].
- EBL with a dose of 1850 $\mu C/cm^2$.
- Develop PMMA and PMGI layer. For PMMA, develop by using MIBK and IPA 1:3 mixture for 60 seconds. Then move the chip to MIBK and Ethanol 1:3 mixture for 60 seconds. Finally, put the chip in the IPA solution for 10 seconds. For PMGI, use MF321 for 15 seconds, and immediately move the chip to the water for 30 seconds.
- Oxygen plasma cleaning to eliminate the residual resist. O_2 gas with a flow rate of 10 sccm. Applied AC power is 30 Watt for 60 seconds.
- Buffered oxide etch (BOE) for 30 seconds. Use 1:7 BOE solution.
- Deposit the first Aluminium layer. Thickness of 60nm.
- Oxidation layer. Chamber pressure is 1.3 mbar when oxygen is injected. Duration is 11 mins.
- Deposit the 2nd Aluminium layer. Thickness of 100 nm.
- Lift-off the Aluminum layer using NMP.

[1] This forms a layer of 540 nm thickness.
[2] This forms a layer of 570 nm thickness.
[3] This forms a layer of 150 nm thickness.

A.2. FABRICATION RECIPE FOR SiC COATING INSIDE THE RADIATION SHIELD

First, we prepare pre-coating with Stycast 2850FT (100g) and Catalyst 9 (4g). SiC coating mixture is composed of Stycast 2080FT (100g), Catalyst24LV (8g), and SiC powders. We use several sizes of SiC, 70 grit (40g), 60 grit (45g), 24 grit (40g), 36 grit (40g), and CMF-CVD (40g). Once the mixture is completed, the remaining steps are the followings. Stir the mixtures until they get well mixed. Put red non-elastic tape over screw holes in Copper shield. Coat inner side of Copper can with pre-coating mixture. Coat inner side of Copper can with SiC coating mixture. Coat cold finger with pre-coating and SiC coating mixture. Remove the residual coating material inside of wire holes by cotton bud. Clean up the stuff. Dry for a day at room temperature.

B

APPENDIX-B

Descriptions of some of the programming codes I developed during my PhD is presented here.

All the simulation codes discussed in this chapter is available in github.com/bann-01.

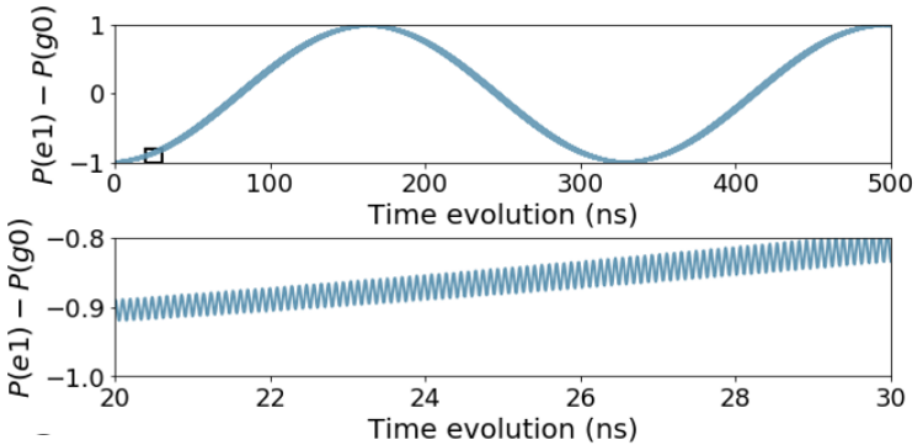

Figure B.1: Time-domain plots of the numerical simulation results. Blue sideband transition between a transmon and resonator is simulated. The bottom panel is the magnified view of the area enclosed by the box in the top panel. One can identify the slow and large oscillation (top) and the fast and small oscillation (bottom) exist at the same time.

B.1. QUANTUM DYNAMIC SIMULATION WITHOUT THE ROTATING WAVE APPROXIMATION.

In Chapter 4 and 5, I briefly introduce the numerical calculation method to obtain the sideband transition rates. In fact, there is a technical challenge to solve the master equation of the time periodically driven quantum systems. As you can see in figure B.1, the dynamics is decomposed into two parts. One is the slow oscillating component with a large amplitude, and the other is the fast oscillating component with a small amplitude. In order to get the sideband transition rates, the total time range of the simulation should be sufficiently long to cover at least one cycle of the slow oscillation, and the unit time should be small enough to resolve the fast oscillation. Therefore, the total number of the time steps in the simulation should be very large, consuming lots of random access memory (RAM). This could not be a significant problem when simulating very low dimensional system like spin-1/2. However, if you want to simulate the system that should be described high dimensional hilbert space, like driven harmonic oscillator for instance, than your simulation is largely limited by the size of the (RAM).

Together with Wouter Kessels, we have invoked an idea to tackle this challenge. First, we segment the time range of the simulation as depicted in figure B.2. Then, we perform the simulation in the first segment, denoted by number 1. Once the simulation is done, then we save all the results in the hard disk drive and empty the memory except the last data point of the first segment. This data is used as the initial condition for the simulation in segment 2. We repeat this procedure until we complete the simulation in the final segment. No matter how long the total time range is, we can complete the simulation without using up the computer memory.

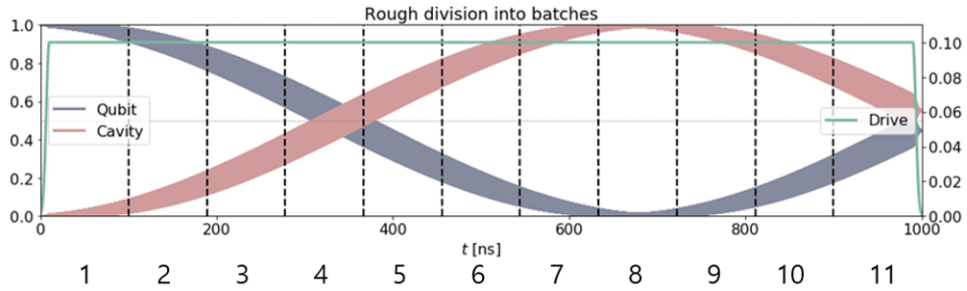

Figure B.2: Description of 'Segment and combine' simulation approach.

B.2. SYSTEM'S NOISE SPECTRUM SIMULATION BASED ON THE TIME-CORRELATION.

It is often useful to estimate the qubit's shifted transition frequency under the driving fields. Although the analytical formula is given in Chapter 4 and 5 for two-level system and transmon cases respectively, the accuracy of the formula is not guaranteed for strong drivings since they are derived based on the perturbative approach. The transition frequency can be also obtained from the qubit's noise spectrum. For transmon case, the noise spectrum $S_{xx}(\omega)$ defined by,

$$S_{xx}(\omega) = \int_{-\infty}^{\infty} d\tau e^{i\omega t} \langle \hat{x}(t+\tau)\hat{x}(t) \rangle \tag{B.1}$$

Here, $\hat{x}$ is defined by $\frac{2E_c}{E_j}^4(\hat{a}+\hat{a}^\dagger)$. Also, $\hat{a}$ and $\hat{a}^\dagger$ are lowering and rising operators of the tramsmon. The bracket in Eq. B.1 means the time average over t. For stationary system, $\langle \hat{x}(t+\tau)\hat{x}(t) \rangle$ is a function of only τ. For non-stationary systems like time-periodically driven transmon we mainly discuss in this thesis, we cannot drop the t dependence of $\langle \hat{x}(t+\tau)\hat{x}(t) \rangle$. For time-periodically driven systems, $\langle \hat{x}(t+\tau)\hat{x}(t) \rangle$ has a time periodicity $T = 2\pi\omega_d^{-1}$. Fortunately, I have found that just fixing t by an arbitrary value between 0 and ω_d^{-1} solves the problem. The calculated spectrum is independent with t with minor differences. Another point at which we should be mindful in calculating $S_{xx}(\omega)$ of time-dependent systems is that we should set the initial state by quasi-stationary states. For the transmon under the driving field, the ground state cannot be a quasi-stationary state. If one uses the ground state as an initial state in the calculation, then significant distortion in the spectrum is shown. In my case, I first acquire the quasi-stationary state from a separate master equation simulation, and use the obtained state in the time-correlation calculation. Successfully calculated driven transmon's noise spectrum is given in figure B.3.

B

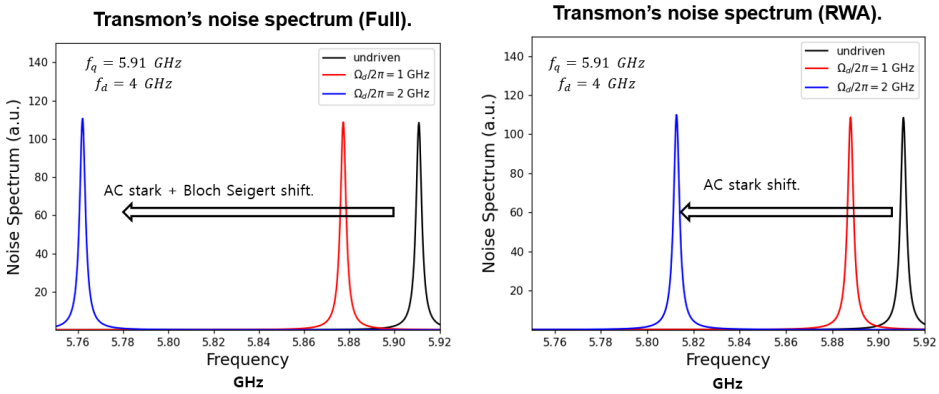

Figure B.3: Simulated noise spectrum of a time-periodically driven transmon qubit. (Left) Simulation with driving Hamiltonian without the rotating wave approximation. (Right) Simulation with driving Hamiltonian with the rotating wave approximation.

SUMMARY

In this work, I investigate how to implement and quantify *in-situ* tunable quantum interface between superconducting qubits and resonators using external transverse driving fields beyond the rotating wave approximation (RWA). When studying the system under the time-periodic driving field, we typically rely on RWA, a useful technique that significantly reduces the analytical difficulties in solving the dynamics with time-dependent Hamiltonian. Nonetheless, it does not correctly describe the systems' dynamics when the drive fields are excessively strong and far off-resonant. Especially in circuit QED platform, the RWA often breakdowns. Many studies before, however, mainly focus on the transition frequency shifts. How the RWA distorts the interaction rates between two systems has been rarely explored.

I have performed quantitative studies over two different systems. One is the quantum Rabi model (QRM) where a two-level atom is dispersively coupled to a resonator mode. The other is dispersively coupled a transmon and resonator system, which is the same as the QRM except that the transmon replaces the two-level atom in QRM. In both cases, I have revealed that the RWA significantly mislead the sideband transition rates between two elements. In the latter case, I have performed the experiments, and the results nicely agree with the analytical and numerical calculations. In addition to these, I also have introduced a study where the tunable coupling between a transmon and resonator is used for non-invasive resonator probing.

SAMENVATTING

In dit onderzoek wordt het middenveld tussen supergeleidende qubits en resonatoren gekwantificeerd met behulp van externe transversale aandrijfvelden waarbij de rotating wave benadering (RWA) niet meer van toepassing is. Bij het bestuderen van het systeem onder periodieke aandrijving, is de RWA een gebruikelijke methode om het systeem Hamiltonian tijdsonafhankelijk te maken. Hier wordt het verkrijgen van een analytische oplossing minder ingewikkeld en moeizaam. Helaas kan dit techniek niet worden toepast wanneer de aandrijfvelden extreem sterk of ver aflegt van het resonantie van het systeem. Veel literatuur richt zich voornamelijk op het verband tussen RWA en verschuivingen in transititie frequenties. De manier waarop de RWA de interactiesnelheid tussen 2 gekoppelde systemen verstoort is grotendeels nog niet onderzocht.

Ik heb kwantitatieve studies uitgevoerd van twee verschillende systemen: het ene is het kwantum Rabi-model (QRM) waarbij een atoom met twee energie niveaus dispersief is gekoppeld aan een resonator. Het andere is een transmon dat dispersief gekoppeld is aan een resonatorsysteem, wat hetzelfde is als de QRM behalve dat de transmon het atoom met twee niveaus vervangt. In beide gevallen heb ik aangetoond dat de koppeling tussen kruiselings energieniveas, verkregen uit de RWA, onjuist is. Ook heb ik de experimenten uitgevoerd waarbij resultaten overeen komen met de analytische en numerieke berekeningen. Daarnaast heb ik ook een onderzoek uitgevoerd waarbij het aanpasbare koppeling tussen een transmon en resonator kan worden gebruikt voor non-invasive resonatormetingen.

BIBLIOGRAPHY

[1] P. Grangier *et al.*, "Experimental evidence for a photon anticorrelation effect on a beam splitter: a new light on single-photon interferences", Euro. Phys. Lett. **1**, 173 (1986).

[2] A. Aspect *et al.*, "Experimental tests of realistic local theories via bell's theorem", Phys. Rev. Lett. **47**, 460 (1981).

[3] I. Marinković *et al.*, "Optomechanical bell test", Phys. Rev. Lett. **121**, 220404 (2018).

[4] B. Hensen *et al.*, "Loophole-free bell inequality violation using electron spins separated by 1.3 kilometres", Nature **526**, 682 (2015).

[5] Y. P. ZhongView *et al.*, "Violating bell's inequality with remotely connected superconducting qubits", Nat. Phys. **15**, 741 (2019).

[6] F. Arute *et al.*, "Quantum supremacy using a programmable superconducting processor", Nature **574**, 505 (2019).

[7] N. Gisin and Rob Thew, "Quantum communication", Nat. Photo. **1**, 165 (2007).

[8] J. I. Cirac and P. Zoller, "Goals and opportunities in quantum simulation", Nat. Phys. **8**, 264 (2012).

[9] M. Greiner and S. Fölling, "Optical lattices", Nature **736**, 453 (2008).

[10] J. Ye *et al.*, "Trapping of single atoms in cavity qed", Phys. Rev. Lett. **83**, 4987 (1999).

[11] M. H. Anderson *et al.*, "Observation of bose-einstein condensation in a dilute atomic vapor", Science **198**, 5221 (1995).

[12] M. Greiner *et al.*, "Quantum phase transition from a superfluid to a mott insulator in a gas of ultracold atoms", Nature **39**, 415 (2002).

[13] N. GrzesiakView *et al.*, "Efficient arbitrary simultaneously entangling gates on a trapped-ion quantum computer", Nat. Comm. **11**, 2963 (2020).

[14] R. Boyd, *Nonlinear optics* (Academic Press, New York, 2008).

[15] D. Bouwmeester *et al.*, "Experimental quantum teleportation", Nature **390**, 575 (1997).

[16] A. Ekert *et al.*, "Quantum cryptography based on bell's theorem", Phys. Rev. Lett. **61**, 661 (1991).

[17] D. Loss and D. P. DiVincenzo, "Quantum computation with quantum dots", Phys. Rev. A **57**, 120 (1998).

[18] A. Wallraf *et al.*, "Strong coupling of a single photon to a superconducting qubit using circuit quantum electrodynamics", Nature **431**, 162 (2004).

[19] A. Blais *et al.*, "Quantum information processing with circuit quantum electrodynamics", Phys. Rev. A **75**, 032329 (2007).

[20] J. Koch *et al.*, "Charge-insensitive qubit design derived from the cooper pair box", Phys. Rev. A **76**, 042319 (2007).

[21] F. Motzoi *et al.*, "Simple pulses for elimination of leakage in weakly nonlinear qubits", Phys. Rev. Lett. **103**, 110501 (2010).

[22] M. H. Michael *et al.*, "New class of quantum error-correcting codes for a bosonic mode", Phys. Rev. X **6**, 031006 (2016).

[23] S. Rosenblum *et al.*, "Fault-tolerant detection of a quantum error", Science **6399**, 266 (2018).

[24] R. Lescanne *et al.*, "Exponential suppression of bit-flips in a qubit encoded in an oscillator", Nat. Phys. **16**, 509 (2020).

[25] M. Hofheinz *et al.*, "Generation of fock states in a superconducting quantum circuit", Nature **454**, 310 (2008).

[26] Z. Leghtas *et al.*, "Confining the state of light to a quantum manifold by engineered two-photon loss", Science **347**, 853 (2015).

[27] A. Ketterer, *Modular variables in quantum information* (Universit´e Paris Diderot, Paris, 2016).

[28] P. Giscard *et al.*, "Dynamics of quantum systems driven by time-varying hamiltonians: solution for the bloch-siegert hamiltonian and applications to nmr", Phys. Rev. Res. **2**, 023081 (2020).

[29] J. R. Johansson *et al.*, "Qutip 2: a python framework for the dynamics of open quantum systems", Comp. Phys. Comm. **184**, 1234 (2013).

[30] J. R. Johansson *et al.*, "Qutip: an open-source python framework for the dynamics of open quantum systems", Comp. Phys. Comm. **183**, 1760 (2012).

[31] F. Bloch and A. Siegert, "Magnetic resonance for nonrotating fields", Phys. Rev. **57**, 522 (1940).

[32] D. M. Pozar, *Microwave engineering* (Wiley, Danvers, 2012).

[33] P. Krantz *et al.*, "A quantum engineer's guide to superconducting qubits featured", Appl. Phys. Rev. **6**, 021318 (2019).

[34] D. Ristè *et al.*, "Feedback control of a solid-state qubit using high-fidelity projective measurement", Phys. Rev. Lett. **109**, 240502 (2012).

[35] L. DiCarlo *et al.*, "Demonstration of two-qubit algorithms with a superconducting quantum processor", Nature **460**, 240 (2009).

[36] F. Beaudoin *et al.*, "First-order sidebands in circuit qed using qubit frequency modulation", Phys. Rev. A **86**, 022305 (2012).

[37] J. D. Strand *et al.*, "First-order sideband transitions with flux-driven asymmetric transmon qubits", Phys. Rev. B **87**, 220505(R) (2013).

[38] E. R. Z. Ramdin, *Determining the most reliable and reproducible measurement method for measuring al-alox-al josephson junctions at room temperature* (Delft University of Technology, Delft, 2019).

[39] D. J. Thoen *et al.*, "Superconducting nbtin thin films with highly uniform properties over a ø 100 mm wafer", IEEE Transactions on Applied Superconductivity **27** (2017).

[40] A. Bruno *et al.*, "Reducing intrinsic loss in superconducting resonators by surface treatment and deep etching of silicon substrates", Appl. Phys. Rev. **106**, 182601 (2015).

[41] X. Xue *et al.*, "Cmos-based cryogenic control of silicon quantum circuits", Nature **593**, 205 (2021).

[42] R. Nikandish, "Cmos quantum computing: toward a quantum computer system-on-chip", arXiv:2012.09021 (2020).

[43] G. J. Dolan, "Offset masks for lift-off photoprocessing", Appl. Phys. Rev. **337**, 31 (1977).

[44] V. Ambegaokar and A. Baratoff, "Tunneling between superconductors", Phys. Rev. Lett. **10**, 486 (1963).

[45] L. Duan *et al.*, "The mixed quantum rabi model", Sci. Rep. **9**, 18353 (2019).

[46] L. Cong *et al.*, "Selective interactions in the quantum rabi model", Phys. Rev. A **101**, 032350 (2020).

[47] B.Ann *et al.*, "Tunable and weakly invasive probing of a superconducting resonator based on electromagnetically induced transparency", Phys. Rev. A **102**, 053721 (2020).

[48] P. Alsing *et al.*, "Jaynes-cummings model under monochromatic driving", Phys. Rev. A **45**, 5135 (1992).

[49] F. Deppe *et al.*, "Two-photon probe of the jaynes–cummings model and controlled symmetry breaking in circuit qed", Nat. Phys. **4**, 686 (2008).

[50] L. Ermann *et al.*, "Jaynes-cummings model under monochromatic driving", Phys. Rev. A **102**, 033729 (2020).

[51] L. Henriet *et al.*, "Quantum dynamics of the driven and dissipative rabi model", Phys. Rev. A **90**, 023820 (2014).

[52] Z. Chen *et al.*, "Single-photon-driven high-order sideband transitions in an ultrastrongly coupled circuit-quantum-electrodynamics system", Phys. Rev. A **96**, 012325 (2017).

[53] J. R. Schrieffer and P. A. Wolff, "Relation between the anderson and kondo hamiltonians", Phys. Rev. **149**, 491 (1966).

[54] D. A. Andrews *et al.*, "Observation of bloch-siegert shifts in the $2^2s1/2$-$2^2p1/2$ microwave resonance in atomic hydrogen", J. Phys. B **57**, 522 (1940).

[55] G. D. Fuchs *et al.*, "Gigahertz dynamics of a strongly driven single quantum spin", Science **326**, 5959 (2009).

[56] J. Tuorila *et al.*, "Stark effect and generalized bloch-siegert shift in a strongly driven two-level system", Phys. Rev. Lett. **105**, 257003 (2010).

[57] C. Deng *et al.*, "Observation of floquet states in a strongly driven artificial atom", Phys. Rev. Lett. **115**, 133601 (2015).

[58] A. Laucht *et al.*, "Breaking the rotating wave approximation for a strongly driven dressed single-electron spin", Phys. Rev. B **94**, 161302(R) (2016).

[59] I. Pietikäinen *et al.*, "Observation of the bloch–siegert shift in a driven quantum-to-classical transition", Phys. Rev. B **96**, 020501(R) (2016).

[60] E. J. Sie *et al.*, "Large, valley-exclusive bloch-siegert shift in monolayer ws2", Science **355**, 6329 (2017).

[61] J. V. Koski *et al.*, "Floquet spectroscopy of a strongly driven quantum dot charge qubit with a microwave resonator", Phys. Rev. Lett. **121**, 043603 (2018).

[62] P. J. Leek *et al.*, "Using sideband transitions for two-qubit operations in superconducting circuits", Phys. Rev. B **79**, 180511(R) (2009).

[63] P. J. Leek *et al.*, "Cavity quantum electrodynamics with separate photon storage and qubit readout", Phys. Rev. Lett. **79**, 100504 (2009).

[64] S. O. Mundhada *et al.*, "Experimental implementation of a raman-assisted six-quanta process", Phys. Rev. Appl. **12**, 054051 (2019).

[65] J. D. Teufel *et al.*, "Sideband cooling of micromechanical motion to the quantum ground state", Nature **475**, 359 (2011).

[66] A. Schliesser *et al.*, "Resolved-sideband cooling of a micromechanical oscillator", Nat. Phys. **4**, 415 (2008).

[67] C. Monroe *et al.*, "Resolved-sideband raman cooling of a bound atom to the 3d zero-point energy", Phys. Rev. Lett. **75**, 4011 (1995).

[68] M. Hennrichh *et al.*, "Vacuum-stimulated raman scattering based on adiabatic passage in a high-finesse optical cavity", Phys. Rev. Lett. **85**, 4872 (2000).

[69] M. J. Reagor, *Superconducting cavities for circuit quantum electrodynamics* (Yale University thesis, New Haven, 2015).

[70] M. Gely *et al.*, "Nature of the lamb shift in weakly anharmonic atoms", Phys. Rev. A **98**, 053808 (2018).

[71] R. Lescanne *et al.*, "Escape of a driven quantum josephson circuit into unconfined states", Phys. Rev. Appl. **11**, 014030 (2019).

[72] K. M. Birnbaum *et al.*, "Photon blockade in an optical cavity with one trapped atom", Nature **436**, 87 (2005).

[73] Y. Zhou *et al.*, "Tunable microwave single-photon source based on transmon qubit with high efficiency", Phys. Rev. Appl. **13**, 034007 (2020).

[74] B. Yurke, "Squeezed-state generation using a josephson parametric amplifier", J. Opt. Soc. Am. B **4**, 1551 (1987).

[75] S. Bose *et al.*, "Preparation of nonclassical states in cavites with a moving mirrow", Phys. Rev. A **56**, 4175 (1997).

[76] M. Lugwig *et al.*, "Enhanced quantum nonlinearities in a two-mode optomechanical system", Phys. Rev. Lett. **109**, 063601 (2012).

[77] S. Gupta *et al.*, "Cavity nonlinear optics at low photon number from collective atomic motion", Phys. Rev. Lett. **99**, 231601 (2007).

[78] G. Eckhardt *et al.*, "Stimulated raman scattering from organic liquids", Phys. Rev. Lett. **9**, 455 (1962).

[79] T. Hänsch *et al.*, "Doppler-free two-photon spectroscopy of hydrogen 1s-2s", Phys. Rev. Lett. **34**, 307 (1975).

[80] P. T. Eles *et al.*, "Stimulated raman scattering from organic liquids", J. Chem. Phys. **121**, 10167 (2004).

[81] A. Wallraf *et al.*, "Sideband transitions and two-tone spectroscopy of a superconducting qubit strongly coupled to an on-chip cavity", Phys. Rev. Lett. **99**, 050501 (2007).

[82] K. S. Kumar *et al.*, "Stimulated raman adiabatic passage in a three-level superconducting circuit", Nat. Comm. **100**, 033802 (2020).

[83] S. Premaratne *et al.*, "Microwave photon fock state generation by stimulated raman adiabatic passage", Nat. Comm. **8**, 14148 (2017).

[84] A. Vepsäläinen *et al.*, "Superadiabatic population transfer in a three-level superconducting circuit", Sci. Adv. **5**, 5999 (2019).

[85] Y. -M. He *et al.*, "Coherently driving a single quantum two-level system with dichromatic laser pulses", Nat. Phys. **15**, 941 (2019).

[86] T. T. Meiling *et al.*, "Two-photon excitation fluorescence spectroscopy of quantum dots: photophysical properties and application in bioassays", J. Phys. Chem. C **112**, 9641 (2019).

[87] S. Gasparinetti *et al.*, "Correlations and entanglement of microwave photons emitted in a cascade decay", Phys. Rev. Lett. **119**, 140504 (2017).

[88] S. Gasparinetti *et al.*, "Two-photon resonance fluorescence of a ladder-type atomic system", Phys. Rev. A **100**, 033802 (2020).

[89] A. Quattropani *et al.*, "Two-photon transitions to excited states in atomic hydrogen", Phys. Rev. A **6**, 3079 (1982).

[90] A. P. Saiko *et al.*, "Effective field and the bloch-siegert shift at bichromatic excitation of multiphoton epr", JETP Letter **84**, 130 (2006).

[91] W. J. Meath, "Bloch-siegert effects in two-photon excitations: fixed laser-molecule configurations versus orientational averaging", J. Chem. Phys. **149**, 204114 (2018).

[92] B. Ann, "Sideband transitions in a two-mode josephson circuit driven beyond the rotating wave approximation.", 10.5281/zenodo.4568937 (2020).

[93] A. Miroshnichenko *et al.*, "Exponential suppression of bit-flips in a qubit encoded in an oscillator", Optics and Photonics News **19**, 12 (2008).

[94] M. S. Khalil *et al.*, "An analysis method for asymmetric resonator transmission applied to superconducting devices", J. Appl. Phys. **111**, 054510 (2012).

[95] M. Reagor *et al.*, "Reaching 10ms single photon lifetimes for superconducting aluminum cavities", J. Appl. Phys. **102**, 192604 (2013).

[96] K. M. Birnbaum *et al.*, "Photon blockade in an optical cavity with one trapped atom", Nature **436**, 87 (2005).

[97] T. Peyronel *et al.*, "Quantum nonlinear optics with single photons enabled by strongly racting atoms", Nature **488**, 57 (2012).

[98] W. Chen *et al.*, "All-optical switch and transistor gated by one stored photon", Science **6147**, 768 (2013).

[99] J. Long *et al.*, "Electromagnetically induced transparency in circuit quantum electrodynamics with nested polariton states", Phys. Rev. Lett. **120**, 083602 (2018).

[100] G. Andersson *et al.*, "Electromagnetically induced acoustic transparency with a superconducting circuit", J. Appl. Phys. **124**, 240402 (2020).

[101] S. Novikov *et al.*, "Raman coherence in a circuit quantum electrodynamics lambda system", Nat. Phys. **12**, 75 (2016).

[102] Q. -C. Li *et al.*, "Method for identifying electromagnetically induced transparency in a tunable circuit quantum electrodynamics", Phys. Rev. A **12**, 75 (2016).

[103] D. I. Schuster *et al.*, "Resolving photon number states in a superconducting circuit", Nature **445**, 515 (2007).

[104] S. Novikov *et al.*, "Autler-townes splitting in a three-dimensional transmon superconducting qubit", Phys. Rev. B **88**, 060503(R) (2013).

[105] M. A. Sillanpää *et al.*, "Autler-townes effect in a superconducting three-level system", Nature **103**, 193601 (2009).

[106] W. R. Kelly *et al.*, "Direct observation of coherent population trapping in a superconducting artificial atom", Phys. Rev. Lett. **104**, 163601 (2010).

[107] J. L. *et al.*, "Dynamical autler-townes control of a phase qubit", Sci. Rep. **2**, 645 (2012).

[108] P. M. Anisimov *et al.*, "Objectively discerning autler-townes splitting from electromagnetically induced transparency", Phys. Rev. Lett. **107**, 163604 (2011).

[109] P. V. Klimov *et al.*, "Fluctuations of energy-relaxation times in superconducting qubits", Phys. Rev. Lett. **121**, 090502 (2018).

[110] Y. Chen *et al.*, "Qubit architecture with high coherence and fast tunable coupling", Phys. Rev. Lett. **113**, 220502 (2014).

[111] R. Versluis *et al.*, "Scalable quantum circuit and control for a superconducting surface code", Phys. Rev. Appl. **8**, 034021 (2017).

[112] R. Schutjens *et al.*, "Single-qubit gates in frequency-crowded transmon systems", Phys. Rev. A **88**, 052330 (2013).

[113] M. Chow *et al.*, "Device challenges for nearterm superconducting quantum processors: frequency collisions", IEEE International Electron Devices, 6.1.1–6.1.3 (2018).

CURRICULUM VITÆ

Byoung-moo ANN

03-03-1988 Born in Seoul, Republic of Korea (South Korea).

EDUCATION

2004–2007 Yangcheon High School

2007–2014 BSc in Physics & Physics Education
Seoul National University

2011–2013 Mandatory military service.

2016 MSc in Physics
Ludwig Maximilian University and Max Planck Institute of Quantum Optics
Thesis: Investigation of Beryllium and Magnesium mixed ion crystal toward Helium^{+} 1S-2S spectroscopy.
Promotor: Prof. Th. Udem

2017–2021 PhD in Applied physics
Delft University of Technology
Thesis: Tunable quantum interface between superconducting Qubits and microwave Photons induced by extreme driving.
Promotor : Prof. G. A. Steele
Co-Promotor: Dr. T. van der Sar

LIST OF PUBLICATIONS

9. **B. Ann** and G. A. Steele, *Modified dispersive and Lamb shifts of a Floquet multi-level artificial atom coupled to a linear resonator* (In preparation)

8. **B. Ann** and G. A. Steele, *Multi-level Bloch-Siegert effect of quantum Duffing oscillators: Validity and invalidity of the Kerr resonator model* (In preparation)

7. **B. Ann**, W. Kesseles, and G. A. Steele, *Tuneable qubit-cavity interface in a time-periodically driven quantum Rabi model : Quantitative analysis beyond the rotating wave approximation* (to be submitted)

6. **B. Ann**, W. Kesseles, and G. A. Steele, *Sideband transition in a two-mode Josephson circuit driven beyond the rotating wave approximation*, arXiv:2011.14600, Physical Review Research (In press)

5. **B. Ann** and G. A. Steele, *Weakly-invasive probing of a superconducting resonator based on electromagnetically induced transparency*, arXiv:2005.01975, Physical Review A **102**, 053721 (2020)

4. **B. Ann**, Y. Song, J. Kim, D. Yang, and K. An, *Scalable sub-Poisson field lasing in a microlaser*, arXiv:1906.11019, Scientific Reports **9**, 17110 (2019)

3. **B. Ann**, F. Schmid, J. Krause, T. Hänsch, Th. Udem, and A. Ozawa, *Motional resonances of three-dimensional dual-species Coulomb crystals*, Journal of Physics B **52**, 035002 (2019)

2. **B. Ann**, Y. Song, J. Kim, D. Yang, and K. An, *Indirect measurement of three-photon correlation in non-classical light*, arXiv:1608.07915, Physical Review A **93**, 063816 (2016)

1. **B. Ann**, Y. Song, J. Kim, D. Yang, and K. An, *Correction for the detector-dead-time effect on the second-order-correlation of stationary sub-Poissonian light in two detector configuration*, arXiv:1503.06263, Physical Review A **92**, 023830 (2015)

ACKNOWLEDGEMENTS

I would like to appreciate everyone who helped me during the 4 years journey in Delft. First of all, I would have to thank my supervisor, Prof. Gary Steele, for advising, helping, encouraging me for last 4 years. I also appreciate my PhD committee members, Prof. Vitally, Prof. Paraoanu, Prof. Terhal, Prof. Blanter, and Prof. Otte. Thanks for reading my thesis and providing me with sharp and precious comments that make my thesis more solid.

To people in Steele lab, thanks for so many memorable events and being together for the last four years with people in Steele lab. Although we were working toward different goals, we had a very sticky relationship with one another. I wish you luck at all times.

To people in QN, I regret that I used not to join many social activities among us frequently. I will miss the energetic environment here. Also, many thanks for kind administrative supports. For those who is still working for your PhD, I hope everyone will successfully finish your degrees in the future.

To people in Qutech, I am really grateful that I learned so many specialized knowledge on superconducting qubits from you. Also, thanks a lot for always giving me your hands in the cleanroom.

To people in Kavli cleanroom, the devices which make me release from PhD student to PhD could not exist without you. It was great luck that I could work in one of the best cleanrooms in the world. I am already nervous that I will not be satisfied by any other cleanroom facility and support no matter where I move to the next.

Finally, I would like to sincerely thank my family and friends in Korea who have always been cheering and supporting me.